

Department of Physics and Astronomy
University of Heidelberg

Diploma thesis
in physics

submitted by
Philipp Cörlin
born in Böblingen
September 2012

Laser induced Coulomb-explosion of allene molecules: Experiment and simulation

This diploma thesis has been carried out by Philipp Cörlin
at the
Max-Planck-Institut für Kernphysik
under the supervision of
Herrn Priv.-Doz. Dr. Robert Moshhammer

Laserinduzierte Coulomb-Explosion von Allenmolekülen: Experiment und Simulation:

Die Arbeit behandelt die durch intensive infrarote (IR) und extrem ultraviolette (XUV) Laserimpulse induzierte Coulomb-Explosion von Allenmolekülen (C_3H_4). Über den gesamten Raumwinkel werden geladene Fragmente mit einem Reaktionsmikroskop detektiert. Ein Computerprogramm zur Simulation von molekularen Fragmentationsvorgängen wurde entwickelt, um die Interpretation von Mehrfach-Ionen-Koinzidenzspektren zu erleichtern.

Die Doppelionisation von Allen durch mehrere Photonen eines intensiven IR-Impulses mit Impulslängen unter 10 fs offenbarte sechs Fragmentationskanäle mit je zwei Ionen. Vier dieser Kanäle zeigen Anzeichen einer Isomerisierung. Eine Aufspaltung in drei geladene Fragmente wurde nicht beobachtet.

Die gemessenen freigesetzten kinetischen Energien aller Coulomb-Explosions-Kanäle sind unabhängig von IR-Impulsintensität und IR-Impulslänge und ändern sich auch nicht bei der Verwendung von XUV-Impulsen. Verzweigungsverhältnisse von stabilen und instabilen zweifach geladenen Molekülionen weisen eine Abhängigkeit von der Intensität der IR-Impulse auf. Die Halbwertszeit von langlebigen metastabilen zweifach geladenen Molekülionen wurde anhand von Flugzeitspektren abgeschätzt. Pump-Probe Messungen mit XUV- und IR-Impulsen deuten auf eine Dynamik von zweifach geladenem Allen auf Zeitskalen von 50 fs hin.

Laser induced Coulomb-explosion of allene molecules: Experiment and simulation:

In this thesis Coulomb-explosions of allene molecules (C_3H_4) induced by intense infrared (IR) and extreme ultraviolet (XUV) laser pulses are studied. Over the full solid angle charged particles are detected with a reaction microscope. A software for simulation of molecular fragmentation processes has been developed to facilitate the interpretation of multi-ion coincidence spectra.

Multi-photon double-ionization of allene by intense IR pulses with pulse lengths below 10 fs reveals six double-ion fragmentation channels of which four show indications of an isomerization process. Triple-ion fragmentations have not been observed.

Measured kinetic energy releases of all Coulomb-explosion channels are independent of IR pulse intensity and of IR pulse length. They also do not differ, if XUV pulses are used. Branching ratios of stable and unstable dications feature a dependence on the intensity of IR pulses. The half-life of long-lived metastable allene dications is estimated from time-of-flight spectra.

Pump-probe measurements with XUV and IR pulses indicate dynamics of allene dications on time scales of 50 fs.

Contents

1. Introduction	1
2. Creation of ultrashort laser pulses	4
2.1. Theoretical background	4
2.1.1. Modelocking	4
2.1.2. Propagation of laser pulses	5
2.1.3. Spectral broadening of laser pulses	5
2.1.4. High harmonic generation	6
2.2. Laser system and high harmonic generation	7
2.2.1. Titanium-sapphire oscillator and amplifier	8
2.2.2. Hollow fiber and chirped mirror compressor	8
2.2.3. High harmonic generation chamber	10
3. Reaction microscope	13
3.1. Functional principle of reaction microscopes	13
3.2. Trajectories of charged particles within reaction microscopes	14
3.2.1. (Positive) ions	15
3.2.2. Electrons	15
3.3. Software for simulation of electron trajectories in reaction microscopes .	16
3.3.1. Parallel electric and magnetic fields	18
3.3.2. Non-parallel electric and magnetic fields	18
3.4. A comparison of simulated electron spectra with experimental data . .	18
3.4.1. Electron spectra at 40 A Helmholtz current	19
3.4.2. Electron spectra at 45 A Helmholtz current	20
4. Laser induced Coulomb-explosion of allene - Theory	22
4.1. Quantum mechanical treatment of molecules	22
4.1.1. Calculation of molecular electronic wave functions	22
4.1.2. Potential energy surfaces, nuclear motion and Franck-Condon principle	24
4.1.3. Coulomb-explosion imaging	26
4.1.4. Isomerization and pump-probe Coulomb-explosion imaging . .	27
4.2. Allene	29
4.2.1. Computed allene geometries and fragmentation pathways	29

4.3.	Software for simulation of ion trajectories in reaction microscopes . . .	34
4.3.1.	Algorithm for the instantaneous fragmentation simulation . . .	34
4.3.2.	Algorithm for simulation of delayed Coulomb-explosions . . .	38
4.4.	Simulated allene fragmentation spectra	40
4.4.1.	Introduction to time-of-flight correlation spectra	40
4.4.2.	Simulated recoil ion spectra	41
4.4.3.	Simulated two body Coulomb-explosion spectra	42
4.4.4.	Simulated three body Coulomb-explosion spectra	43
5.	Laser induced Coulomb-explosion of allene - Experimental results	49
5.1.	Previous experiments on allene molecules	49
5.2.	Conducted IR single pulse experiments	50
5.2.1.	Time-of-flight spectrum and identification of fragments	51
5.2.2.	Time-of-flight correlation spectra and identification of coincidences	52
5.2.3.	Kinetic energy releases measured with IR pulses	57
5.2.4.	IR pulse parameter variation and branching ratios	65
5.2.5.	Half-life of metastable allene dications	70
5.3.	Conducted XUV single pulse experiment	78
5.4.	Conducted XUV-IR Pump-probe experiment	79
6.	Summary and outlook	82
	Appendices	84
A.	Atomic unit system and other non-SI units	85
B.	Estimation influences of the earth's magnetic field on electron trajectories	86
C.	Estimation of experimental KER uncertainty	88
D.	KERs measured with XUV pulses	90
E.	Detection efficiency and drawbacks of high count rates	91
F.	Bibliography	94

Nomenclature

HHG	high harmonic generation
IR (light)	infrared (light)
KER	kinetic energy release
MCP	micro-channel plate
PES	potential energy surface
ReMi	reaction microscope
TDC	time to digital converter
Ti:Sapphire	titanium-doped sapphire
ToF	time-of-flight
XUV (light)	extreme ultraviolet (light)

1. Introduction

Spectroscopic observations like the Balmer series of the hydrogen spectrum [Bal85], the photoelectric effect [Her87] and the black-body radiation [Kir60] gave a crucial impetus for the development of quantum mechanics. Since then increasing energy resolution of spectroscopy has led to discoveries that could not be explained by established theories. A prominent example is a discrepancy from Dirac's model measured by W. LAMB [LR47] in 1947 triggering research that eventually led to the development of quantum electrodynamics.

New spectroscopic techniques that reach unprecedented frequency resolutions became accessible with the invention of lasers in the 1960s. Today sophisticated spectroscopic experiments are for example used in atomic fountain clocks for time standards [SLL⁺99] or in precision spectroscopy to measure drifts in fundamental constants [FKZ⁺04]. The use of frequency combs as first performed by T. W. HÄNSCH enabled absolute frequency measurements with spectroscopic precision [NHR⁺00].

While energy resolution was the driving motor in many fields of physics, advances in temporal resolution of reaction mechanisms were mostly done in chemical sciences. Flow tubes in which reactants were observed at different distances allowed observation of reaction dynamics on sub-second time scales [HR23]. In 1967 M. EIGEN, R. G. W. NORRISH AND G. PORTER were awarded the Nobel prize in Chemistry "for their studies of extremely fast chemical reactions, effected by disturbing the equilibrium by means of very short pulses of energy" [Nob] that had been performed around 1950 and had reached microsecond time scales.

The introduction of pulsed laser technology led – via the nano- and picosecond regimes – to time resolutions of femtoseconds. A. H. ZEWAIL was awarded the Nobel prize in Chemistry in 1988 for his pump–probe experiments with ultrashort laser pulses that reached time resolutions below 10 fs [Zew88]. This work laid the foundation of a new scientific field, the *femtochemistry*. The pump–probe technique uses two laser pulses that are separated temporally by a variable time delay. The pump pulse triggers a reaction by excitation or ionization of the target molecule until it is probed by the probe pulse.

Early experiments on reaction mechanisms were typically based on macroscopic samples and observables and they were thereby part of physical chemistry. Today pump–probe experiments with intense laser pulses are able to investigate the dynamics of single molecules on a quantum level providing a powerful tool for chemical physics that led to a number of new discoveries. From the 1990s onwards, for instance,

vibrational wave-packet dynamics have been observed in different diatomic molecules like I_2 [SCC95] and later H_2 [ERF⁺05].

Due to only one degree of freedom in internuclear motion, theoretical understanding of diatomic molecules is rather advanced in comparison to medium sized molecules, consisting of three to ten atoms. But especially the latter are highly interesting. Some of them change their geometry upon excitation. The created isomers often feature completely new chemical properties. Therefore a better understanding of their formation might enable us to create new substances or even steer chemical reactions with laser pulses.

However, very few experiments with the pump-probe method have so far been conducted on such targets [JRH⁺10]. More commonly single, ultrashort pulses in the femtosecond regime are used to investigate isomerization processes, especially hydrogen migration, of molecules like acetylene (C_2H_2) [ALO⁺06], allene (C_3H_4) [XOY09a] or 1,3-butadiene (C_4H_6) [ZRX⁺12]. In these experiments the durations of the molecular dynamics are extracted indirectly, for example from angular distributions of fragments created in Coulomb-explosions. Direct measurement of isomerization times, however, is not possible without a probe pulse.

In this work a titanium-sapphire laser system is used to create laser pulses in the near infrared with pulse lengths of 10 fs and pulse energies of 1 mJ at a repetition rate of 8 kHz. With our setup, pump-probe experiments with extreme ultraviolet pulses and infrared pulses can be performed at a repetition rate that is superior to that of other sources of such pulses. The extreme ultraviolet pulse is the perfect pump pulse to investigate isomerization processes of charged molecular ions because many target gases can be double ionized by a single highly energetic photon. This results in excitation to selected states through a process relatively well understood by theory.

In the experiments conducted within the framework of this thesis, laser pulses are focused into a cold jet of target molecules within a reaction microscope. Three-dimensional momenta of all charged particles created by laser induced ionization or fragmentation are measured over the full solid angle, allowing a kinematically complete study of reactions.

As a part of this thesis Coulomb-explosion imaging experiments on allene (C_3H_4) were performed and the acquired data was analyzed. Experiments on medium sized target molecules were conducted for the first time with our laser system and reaction microscope. Therefore single pulse experiments are carried out to provide a benchmark for our experimental setup by comparing results with previous publications. Experience gathered in these measurements may be used in future pump-probe experiments on medium sized target molecules with extreme ultra violet and infrared laser pulses. To our knowledge, such experiments have not been reported before. As a first step in this direction a pump-probe experiment on allene molecules was conducted as part of this thesis.

Chapter 2 gives a brief introduction to the creation of ultrashort laser pulses and the

creation of extreme ultraviolet pulse trains by high harmonic generation. Theoretical aspects of pulse creation, pulse propagation through dispersive media and the high harmonic generation process are explained. Chapter 3 describes the reaction microscope and charged particle trajectories within its electric and magnetic field. A software for simulation of electron trajectories within these fields has been developed as a part of this thesis. It is used to create simulated electron spectra which are compared with experimental data to detect field inhomogeneities within the reaction microscope. A quantum mechanical treatment of molecules is introduced in chapter 4 with focus on potential energy surfaces which are fundamental for the Coulomb-explosion imaging measurements performed in this work. Predicted fragmentation channels of allene are introduced and simulated with a Monte-Carlo simulation developed as a part of this thesis. Finally, results of Coulomb-explosion imaging experiments – with single laser pulses and in a pump–probe configuration – are presented in chapter 5.

2. Creation of ultrashort laser pulses

Contents

2.1. Theoretical background	4
2.2. Laser system and high harmonic generation	7

2.1. Theoretical background

The experiments on laser induced molecular dynamics presented in this work have been performed with ultrashort and intense laser pulses. The foundation of such pulses are mode-locked laser oscillators described in 2.1.1. Due to their broad frequency spectrum such pulses are subject to undesired dispersive effects (section 2.1.2). The laser pulses are further spectrally broadened via nonlinear effects in order to achieve pulse lengths of only a few femtoseconds (section 2.1.3). The last part (section 2.1.4) gives a short introduction to high harmonic generation, a method to create coherent pulses in the ultraviolet and near x-ray regime that are used in some of the experiments presented in this work.

2.1.1. Modelocking

Within a laser cavity of length L , standing light waves of angular frequency ω_q are created with a frequency separation of $\Delta\omega_L = \pi c/L$. Here c denotes the speed of light in vacuum¹. In general, these longitudinal modes oscillate independently and their phases $\Phi_{\omega_q}(t)$ are not fixed with respect to each other. Modelocking is achieved, if the amplified cavity modes have fixed phases Φ_{ω_q} [Spe09, p. 7]. In this case the electric field $E(t)$ at a fixed position in space created by $(2n + 1)$ longitudinal modes of frequency $\omega_q = \omega_0 + q\Delta\omega_L$ is given by

$$E(t) = \sum_{q=-n}^n E_{\omega_q} e^{i(-\Phi_{\omega_q})} e^{i\omega_q t} \quad (2.1)$$

with the amplitudes of the cavity modes E_{ω_q} . $E(t)$ describes laser pulses created by constructive interference of the longitudinal modes. The time between two laser pulses is given by $\tau_{rep} = 2L/c$ [Kre09, p. 30]. The repetition rate is given by $1/\tau_{rep}$.

¹For cavities filled with a medium of refractive index n , c must be replaced by $c' = c/n$.

The temporal length $\Delta\tau$ of these laser pulses is related to the total width of the spectrum and the phases Φ_{ω_q} via a Fourier transform of the envelope function. The maximum number of amplified cavity modes is typically limited by the amplification bandwidth of the lasing medium [Spe09, p. 8].

2.1.2. Propagation of laser pulses

The frequency dependent refractive index $n(\omega)$ of optical media like glass or even air influences the propagation of ultra short laser pulses because the phase velocity $v_{ph}(\omega) = c/n(\omega)$ and the wave vector $k(\omega) = \omega/v_{ph}(\omega)$ are non-constant over the large spectral bandwidth.

The electric field $E(z, t)$ of a laser pulse propagating in z -direction can be expressed by a Fourier transform

$$E(z, t) = \frac{1}{\sqrt{2\pi}} \int \tilde{s}(z, \omega) e^{i\omega t} d\omega = \frac{1}{\sqrt{2\pi}} \int s(0, \omega) e^{i\Phi(z, \omega)} e^{-\lambda(z, \omega)z} e^{i\omega t} d\omega. \quad (2.2)$$

Here $|s(0, \omega)|$ denotes the spectral amplitude at $z = 0$ and $\Phi(z, \omega)$ denotes the spectral phase which describes the effects of dispersive media on the phase relation between different spectral components. It has no effects on the spectral composition of the laser pulse, but can alter the temporal shape of the pulse. Absorption of frequency components is described by $e^{-\lambda(z, \omega)z}$.

$\Phi(z, \omega)$ can be written as a Taylor expansion at $\omega = \omega_0$

$$\Phi(z, \omega) = \sum_{j=0}^{\infty} \frac{1}{j!} \left. \frac{\partial^j \Phi(z, \omega)}{\partial \omega^j} \right|_{\omega=\omega_0} (\omega - \omega_0)^j \quad (2.3)$$

with the center frequency ω_0 [Fis10, p. 30]. To describe femtosecond pulses propagating through a dispersive medium sufficiently well, only terms up to $j = 3$ are considered. It can be shown that the first two terms influence the carrier envelope phase and the velocity of the pulse envelope (called group velocity). These terms do not modify the shape of the pulse envelope.

The third term describes a frequency dependent phase velocity the so called linear chirp. For a non-vanishing linear chirp, the pulse envelope is stretched. Higher orders $\mathcal{O}(\omega^3)$ of the Taylor expansion are called nonlinear chirp which can for example cause satellite pulses [Spe09]. Both, linear and nonlinear chirp, must be minimized and compensated for in order to keep the laser pulses short and the intensity high.

2.1.3. Spectral broadening of laser pulses

Laser pulses created by a chirped pulse amplification system have typical pulse lengths of approximately 30 fs. Further pulse compression requires a broadening of the frequency spectrum. This is achieved by self-phase modulation due to an intensity

refractive index [DRo6, p. 193]

$$n = n_0 + \bar{n}_2 I(t). \quad (2.4)$$

The intensity $I(t)$ has different magnitudes at different parts of the laser pulse. “[They] will ‘feel’ different refractive indices, leading to a phase change across the pulse [...]” [DRo6, p. 196] which results in a temporal chirp. The leading edge of the pulse is shifted towards smaller frequencies and the trailing edge is blue-shifted. Mere self-phase modulation does not change the length of the pulse envelope, but the intensity dependent refractive index causes a spectral broadening which allows further pulse compression. This is described in section 2.2.2.

2.1.4. High harmonic generation

Media with a dielectric polarization

$$P(E) \propto \chi^{(1)}E + \chi^{(2)}E^2 + \chi^{(3)}E^3 + \chi^{(4)}E^4 + \dots \quad (2.5)$$

that responds in a nonlinear way to an incident electric field E , are known since the 1960s when second harmonic generation was first observed in optical frequencies [FHPW61]. Since then, available field strengths increased rapidly and higher order nonlinear processes like third harmonic generation could be accessed. The intensities of higher order harmonics, however, decrease because the amplitudes of the susceptibilities $\chi^{(i)}$ fall fast with the order of i . Unexpected observations were made in the end of the 1980s: focusing a high intensity laser into rare gases produces very high order harmonics and, most importantly, their intensities are nearly constant over a wide range up to a certain cutoff energy [LLF⁺89]. An intuitive, semi-classical model [Cor93], the so-called three-step model, describes this process of high harmonic generation (HHG) in gases (compare figure 2.1):

1. The atomic potential is distorted by the strong electric field of the high intensity laser pulse. An electron escapes through the formed potential barrier in a tunnel ionization process. This happens preferably at every half-cycle of the carrier frequency when the amplitude of the electric field is maximized.
2. The trajectory of the freed electron within the laser field is calculated classically. The electric potential of the remaining ion and the magnetic field of the laser are neglected. First, the laser field accelerates the electron away from the ion until the field changes its direction and, after half an optical cycle, accelerates the electron back towards the ion².

²Linear polarized light is crucial for HHG because the electron’s motion within circular polarized light does not result in closed trajectories and the electron will not return to the vicinity of the ion.

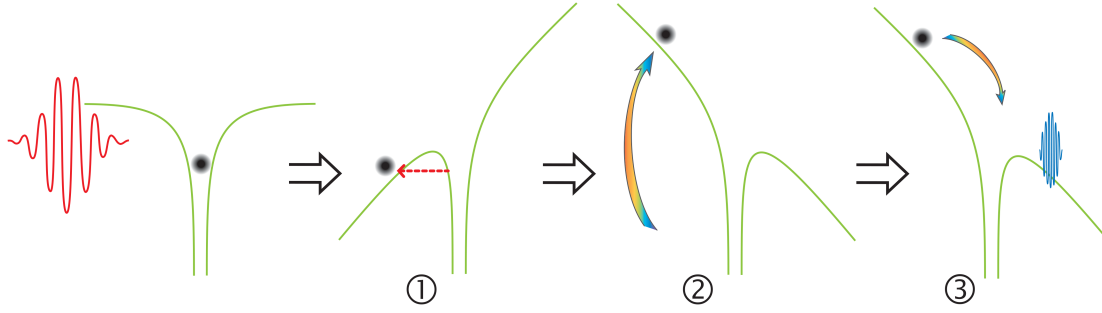


Figure 2.1.: Three step model for HHG with intense laser fields (red pulse). The atomic potential (green) is distorted by the external laser field and an electron (black dot) tunnels through the potential barrier. It gains kinetic energy in the electric field. If it eventually recombines with the ion, there will be a chance that a highly energetic photon is emitted (blue pulse). Figure taken from [Rie07].

3. The highly energetic electron will eventually interact with the ion which is described quantum mechanically in this model. Upon recombination, the system can emit the gained kinetic energy in a single, extreme ultra violet (XUV) photon of high energy. Elastic and inelastic scattering processes (which are the dominating effects) do not contribute to the creation of high harmonics.

The three step model explains the experimentally measured intensity plateau and predicts the cutoff energy of the high harmonics to a very good degree. Improvements of the three step model take additional effects like the ion's Coulomb potential [LBI⁺94] into account, but the qualitative mechanism of the explained model is still valid.

Due to the tunneling mechanism, the HHG process repeats every half-cycle of the carrier frequency and the XUV light is emitted as train of attosecond pulses. The number of XUV pulses within the pulse train depends on the length of the original infrared pulse. Attosecond pulse trains are referred as XUV pulses in this thesis.

2.2. Laser system and high harmonic generation

The laser system used in this work can be separated into three major parts: the first parts of the beam line are the titanium-sapphire oscillator and the amplifier system which creates infrared (IR) pulses of 32 fs length (section 2.2.1). In a second step, the hollow fiber and chirped mirror compressor (section 2.2.2) reduce the pulse length to approximately 10 fs. At last the HHG chamber (section 2.2.3) is used to create XUV light from the IR pulses.

2.2.1. Titanium-sapphire oscillator and amplifier

The basis for all experiments presented in this work is a tabletop laser system that consists of a laser oscillator and an amplification system. Created laser pulses have a center wavelength of 785 nm at an average power of 8 W. The energy of each pulse is 1 mJ at a repetition rate of 8 kHz.

The laser pulses are generated in multiple steps, beginning with a modelocked titanium-doped sapphire (Ti:Sapphire) laser oscillator, the model *MTS-I* manufactured by *Kapteyn-Murnane Laboratories* (light yellow box in figure 2.2). The oscillator is pumped by a *Verdi* continuous wave neodymium-doped yttrium orthovanadate solid state laser with 6 W output power manufactured by *Coherent*. At a repetition rate of 80 MHz, a pulse length of 18 fs and an average power of 680 mW, the peak intensity of the oscillator pulses is too low for effective HHG (compare sections 2.1.4 and 2.2.3) and multi-photon ionization of molecules (compare chapter 5).

The pulse energy is increased by several orders of magnitude to 1 mJ per pulse in a *chirped pulse amplification* system, the *Dragon* amplifier of *Kapteyn-Murnane Laboratories* (green box in figure 2.2). The central part of this amplifier is a cryogenic Ti:Sapphire crystal pumped by a Q-switched and frequency doubled 100 W Neodymium-doped yttrium aluminum garnet laser produced by *Lee Lasers Inc.*

Direct amplification of the very short oscillator pulses is impossible, because created peak intensities would destroy the amplifier crystal. Instead the pulse length is increased by a combination of a grating and several mirrors (labeled *Stretcher* in the green box of figure 2.2). They introduce a wavelength dependent optical path length which results in a stretched and chirped pulse (therefore the name chirped pulse amplification). This lowers the peak intensities within the amplifier crystal to a reasonable amount during pulse amplification.

Creation of pulse energies in the order of 1 mJ at the high repetition rate of the oscillator would require high pump powers which are technically not available. To overcome this problem, a combination of polarizers and a Pockels cell (labeled *Pockels cell* in the green box of figure 2.2) reduce the repetition rate from 80 MHz to 8 kHz before amplification.

The remaining, stretched oscillator pulses are focused on the pumped amplifier crystal and cause stimulated emission of photons (labeled *Ring amplifier* in the green box of figure 2.2). The laser pulses pass the Ti:Sapphire crystal 13 times during the amplification and are directed into a compressor stage afterwards (labeled *Compressor* in the green box of figure 2.2). Here the pulses are compressed to a length of 32 fs with a combination of gratings and mirrors, similar to the stretcher.

2.2.2. Hollow fiber and chirped mirror compressor

The temporal resolution of many experiments on atomic or molecular dynamics depends on the length of the involved laser pulses. Furthermore, short pulses have

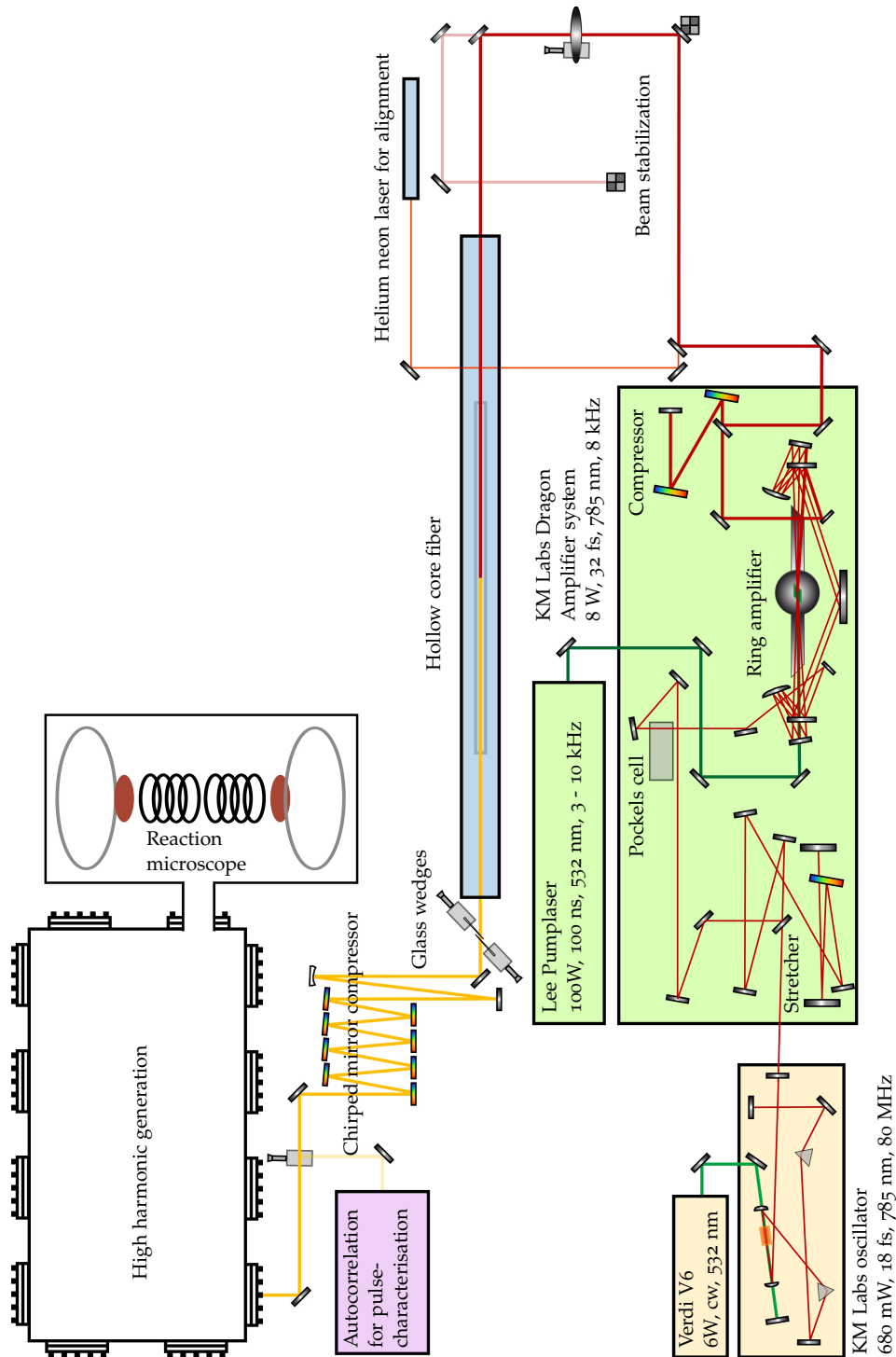


Figure 2.2.: Schematics of a femtosecond laser system. Pulses created by this system were required to perform the experiments described in chapter 5.

an increased peak intensity. The spectral width of the 32 fs pulses from the *Dragon* amplifier is too narrow for further compression. Self-phase modulation described in section 2.1.3, however, allows to broaden the spectrum of the pulses by focusing them into a medium.

In this experiment a hollow core fiber (labeled *Hollow core fiber* in figure 2.2) with a diameter of 250 μm and a length of 1 m is filled with neon at a pressure of 3.5 bar. The laser pulses are focused into the capillary with a lens of 1.5 m focal length and the beam is confined over the whole length of the fiber. The peak intensity decreases over the fiber length because the pulses are stretched by higher order dispersion within the fiber. As a result the efficiency of self-phase modulation decreases as well. This is the reason why a longer fiber length does not necessarily result in a broader spectrum.

The chirped, but spectrally broadened, pulses are compressed by chirped mirrors (named *Chirped mirror compressor* in figure 2.2) which reflect different wavelengths in “different depths” of their coating. A pulse length of approximately 10 fs is achieved behind the compressor. A pair of glass wedges on translation stages allow to increase (or decrease) the amount of dispersive material in the beam line and to fine tune the pulse length.

2.2.3. High harmonic generation chamber

Within the evacuated HHG chamber (sketched in figure 2.3) highly energetic XUV photons are created from the IR pulses coming from the chirped mirror compressor. XUV light is effectively absorbed by air, therefore this chamber is connected to the ReMi by a differential pumping stage. Inside the HHG chamber, a beam splitter splits the laser beam into two. The IR path is marked red and the XUV path is marked blue in figure 2.3.

XUV path The IR pulses in the XUV path are focused into an aluminum tube (named *HHG target* in figure 2.3) with a 200 μm entrance and 150 μm exit hole. A nonlinear processes in argon is used to create the XUV light. The noble gas flows into the aluminum tube continuously to maintain a pressure of about 100 mbar and to replace argon that has escaped through the entrance and exit holes. To keep the low pressure in the main chamber, the HHG target is placed within an additional chamber that is pumped separately. A 0.2 μm thick aluminum filter (labeled *Al filter* in figure 2.3) is used to block remaining IR light. XUV light with photon energies above 17 eV is transmitted by the aluminum filter whose transmittance is given in figure 2.4. Afterwards the divergent XUV pulses are focused by two grating incident mirrors – trough a hole in the parabolic mirror – into the reaction volume of the reaction microscope (labeled *ReMi* in figure 2.3).

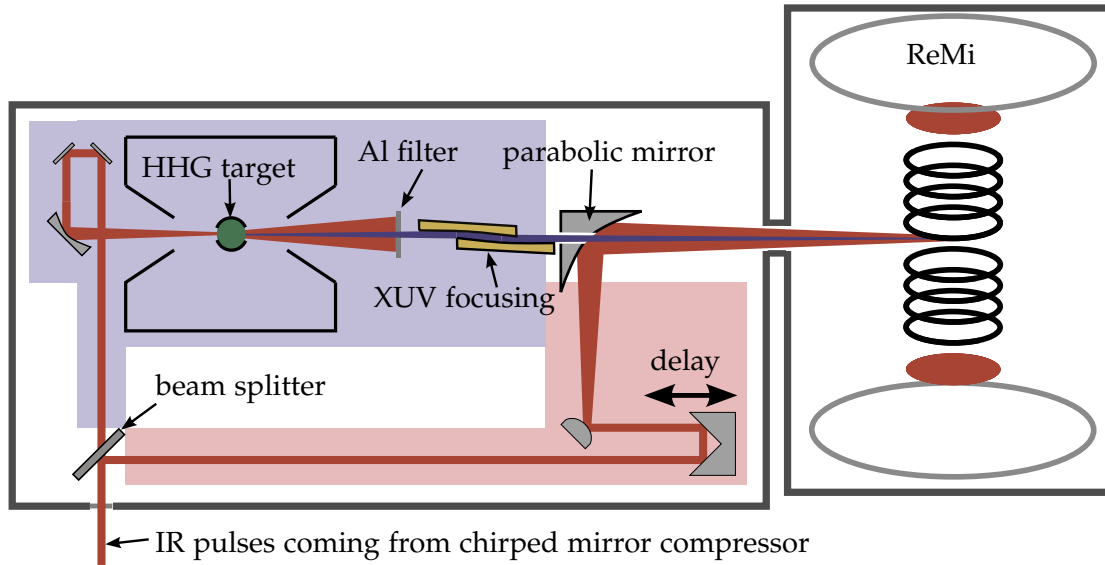


Figure 2.3.: Simplified schematics of the HHG Chamber. IR path and IR light are colored red. XUV path and XUV light are colored bluish.

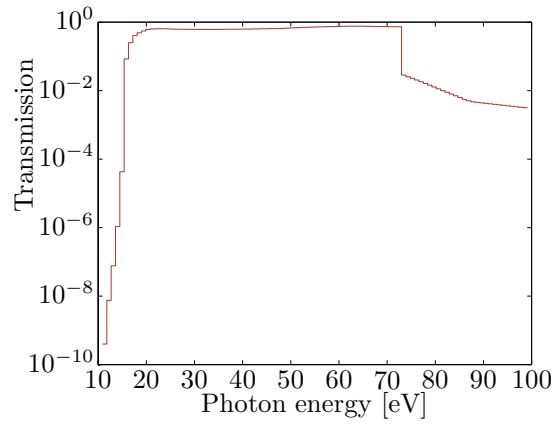


Figure 2.4.: Transmittance of 0.2 μm aluminum filter [fXRO].

IR path The IR pulses in the IR path are focused into the ReMi by a parabolic mirror. The main component in the IR path is a retroreflector on a motorized translation stage. It can be used to change the delay between the IR and XUV pulses. This is necessary for time dependent pump–probe measurements.

Both paths, XUV and IR, can be blocked separately which allows single pulse experiments with either XUV or IR pulses as well as pump–probe measurements requiring both pulses. Furthermore a motorized aperture in the IR path allows to adapt the intensity of the IR pulses.

3. Reaction microscope

Contents

3.1. Functional principle of reaction microscopes	13
3.2. Trajectories of charged particles within reaction microscopes	14
3.3. Software for simulation of electron trajectories in reaction microscopes	16
3.4. A comparison of simulated electron spectra with experimental data	18

The primary measurement tool in this work is a reaction microscope (ReMi) to detect (molecular) ions and electrons created in atomic and molecular ionization processes. This chapter begins with an introduction describing the functional principle (section 3.1). Electric and magnetic fields within ReMis guide charged particles towards position sensitive detectors on trajectories described in section 3.2. A software to simulate electron trajectories within the fields of a ReMi was developed as a part of this thesis. It is introduced in section 3.3. This chapter ends with a comparison of simulated and experimental electron spectra 3.4.

3.1. Functional principle of reaction microscopes

First conceptual studies on ReMis were carried out in the mid 1990s and experiments followed soon afterwards [MUU⁺94, MUS⁺96]. Since then ReMis have been continuously improved and developed into sophisticated devices to observe atomic and molecular fragmentation processes [UMD⁺03]. A sketch of a typical ReMi with its basic components is depicted in figure 3.1.

While ReMis exist in a great variety and are often developed for a single type of experiment, the principle of operation is always the same: An ionizing source interacts with a supersonic target gas jet within a small reaction volume. The charged reaction products, namely electrons and positive ions, are guided by homogeneous electric and magnetic fields towards the position sensitive detectors based on micro-channel plates (MCPs) and delay line anodes. For each particle the time-of-flight (ToF) and hit position on the respective detector is measured independently. With these values the particle's trajectory within the electric and magnetic fields can be reconstructed. This allows to determine the three-dimensional momenta of the ionization products – and therefore

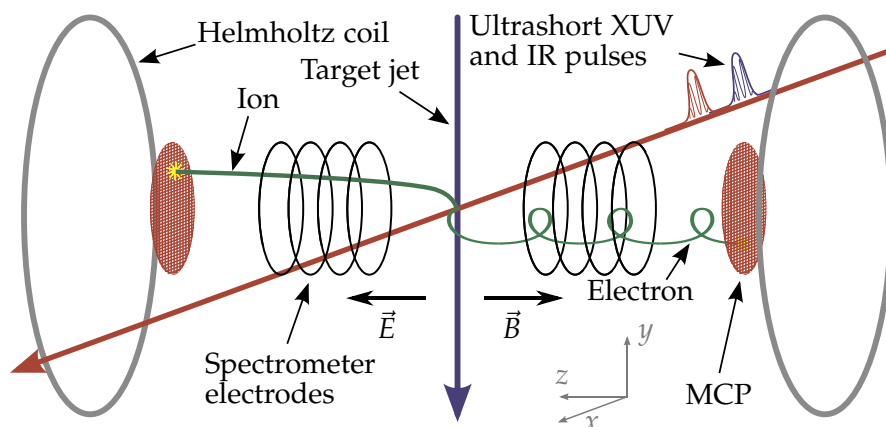


Figure 3.1.: Sketch of a ReMi with main components. Interaction of laser pulses with the target molecules creates charged fragments that are guided towards position sensitive detectors by an electric and magnetic field.

the kinetic energies – at the time of their creation. Charged reaction products can be detected over the full solid angle.

A fundamental requirement for the momentum reconstruction are highly homogeneous fields supplied by spectrometer electrodes and a pair of Helmholtz coils. The design as well as the construction of a ReMi is technically challenging [Fiso3]. The construction of the specific ReMi used throughout this thesis is documented by R. GOPAL [Gop10].

For the purposes of this thesis the axis parallel to the electric field is defined as z -axis or spectrometer axis. The laser propagation direction is orthogonal to z and determines the x -axis. The target gas jet propagates in inverse y -direction. This coordinate system is also depicted in figure 3.1. If not indicated otherwise, the laser is polarized parallel to the z -axis throughout this work.

3.2. Trajectories of charged particles within reaction microscopes

For momentum reconstruction of charged particles a reconstruction of their trajectories within the fields of a ReMi is required. The general equation of motion for a charged particle of mass m and charge q in an electric field \vec{E} and a magnetic field \vec{B} can be written as

$$\vec{F}(\vec{r}) = q \left(\vec{E} + \dot{\vec{r}} \times \vec{B} \right) = m \ddot{\vec{r}}. \quad (3.1)$$

For the general case it is not possible to solve these coupled differential equations analytically. In the special case of an ideal ReMi, however, the above equations decouple and analytic solutions exist. These are introduced below.

3.2.1. (Positive) ions

Effects of the magnetic field on positively charged (molecular) ions can be neglected in most cases, due to their large mass. The electric field is assumed to be homogeneous and parallel to the spectrometer axis. With these constraints, the initial momentum p_{z_i} in z-direction of an ion with measured time-of-flight T_i is calculated by¹

$$p_{z_i} = \frac{lm_i}{T_i} - \frac{1}{2} \frac{Uq_i}{l} T_i. \quad (3.2)$$

Here l denotes the acceleration length between reaction volume and MCP detector and U denotes the acceleration voltage over this length. The acceleration voltage is related to the homogeneous electric field E_z by $U = E_z l$. The ion's mass and charge is given by m_i and q_i . The initial transverse momenta p_{x_i} and p_{y_i} are calculated by

$$\begin{pmatrix} p_{x_i} \\ p_{y_i} \end{pmatrix} = \begin{pmatrix} x \\ y \end{pmatrix} \frac{m_i}{T_i} \quad (3.3)$$

where (x, y) denotes the measured hit position on the ion detector.

3.2.2. Electrons

Due to their small mass compared to the positively charged ions, electrons can gain very high kinetic energies in typical ionization processes. A magnetic field is applied in negative z-direction to force electrons on cyclotron trajectories. This significantly increases the detector acceptance for fast electrons. The z-component p_{z_e} of the electron's initial momentum is unaffected by the magnetic field. It is calculated by equation 3.2 if m_i and q_i are replaced by the electron mass m_e and elementary charge e .

The calculation of the radial momenta is more complicated due to the magnetic field B_z in z direction. A trajectory of an electron projected on the detector plane within the ReMi is depicted in figure 3.2. The absolute value of the electron's radial initial momentum $|\vec{p}_{r_e}|$ is calculated by

$$|\vec{p}_{r_e}| = \frac{\omega_c m_e |\vec{r}|}{2 |\sin(\alpha/2)|} \quad (3.4)$$

with the cyclotron frequency $\omega_c = |e| B_z / m_e$, angle $\alpha = \omega_c T$ (as defined in figure 3.2) and measured hit distance $|\vec{r}|$ from detector center. The azimuthal angle φ gives the initial momentum's direction in the x, y -plane and is calculated by:

$$\varphi = \Phi + \frac{\omega_c T (\bmod 2\pi)}{2}, \quad (3.5)$$

where Φ denotes the azimuthal angle of the measured hit position on the detector plane. The interested reader is referred to A. SENFTLEBEN [Sen09] for more information and a derivation of the formulas above.

¹Some ReMIs incorporate an additional drift length without an electric field. This is not the case for the ReMi used in this work. Therefore all formulas are given without a drift length.

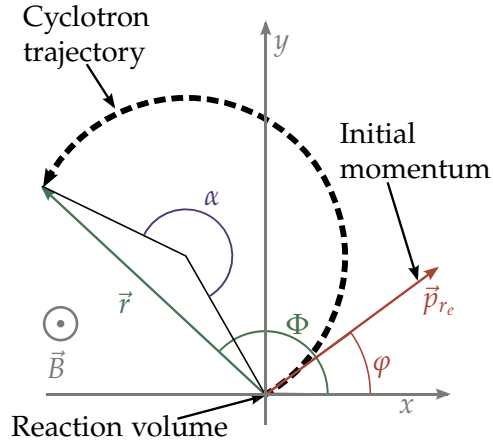


Figure 3.2.: Electron trajectory within a ReMi projected onto the detector plane.

Equation 3.4 shows the downside of adding a magnetic field: For certain ToFs, when $\sin(\alpha/2) = 0$, the calculated momentum $|\vec{p}_{re}|$ diverges. Therefore it is important to choose the magnetic and electric fields in a way that this situation does not occur for momenta which are of interest. This is often challenging and sometimes impossible. The desired acceptance for electrons and ions with different energies creates additional constraints on these parameters, e.g. too weak magnetic fields cannot confine electrons with high radial velocities while high electric fields are required to confine positive ions with a high momentum in radial direction.

3.3. Software for simulation of electron trajectories in reaction microscopes

As mentioned before, choosing correct field parameters in the ReMi is crucial to obtain useful data during an experiment. In this work a Monte Carlo simulation of electron trajectories within a ReMi was developed. The simulation is based on the Go4 data analysis framework that is being developed at the GSI Helmholtzzentrum für Schwerionenforschung in Darmstadt [AMATB⁺11]. The Go4 framework is also used for ReMi data analysis in this thesis.

There are two main applications for the simulation of electron trajectories. First simulation of electrons with expected energies can help to determine useful field parameters before even starting an experiment. This can save valuable beam time. Furthermore it is possible to simulate magnetic fields tilted with respect to the spectrometer axis. Such field inhomogeneities exist in all real world ReMIs because of imperfectly aligned Helmholtz coils or influences of the earth's magnetic field. Comparison of experimental data with simulated spectra can reveal such field inhomogeneities.

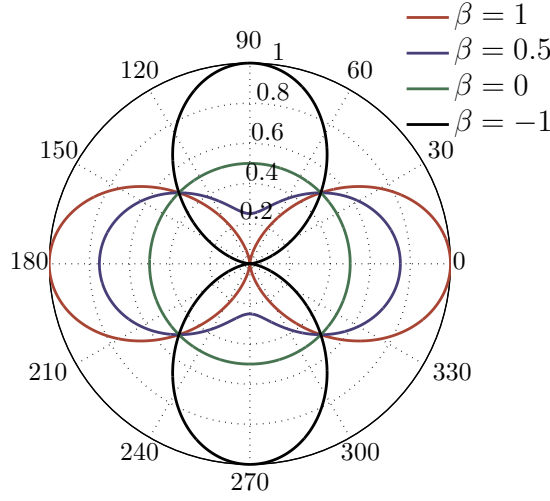


Figure 3.3.: β -parameter: $P(\vartheta) = 0.5 + \beta (\cos(\vartheta)^2 - 0.5)$. $\beta = 0$ describes an isotropic distribution, while $\beta \neq 0$ introduces an anisotropy. In this thesis β -parameters are used to introduce randomized angular distributions in the Monte Carlo simulations.

In the software, electrons are simulated with an initial kinetic energy which is randomized by a Gaussian probability distribution to describe effects from the broad energy spectrum of the ultrashort and spectral broadened laser pulses. The mean value and the variance of this distribution are set as input parameters. The absolute value of the electron's initial momentum \vec{p}_e is calculated from the kinetic energy.

A probability distribution of the angle ϑ

$$P(\vartheta) = 0.5 + \beta (\cos(\vartheta)^2 - 0.5), \quad \beta \in [-1, 1] \quad (3.6)$$

is used to randomize the direction of the electron's initial momentum \vec{p}_e . $P(\vartheta)$ is drawn in figure 3.3 for different values of β . In the simulation, ϑ is the polar angle to an axis of symmetry.

The application of the β -parameter shall be explained with an example: if the laser polarization was parallel to the spectrometer axis (z-axis) and an anisotropic angular distribution of the created photo electrons was expected due to the laser polarization, the z-axis would define an axis of symmetry. To simulate electrons that are ejected preferably along the laser polarization, β must be chosen larger than zero, for example $\beta = 0.5$ (compare figure 3.3), and the z-axis must be chosen as the symmetry axis. Both, the β -parameter and the direction of the axis of symmetry, are input parameters of the software. Due to the cylindrical symmetry, the momentum distribution orthogonal to the axis of symmetry is always simulated as isotropic.

To create ToF spectra or spectra incorporating the detector position, trajectories of electrons with initial momentum \vec{p}_e are simulated within the ReMi fields. ReMi

parameters like acceleration length l and acceleration voltage U , as well as the magnetic field \vec{B} are defined as input parameters. The method of trajectory simulation depends on the angle between the magnetic field \vec{B} and the spectrometer axis. If the magnetic field is parallel to the spectrometers axis, the ToF and hit position can be calculated analytically. In the case of a tilted magnetic field, it is necessary to solve the equations of motion numerically. Both cases are described below.

3.3.1. Parallel electric and magnetic fields

When electric and magnetic fields are parallel, the time-of-flight T is calculated by

$$T = m_e \frac{2l}{p_{z_e} + \sqrt{p_{z_e}^2 + 2m_e e U}}. \quad (3.7)$$

with electron mass m_e and elementary charge e . This equation is obtained by rearranging equation 3.2.

The hit position is calculated in two steps. By rearrangement of equation 3.5, the angle Φ of the detector hit is obtained from the time-of-flight T and the cyclotron frequency ω_c :

$$\Phi = \varphi - \frac{\omega_c T (\bmod 2\pi)}{2} \quad (3.8)$$

with the azimuthal angle $\varphi = \arctan(p_{x_e}/p_{y_e})$ of the initial momentum. The hit radius $|\vec{r}|$ is calculated by rearranging equation 3.4 to

$$|\vec{r}| = 2 \frac{p_{r_e}}{\omega_c m} |\sin(\alpha/2)|. \quad (3.9)$$

The simulated ToF and hit position can be plotted in different types of spectra.

3.3.2. Non-parallel electric and magnetic fields

The coupled differential equations of motion of a charged particle in a magnetic and electric field cannot be solved analytically for non-parallel fields. Therefore a tilted magnetic field requires a numerical integration of equation 3.1. This is done by a Runge-Kutta-4 integrator with adaptive step-size control taken from the Gnu Scientific Library [GDT⁺09] which uses the initial momentum \vec{p}_e of each electron as well as ReMi parameters to calculate the ToF and hit position. Spectra are created similarly to the case of parallel fields.

3.4. A comparison of simulated electron spectra with experimental data

As a part of this thesis, experimental electron spectra have been obtained at different Helmholtz currents as a benchmark for the electron trajectory simulation. It will be

shown that all features in the experimental spectra can be resembled by the simulation. In addition, magnetic field inhomogeneities will be revealed by comparison of simulated and measured electron spectra. In this section, magnitudes of magnetic fields are given in gauss. The conversion to the SI unit tesla is given by $1 \text{ G} \hat{=} 1 \times 10^{-4} \text{ T}$ (compare appendix A).

The experiments described in the following sections have been performed with ^{40}Ar as a target gas. The noble gas was single ionized by XUV photons with energies $E_{h\nu}$ that were created by HHG. Due to energy conservation, ejected electrons had a kinetic energy

$$E_e = E_{h\nu} - E_i. \quad (3.10)$$

Here E_i denotes the ionization potential of ^{40}Ar . A ReMi with an acceleration length of 16.10 cm was used to detect ToF and hit position of photo electrons. It was operated at an acceleration voltage of 44 V.

These values were used as input parameters of the software. The electron energy distributions and their relative intensity were chosen to fit the experimental spectrum at 40 A Helmholtz current. The variance of the Gaussian energy distribution was 0.7 eV and the simulated angular distribution was isotropic in the simulation.

Data acquired at a Helmholtz current of 40 A is presented in the next section. Thereafter results from an experiment with 45 A Helmholtz current are interpreted. By comparing experimental electron spectra with simulated spectra, it will be shown that the magnetic and electric fields are parallel at the lower Helmholtz current. At higher currents, however, a comparison of the experimental spectra with simulated spectra reveals that the magnetic field is tilted by a small angle of approximately 0.5° with respect to the electric field.

3.4.1. Electron spectra at 40 A Helmholtz current

In a first measurement, the Helmholtz coils of the ReMi were operated at 40 A. In figure 3.4 the radius of the measured electron hit position is plotted over the measured ToF.

The most prominent feature in the experimental data are the nodes in the electron hit radius at $T_1 = 45.0 \text{ ns}$, $T_2 = 90.3 \text{ ns}$, $T_3 = 135.7 \text{ ns}$. The hit radius is described by equation 3.9 and it equals zero for ToFs that fulfill $T\omega_c = \alpha = 2\pi \cdot i$ with $i \in \mathbb{N}$. Therefore the separation ΔT between two nodes depends on the cyclotron frequency $\omega_c = |e| B_z / m_e$. This is used to calculate the magnitude of the magnetic field B_z within the ReMi by

$$B_z = \omega_c \frac{m_e}{|e|} = \frac{2\pi}{\Delta T} \frac{m_e}{|e|} = 7.9 \text{ G}. \quad (3.11)$$

The XUV photons in this experiment have a discrete energy spectrum due to their origin from HHG. Due to energy conservation in equation 3.10, the photo electrons have discrete kinetic energies as well. The hit radius depends on the transversal momentum

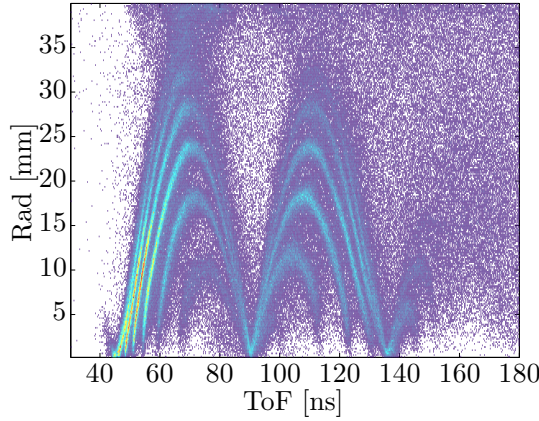


Figure 3.4.: Experimental electron spectra at 40A Helmholtz current. The radius of the detector hit position is plotted over the electron ToF. A logarithmic color scale is used.

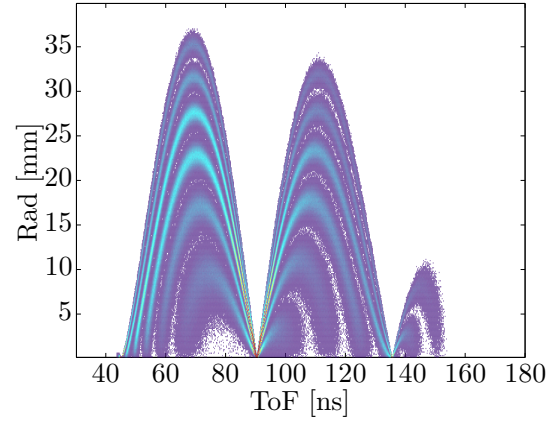


Figure 3.5.: Simulated electron spectra with a magnetic field of $B = 7.9$ G. Magnetic end electric fields are simulated parallel. The radius of the simulated detector hit position is plotted over the simulated ToF. A logarithmic color scale is used.

(compare equation 3.9) and therefore on the kinetic energy. As a result, measured hit radii feature a characteristic band structure shown in figure 3.4.

Electron trajectories have been simulated with a magnetic field parallel to the electric field. Its magnitude of $B = 7.9$ G was extracted from the experimental data. All prominent features of the measurement are reproduced by the simulated spectrum which is plotted in figure 3.5. The nodes of both spectra appear at the similar ToFs. This indicates a correct operation of the software.

3.4.2. Electron spectra at 45 A Helmholtz current

In a second measurement, the Helmholtz coils were operated at 45 A. All other ReMi and laser parameters remained unchanged.

The nodes in figure 3.6 are shifted towards lower ToFs and their separation is smaller than in figure 3.4. Furthermore the radii of the cyclotron trajectories decrease. The separation between the nodes at $T_1 = 81.9$ ns and $T_2 = 122.8$ ns is used to calculate the magnetic field with equation 3.11. Its magnitude is increased to 8.73 G due to the higher Helmholtz current.

Compared to figure 3.4, the band structure in figure 3.6 is more washed out. The energy spectrum of the XUV photons is the same in both measurements and the broadened bands can only be explained by changes in the magnetic field. If photo electron momenta were reconstructed from these hit positions, this would translate into a reduced momentum resolution of the ReMi. To reproduce the broadened band structure in the simulated spectrum, the magnetic field of 8.73 G must be tilted by by a

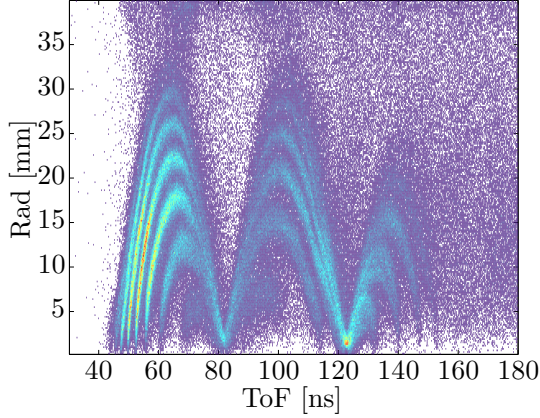


Figure 3.6.: Experimental electron spectra at 45A Helmholtz current. The radius of the detector hit position is plotted over the electron ToF. A logarithmic color scale is used.

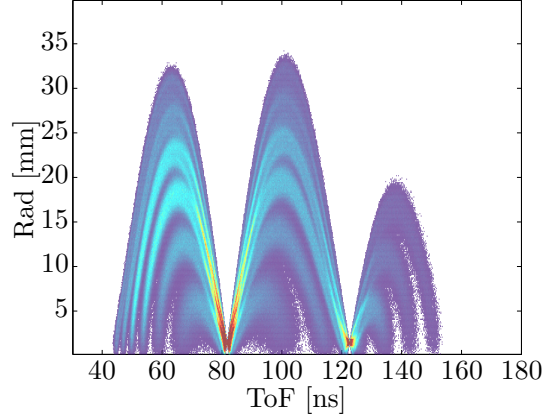


Figure 3.7.: Simulated electron spectra with a magnetic field of $B = 8.73$ G. The magnetic field is tilted by 0.5° with respect to the electric field in the simulation. The radius of the simulated detector hit position is plotted over the simulated ToF. A logarithmic color scale is used.

small angle with respect to the electric field. This angle was chosen 0.5° to create the simulated spectrum in figure 3.7.

This tilt of the magnetic field results from the superposition of the coil's magnetic field with the earth's magnetic field. When constructing the ReMi, the position of the coils was varied in order to get the best results at 40 A. For higher Helmholtz currents, the effective magnetic field has a non-vanishing component perpendicular to the z-axis. According to a crude estimation (see appendix B) the effective magnetic field within the ReMi is tilted by $\approx 0.3^\circ$ with respect to the spectrometer axis at a Helmholtz current of 45 A. This value is consistent with the angle of 0.5° obtained from the simulation. It should be emphasized that the latter is obtained by a qualitative comparison of the features of the two spectra and its uncertainty is at least 0.1° .

It has been demonstrated that the Monte-Carlo simulation is able to reproduce experimental spectra and can be used to analyze field inhomogeneities within the ReMi. A planned upgrade of the software will include momentum reconstruction from simulated ToFs and hit positions. This will allow to simulate the effects of field inhomogeneities on reconstructed electron momenta.

4. Laser induced Coulomb-explosion of allene - Theory

Contents

4.1. Quantum mechanical treatment of molecules	22
4.2. Allene	29
4.3. Software for simulation of ion trajectories in reaction microscopes .	34
4.4. Simulated allene fragmentation spectra	40

This chapter begins with an introduction to quantum mechanical methods and concepts used to describe molecules (section 4.1). In section 4.2, Coulomb-explosion pathways and isomers of allene dications predicted by theory, are presented. Section 4.3 introduces a software to simulate molecule fragmentation within a ReMi which has been developed as a part of this thesis. Simulated allene fragmentation spectra are presented in section 4.4.

4.1. Quantum mechanical treatment of molecules

While the Schrödinger equation of the hydrogen atom is solved in most quantum mechanics textbooks [Scho7, p. 124-129], solving even the smallest molecules is difficult and only possible with numerical methods or approximations. This section gives a short introduction to molecules in quantum physics and how to separate electronic and nuclear motion (*Born-Oppenheimer approximation*) in order to simplify the numerical problem or, in the case of the H_2^+ molecular ion, make it analytically solvable.

4.1.1. Calculation of molecular electronic wave functions

The non-relativistic Hamilton operator \hat{H} of a molecule with I nuclei of masses M_i and charges q_i and J electrons of charge e and mass m_e ,

$$\hat{H} = -\frac{\hbar^2}{2m_e} \sum_{j=1}^J \nabla_j^2 - \frac{\hbar^2}{2} \sum_{i=1}^I \frac{1}{M_i} \nabla_i^2 + V(\vec{r}, \vec{R}) \quad (4.1)$$

contains three terms. The first two describe the kinetic energy of the electrons and nuclei while the third term

$$V(\vec{r}, \vec{R}) = \frac{1}{4\pi\epsilon_0} \left[\sum_{j < j'} \sum_{j'=1}^J \frac{e^2}{|\vec{r}_{j,j'}|} + \sum_{i < i'} \sum_{i'=1}^I \frac{q_i q_{i'}}{|\vec{R}_{i,i'}|} - \sum_{j=1}^J \sum_{i=1}^I \frac{eq_i}{|\vec{r}_{j,i}|} \right] \quad (4.2)$$

is the Coulomb potential of the system [Demo8, p.16]. It depends on the position vectors of electrons $\vec{r} = \vec{r}_1, \dots, \vec{r}_J$ and nuclei $\vec{R} = \vec{R}_1, \dots, \vec{R}_I$. $|\vec{r}_{j,j'}|$, $|\vec{R}_{i,i'}|$ and $|\vec{r}_{j,i}|$ are the distances between pairs of particles. The first term in 4.2 describes the repulsion between pairs of electrons. The second describes the repulsion between pairs of ions and the third describes the attractive potential between electrons and ions.

The Schrödinger equation, with the non-relativistic Hamilton operator \hat{H} (defined in equation 4.1), the energy eigenvalue E and the corresponding eigenstate ψ ,

$$\hat{H}\psi = E\psi, \quad (4.3)$$

is exact if interactions due to nuclear and electronic spins are neglected. Unfortunately, even for the H_2^+ molecular ion – the simplest molecule – no analytic solution of this equation exists [Demo8, p. 15-17]. Numerically, the Schrödinger equation can either be solved with the exact Hamilton operator (equation 4.1) or with a Hamilton operator that has been simplified with physically motivated approximations. If the first method is applied, it is difficult to transfer results obtained for a specific molecule to other species. The second approach will reduce the required computational time and deepens the insight into underlying physical processes. Hence it is pursued in the following sections.

Due to momentum conservation and the large mass ratio M_i/m_e , the nuclei move much slower than electrons. In very good approximation the electrons adapt instantaneously to the frame given by the nuclei. The motion of electrons and nuclei can be separated in this case and the second term in equation 4.1 can be neglected for the calculation of the electronic wave functions and the electronic energies.

In combination with equations 4.1 and 4.2 this gives a purely electronic Hamilton operator

$$\hat{H}_{\text{el}} = -\frac{\hbar^2}{2m_e} \sum_{j=1}^J \nabla_j^2 + \frac{1}{4\pi\epsilon_0} \left[\sum_{j < j'} \sum_{j'=1}^J \frac{e^2}{|\vec{r}_{j,j'}|} - \sum_{j=1}^J \sum_{i=1}^I \frac{eq_i}{|\vec{r}_{j,i}|} \right] \quad (4.4)$$

and an internuclear repulsion

$$V_N = \sum_{i < i'} \sum_{i'=1}^I \frac{q_i q_{i'}}{|\vec{R}_{i,i'}|} \quad (4.5)$$

that only depends on the nuclear positions which are parameters in this approximation. The operators in the resulting electronic Schrödinger equation

$$(\hat{H}_{\text{el}} + V_N) \psi_{\text{el}}(\vec{r}, \vec{R}) = U(\vec{R}) \psi_{\text{el}}(\vec{r}, \vec{R}), \quad (4.6)$$

act only on the electron position and on the wave function [Levo8, p. 370] and no differentiation or integration is done over \vec{R} . The eigentvalues to the electronic wave functions ψ_{el} are given by $U(\vec{R})$. In physical chemistry, equation 4.6 is solved with numerical methods like *self-consistent field Hartee-Fock configuration interaction* [Demo8, p. 73-77].

When equation 4.6 is solved numerically, one finds that for fixed \vec{R} a number of wave functions $\psi_{el} = \psi_{el,n}$ and energy eigenvalues $U(\vec{R}) = U_n(\vec{R})$ exist. Different sets of electronic quantum numbers are denoted by n .

4.1.2. Potential energy surfaces, nuclear motion and Franck-Condon principle

For each molecular state, the total energy of the system is conserved and distributed among the electronic energy $U_n(\vec{R})$ and the kinetic energy of the nuclei. The Hamilton operator \hat{H}_N , describing the nuclear dynamics, can be written as

$$\hat{H}_N = -\frac{\hbar^2}{2} \sum_{i=1}^I \frac{1}{M_i} \nabla_i^2 + U_n(\vec{R}) \quad (4.7)$$

where $U_n(\vec{R})$ is an effective potential which dictates the nuclear motion [Levo8, p. 372]. $U_n(\vec{R})$ is therefore called potential energy surface (PES). The solutions of a Schödinger equation with the Hamilton operator \hat{H}_N are vibrational energies and vibrational wave functions of the nuclei.

For a diatomic molecule, $U_n(\vec{R}_1, \vec{R}_2)$ depends only on the internuclear distance $|\vec{R}_1 - \vec{R}_2|$ and the PESs reduce to curves. These are sketched in figure 4.1 with corresponding vibrational energy levels and wave functions. For a non-linear three atomic molecule, the PESs depend on three independent variables: the internuclear distance of two pairs of nuclei and the opening angle between those bonds. PESs of larger molecules are complicated multi-dimensional structures.

The above described separation of electronic and nuclear motion is called *Born-Oppenheimer approximation* which in general works well for the molecular ground state. Whenever $(U_n(\vec{R}) - U_m(\vec{R}))$ for different sets of electronic quantum numbers n and m gets small (for example if the PESs cross), the Born-Oppenheimer approximation breaks down and the nuclear motion can induce a coupling between electronic states. In this case the molecule cannot be described as a nuclear frame oscillating in the effective potential $U_n(\vec{R})$. This is encountered frequently in excited electronic states [Demo8, p. 24].

In Born-Oppenheimer approximation, transitions between electronic states – excitation, absorption and ionization – happen on time scales which are very fast compared to nuclei dynamics. The parameters \vec{R}_i describing the nuclear frame of the initial state are equal to those describing the final state \vec{R}_f . From a classical point of view, the kinetic energy of the nuclei is conserved during electronic transitions and they occur

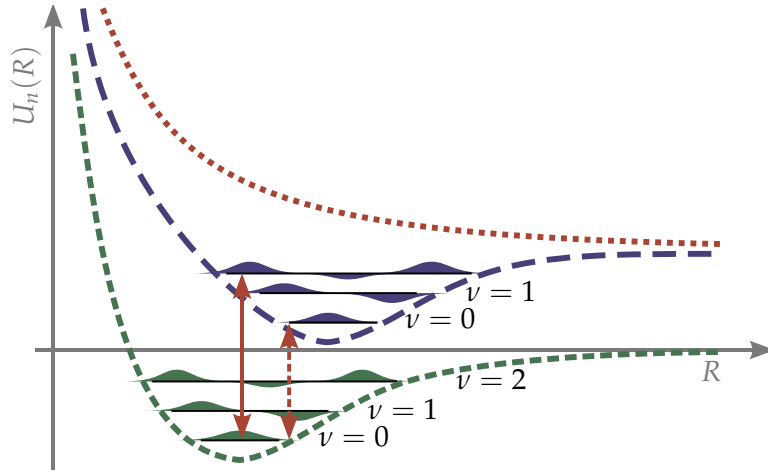


Figure 4.1.: Schematics of bonding (green, blue) and anti-bonding (red) potential energy curves $U_n(\vec{R})$ of a diatomic molecule. The horizontal, black lines correspond to vibrational energy levels of the bound molecule. The solid arrow indicates the vertical ionization energy and the dashed arrow indicates the adiabatic ionization energy.

at internuclear distances \vec{R}^* with $E_{kin}^i(\vec{R}^*) = E_{kin}^f(\vec{R}^*)$ [Dem10, p. 315]. Quantum mechanically the probability for an electronic transition between two vibrational states is related to the *Frank-Condon factor*

$$FC(v_i, v_f) = \left| \int \psi_{v_i}(\vec{R}) \psi_{v_f}(\vec{R}) d\vec{R} \right|^2 \quad (4.8)$$

which describes the overlap integral of the initial vibrational state $\psi_{v_i}(\vec{R})$ and the final vibrational state $\psi_{v_f}(\vec{R})$. Transition probability for a given set of nuclear parameters \vec{R} is described by the integrand in equation 4.8. The integrand is non-zero over a range of \vec{R} due to the finite width of the involved wave functions but it is maximized for $\vec{R} = \vec{R}^*$ in agreement with the classical picture [Dem10, p. 315].

The *vertical ionization energy* is the energy difference between the ground state of a neutral molecule and the ground state of a molecular ion at nuclear parameters for which the integrand in equation 4.8 is maximized. Ionization at such parameters can create vibrationally excited molecular ions, because the local minimums in the PESs of molecular ions are often shifted with respect to those of the neutral molecule, as indicated by the green and blue dashed curves in figure 4.1. The vertical ionization energy is denoted by a solid arrow in the same figure.

The energy difference between the vibrational ground state of the initial electronic state and the vibrational ground state of the final electronic state is called *adiabatic ionization energy* (also called threshold ionization energy). It is always smaller or equal to the vertical ionization energy. In figure 4.1 the adiabatic ionization energy is denoted

by a dashed arrow. Depending on the overlap of initial and final vibrational wave functions, ionization at adiabatic ionization energies is often dramatically suppressed compared ionization at vertical ionization energies. Under certain conditions, however, ionization might occur only at inter nuclear distances with a very small overlap, e.g. for photo ionization with a narrow bandwidth that is detuned from the vertical ionization energy.

Besides the previously discussed bonding PESs¹, anti-bonding PESs exist as well (drawn in figure 4.1 as red curve). Repulsive PESs, especially those of multiply charged molecular ions, can – under certain conditions – be used to determine a molecule's spatial structure from the momentum distribution of the created fragments, as described in the next section.

4.1.3. Coulomb-explosion imaging

Multiple ionization of polyatomic molecules, can – depending on the molecular PESs – trigger decays into several neutral and charged fragments. If all fragments are charged, the repulsive PESs is often approximated by a Coulomb potential and the fragmentation process is called Coulomb-explosion.

In a Coulomb-explosion, the probability density $|\psi_v(\vec{R})|^2$ of the vibrational wave function within the bonding PES is mapped to a distribution of kinetic energies of the final products via the repulsive PES [WSWZ03, p. 411, 412]². This mechanism is shown in figure 4.2 for a two atomic molecule. The sum kinetic energies of all fragments is called kinetic energy release (KER).

For Coulomb-explosion imaging, the method of reconstructing molecular geometries from the fragments' momentum distribution, three conditions must be fulfilled [WSWZ03, p. 411]:

1. All binding electrons need to be removed within a timescale shorter than the vibrational or rotational times of the molecule, in order to map the undisturbed geometry onto the anti-bonding PES.
2. The shape of the anti-bonding PES must be known because its shape quenches (or stretches) the KER distribution compared to the original bond length distribution (as indicated in figure 4.2). In some cases the PES can be approximated by a Coulomb potential but often it has to be calculated.

¹Solving the Schödinger equation 4.6 for varying parameters \vec{R} results in Eigenstates and Eigenvalues that form the PES. Strictly speaking, the electronic state is bonding or anti-bonding, not the PES. For convenience this distinction is not made throughout this thesis.

²A full quantum mechanical treatment requires a calculation of the overlap integral of the initial wave function ψ_v with the final wave function Φ_{KER} . In a semi-classical picture the wave function collapses to a δ -distribution located at the dissociating PES, during the ionization. This approximation neglects the vibration of bound atoms and therefore it ignores the initial velocities of the exploding fragments. In practice, if applied to molecules in the vibrational ground state, the semi-classical approximation will be good enough compared to experimental resolution [WSWZ03, p. 411, 412].

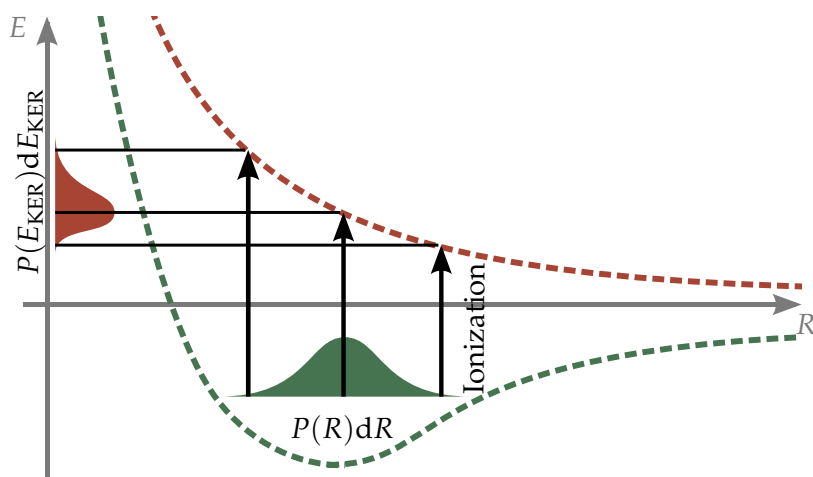


Figure 4.2.: Excitation of molecules to anti-bonding potential energy surfaces is the fundamental principle of Coulomb-explosion imaging. This allows to map bond length distributions onto measured KER distributions of charged fragments. Figure taken from [WSWZ03, p. 412]

3. The cross section of the excitation to the repulsive PES must not depend on the initial molecular geometry.

From a two body Coulomb-explosion, only a single bond length can be extracted. To obtain more detailed structural information it is necessary to produce three or more charged fragments. Then the momentum distribution and (relative) angular distribution of these fragments contains information about bond lengths *and* angles between bonds. This is crucial for the investigation of isomerization processes described in the next section.

4.1.4. Isomerization and pump–probe Coulomb-explosion imaging

The sudden removal of one or multiple electrons causes an electron charge redistribution on a sub-femtosecond timescale, while dynamics of the heavier nuclei appear on a wide range of time scales between a few femtoseconds for protons and up to hundreds of femtoseconds for carbon nuclei [ZRX⁺12]. Such rearrangement of the nuclear frame, called isomerization, has been subject of many experiments [Cor95,SSW⁺05,XOY09a,XOY09b,ZRX⁺12] and theoretical calculations [MBo8,PTS10] during recent years. To reconstruct the equilibrium geometry of a neutral molecule, an instantaneous excitation to the dissociating PES is required, as described in the previous section. For investigation of isomerization processes immediate fragmentation is not desired, because the nuclear frame needs time to rearrange.

The ideal experiment to measure nuclear dynamics is a Coulomb-explosion imaging measurement with a pump pulse and a probe pulse. This is visualized in figure 4.3

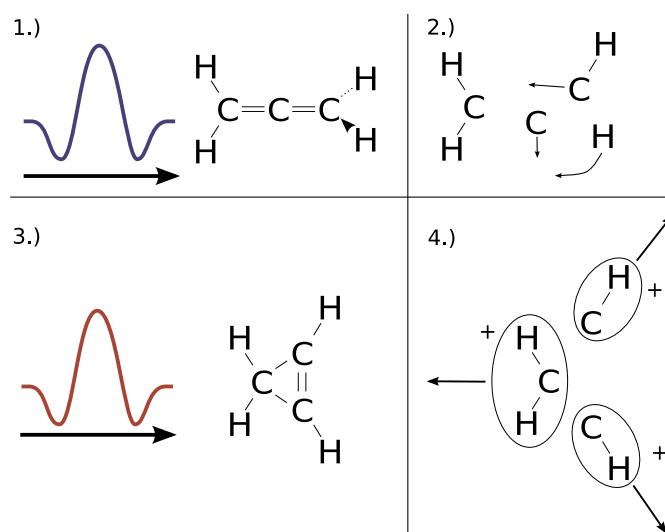


Figure 4.3.: Schematics of a four step pump–probe Coulomb-explosion imaging measurement. First the target molecule (in this case allene) is excited by the pump pulse (blue). The nuclei rearrange in step two. An isomer (in this case cyclopropene) has formed and is probed a second pulse (red) in the third step. A Coulomb-explosion is triggered. The geometry of the isomer can be reconstructed from the fragments' momenta (last step).

and explained below in four steps:

1. An ultrashort laser pulse, the so called pump pulse, excites (or ionizes) the target molecule.
2. As described in section 4.1.2, the nuclear frame starts to move in the direction of the local minimum of the new PES. An isomerization process triggered by the pump pulse has begun.
3. After a variable delay, a second ultra short pulse – the probe pulse – interrupts the isomerization by instantaneously exciting the molecule to a repulsive PES. The probe process must fulfill all requirements on Coulomb-explosion imaging listed in the previous section.
4. The momentum distribution of all fragments is measured and can be mapped to a molecular geometry at the time of interaction with the probe pulse.

In this ideal experiment, molecular geometries are imaged at different temporal delays between the pump and the probe pulse. The evolution of the molecular frame is then measured with a temporal precision that is given by the laser pulse length and the stability of the delay. While the concept of pump–probe Coulomb-explosion imaging is very simple, practical issues, most importantly high ionization thresholds

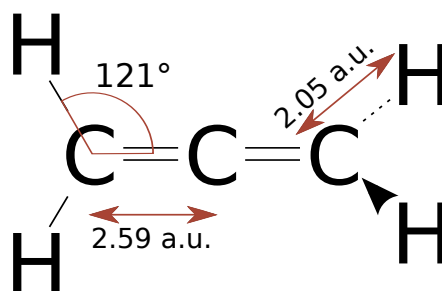


Figure 4.4.: Neutral ground state of allene. Bond lengths and angles from [PTS10].

for triply charged molecular ions and a low cross section for multi-ionization with a single photon, pose severe difficulties. These will be addressed in section 5.4 where the idea of pump-probe Coulomb-explosion imaging is applied to allene molecules. These molecules are introduced in the next section.

4.2. Allene

Hydrocarbons having two double bonds from a carbon atom to two others are called *allenes*. The simplest member of the allene group, propadiene (C_3H_4 , figure 4.4), is commonly known as allene [MST95]. Following previous scientific publications [Cor95, MBo8, XOY09a, XOY09b, PTS10], the name allene is used in this work as well. The geometry of the allene ground state is depicted in figure 4.4.

At room temperature and standard pressure, allene is a colorless gas with a molecular weight of 40.06 g/mol. It boils at $-34^\circ C$ and its melting point is at $-136^\circ C$ (at standard pressure) [Air]. Allene is a non-planar molecule, both CH_2 compounds are rotated by 90° with respect to each other (indicated by the dashed line and triangular shape of two CH bonds in figure 4.4). The symbol [a. u.] denotes that bond lengths are given in atomic units. Conversion factors to SI units are given in appendix A. Predicted isomers and fragmentation channels of allene dications are described in the next section.

4.2.1. Computed allene geometries and fragmentation pathways

The previously explained isomerization and PES concepts are now applied to a specific molecule, allene. Extensive quantum mechanical calculations on allene cations and fragmentation pathways were performed by A. M. MEBEL AND A.D. BANDRAUK, *Theoretical study of unimolecular decomposition of allene cations* [MBo8] on which large parts of this section depend.

Throughout the following sections, the terms *fragmentation channel* and *fragmentation path(way)* are used extensively. Following previous nomenclature [ZRX⁺12], each set of final fragments forms a fragmentation channel. Here, fragments are defined by their

molecular formula and not by their structural formula. In other words, if two isomers of a certain fragment exist, they are considered the same fragment.

One or more fragmentation pathways (also called fragmentation paths) are assigned to each channel. An example of two fragmentation paths corresponding to the same channel are two isomers of a molecular ion that can explode into identical final fragments.

Distinguishing between different fragmentation channels is in general simple with a ReMi because particle species of coincidences can be identified easily. To separate different fragmentation pathways of the same channel, detailed knowledge of the reaction dynamics is required. If observables like KER or angular distributions are not too different, it can be impossible to distinguish between such fragmentation paths.

Energy levels of allene dications and of fragmentations products calculated by A. M. MEBEL AND A.D. BANDRAUK [MBo8] are depicted as horizontal lines in figure 4.5. All energies are given in eV with respect to the singlet ground state of doubly charged allene (labeled as $C_3H_4^{2+}$). Arcs in figure 4.5 represent pathways between different isomers as well as fragmentation pathways. Barrier heights of each fragmentation path are given in eV. The molecular states at the top of each arc are called transition states (geometries of these transition states are given in [MBo8]). Stable geometries of electronic singlet state are given on the left hand side of figure 4.5. The right hand side of figure 4.5 depicts geometries of the electronic triplet state. The adiabatic double ionization energy of allene is 25.84 eV while the vertical double ionization energy is 28.05 eV and therefore 2.21 eV above the dication ground state.

Singlet isomers

Isomers of the electronic singlet state and fragmentation pathways starting from these isomers are introduced below.

The geometry of the allene dication ground state is shown in detail in figure 4.6. While the bond lengths and bond angles differ only slightly from the neutral ground state, it features a planar symmetry. Two fragmentation paths starting from the $C_3H_4^{2+}$ geometry exist (red arcs in figure 4.5):

- $C_3H_4^{2+} \rightarrow C_2H_2^+ + CH_2^+$
- $C_3H_4^{2+} \rightarrow C_2H_3^+ + H^+$

The energetically lowest isomer the cyclopropene dication (labeled c- $C_3H_4^{2+}$ in figure 4.5) lies approximately 0.60 eV above the ground state dication. It features a triangular geometry shown in figure 4.7 and can decay via three different fragmentation pathways (blue arcs in figure 4.5):

- c- $C_3H_4^{2+} \rightarrow C_3H_3^+ + H^+$
- c- $C_3H_4^{2+} \rightarrow C_2H_3^+ + CH^+$

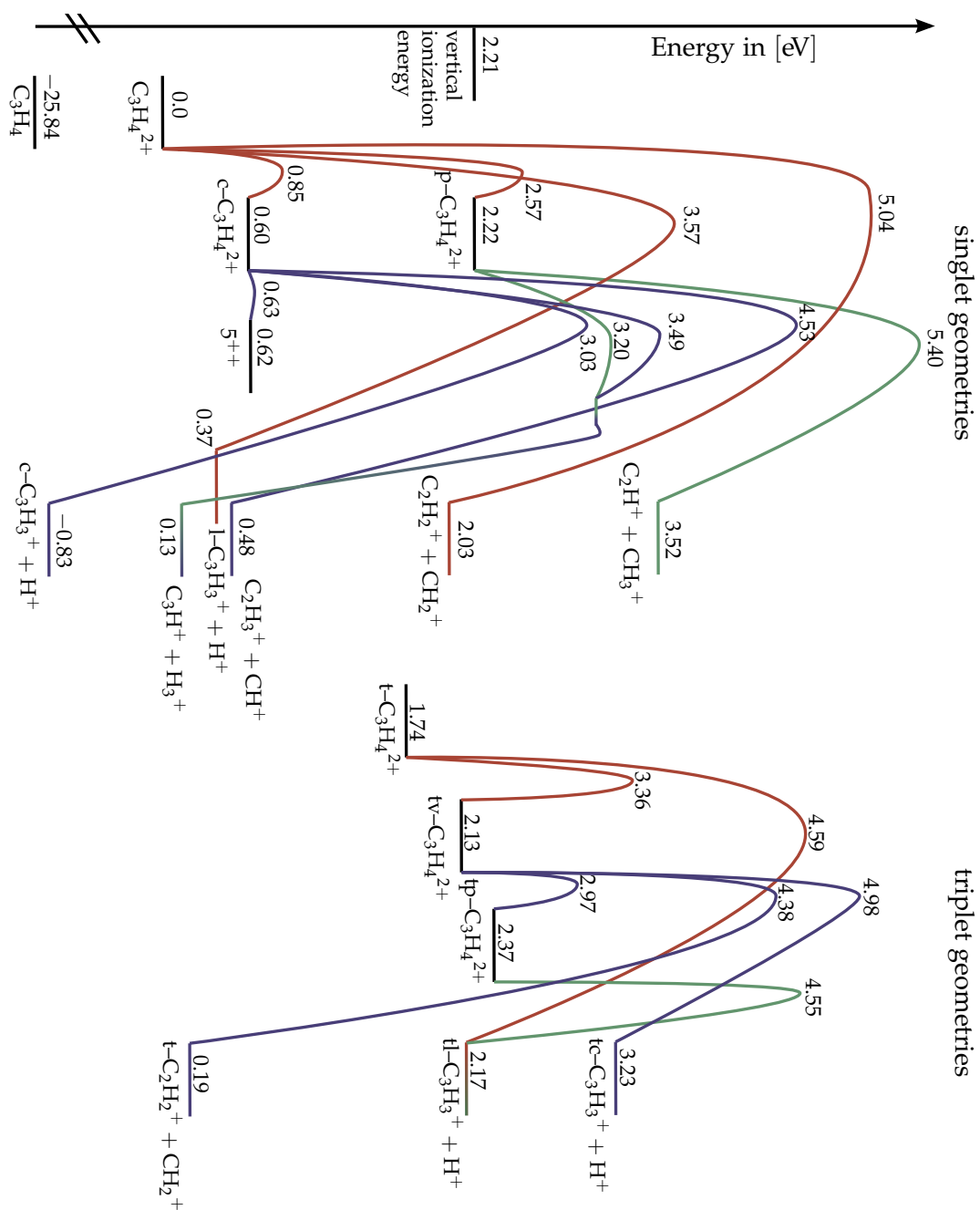


Figure 4.5.: Isomers, transition states and fragmentation pathways of doubly charged allene dications. Energy levels and pathways taken from [MBo8, Fig. 2].

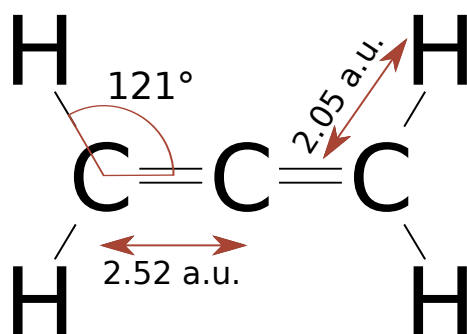


Figure 4.6.: Singlet ground state of $\text{C}_3\text{H}_4^{2+}$ dication. Bond lengths and angles from [PTS10].

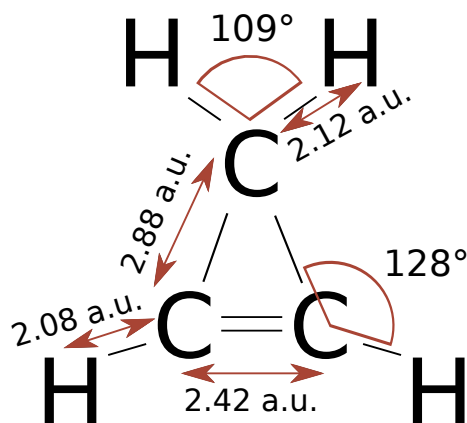
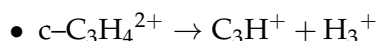
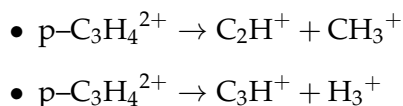


Figure 4.7.: Doubly charged cyclopropene ($\text{c-C}_3\text{H}_4^{2+}$). Bond lengths and angles from [PTS10].



Cyclopropene is separated by an extremely low barrier from another isomer, labeled 5^{++} in figure 4.5. An oscillation mechanism between those two isomers has been proposed by A. M. MEBEL AND A.D. BANDRAUK [MB08].

Doubly charged propyne (labeled $\text{p-C}_3\text{H}_4^{2+}$ in figure 4.5) lies approximately 2.22 eV above the singlet ground state. Three hydrogen atoms of the propyne dication are grouped around one of the outer carbon atoms in an interesting way (compare figure 4.8): a pair of the C-H bonds is elongated to 2.39 a. u. while the distance between those two hydrogen atoms is only 1.79 a. u. An H_2 molecule starts to separate [MB08]. $\text{p-C}_3\text{H}_4^{2+}$ can fragment via two different pathways (green arcs in figure 4.5):



Triplet isomers

Besides the singlet configurations, several triplet geometries exist. They are labeled with a prefix "t" in figure 4.5.

The triplet ground state (labeled $\text{t-C}_3\text{H}_4^{2+}$ in figure 4.5) lies 1.74 eV above the singlet ground state. It features a non-planar geometry similar to the neutral allene ground state, but with slightly different bond lengths [PTS10]. Two stable isomers of the triplet state exist, a propyne dication (labeled $\text{tp-C}_3\text{H}_4^{2+}$ in figure 4.5) and a doubly charged vinylmethylene (labeled $\text{tv-C}_3\text{H}_4^{2+}$ in figure 4.5). Fragmentation pathways starting from the triplet ground state are marked red in figure 4.5. Those starting from the

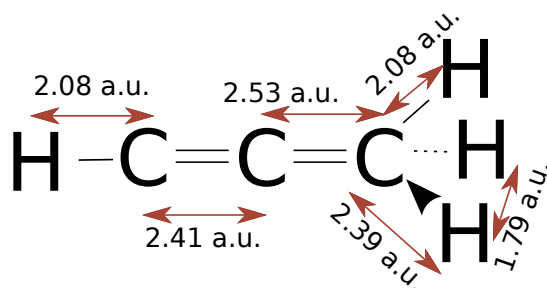


Figure 4.8.: Doubly charged propyne ($p\text{-C}_3\text{H}_4^{2+}$). Bond lengths and angles from [PTS10].

triplet propyne are marked green and paths starting from vinylmethylene are marked blue. The interested reader is referred to BRIAN T. PSCIUK ET AL. [PTS10] for details about triplet geometries.

In total, four different fragmentation paths start from the three stable triplet isomers:

- $t\text{-C}_3\text{H}_4^{2+} \rightarrow \text{C}_3\text{H}_3^+ + \text{H}^+$
- $tp\text{-C}_3\text{H}_4^{2+} \rightarrow \text{C}_3\text{H}_3^+ + \text{H}^+$
- $tv\text{-C}_3\text{H}_4^{2+} \rightarrow \text{C}_2\text{H}_3^+ + \text{H}^+$
- $tv\text{-C}_3\text{H}_4^{2+} \rightarrow \text{C}_2\text{H}_2^+ + \text{CH}_2^+$

Summarizing, six different fragmentation channels of doubly charged allene are predicted by theory:

1. $\text{C}_3\text{H}_4^{2+} \rightarrow \text{C}_2\text{H}_2^+ + \text{CH}_2^+$ (2)
2. $\text{C}_3\text{H}_4^{2+} \rightarrow \text{C}_2\text{H}_3^+ + \text{CH}^+$ (1)
3. $\text{C}_3\text{H}_4^{2+} \rightarrow \text{C}_2\text{H}^+ + \text{CH}_3^+$ (1)
4. $\text{C}_3\text{H}_4^{2+} \rightarrow \text{C}_3\text{H}_3^+ + \text{H}^+$ (5)
5. $\text{C}_3\text{H}_4^{2+} \rightarrow \text{C}_3\text{H}^+ + \text{H}_3^+$ (2)

The number of calculated fragmentation pathways per channel is given in brackets. Eleven different paths were found in total. A. M. MEBEL AND A.D. BANDRAUK searched intensively for the $\text{C}_3\text{H}_4^{2+} \rightarrow \text{C}_3\text{H}_2^+ + \text{H}_2^+$ channel because it was measured in previous experiments [XOY09b] but were not able to find a corresponding pathway [MBo8].

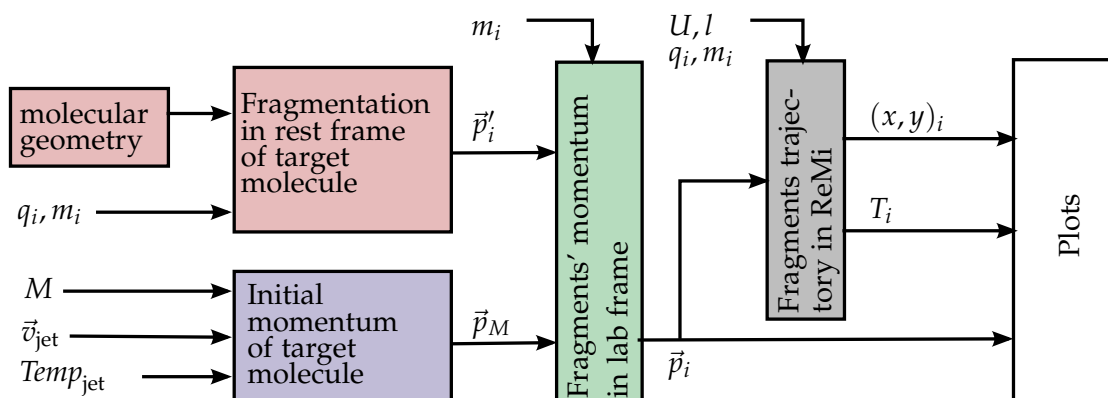


Figure 4.9.: Flowchart for the instantaneous fragmentation algorithm. Simulated spectra are created via several steps from various input parameters like fragments mass m_i and charge q_i as well as ReMi parameters like acceleration voltage U and acceleration length l . Different fragmentation processes can be simulated for different initial geometries.

In a different set of quantum mechanical *ab initio* calculations, the same fragmentation channels were found, albeit with different fragmentation pathways. Additionally, the fragmentation via the $C_3H^+ + H_3^+$ channel appears only if neutral propyne is doubly ionized [PTS10].

4.3. Software for simulation of ion trajectories in reaction microscopes

The simulation of molecular fragmentation processes can be used to visualize expected coincidence channels before starting an experiment. Simulated ToF spectra can be compared with obtained ToF spectra during the runtime of an experiment. This allows to judge the physical value of a measurement immediately and experimental parameters like laser pulses or spectrometer configuration can be adapted if necessary. Two types of simulations were developed. The first one is used to simulate instantaneous fragmentations. It is described in the next section. The second one is used to simulate Coulomb-explosions starting from metastable molecular ions. It is briefly introduced thereafter (in section 4.3.2).

4.3.1. Algorithm for the instantaneous fragmentation simulation

The simulation of instantaneous fragmentations can be described by five major steps listed below. In addition they are visualized by different colored boxes in the flow chart in figure 4.9. Detailed information on each step is given in the following paragraphs.

1. Blue box: The initial momentum \vec{p}_M of a target molecule with mass M is calculated in the laboratory frame from the jet temperature $Temp_{jet}$ and jet velocity \vec{v}_{jet} .
2. Red boxes: In the rest frame of the target molecule three different types of processes can be simulated: recoil ions from photo ionization, two body Coulomb-explosions and three body Coulomb-explosions. The initial momenta \vec{p}'_i of the created fragments with mass m_i and charge q_i are calculated in this step.
3. Green box: The fragments' initial momenta \vec{p}'_i are transformed into the laboratory frame. The momenta in the new coordinate system are denoted by \vec{p}_i .
4. Grey box: Time-of-flight T_i and hit positions $(x, y)_i$ are calculated in the laboratory frame from the fragments' initial momenta \vec{p}_i and from ReMi parameters like acceleration length l and acceleration voltage U .
5. White box: Different types spectra are created from T_i , $(x, y)_i$ and \vec{p}_i . Some of them are presented in section 4.4. This step is not described below.

1. Initial momentum of target molecule

Molecules within supersonic target gas jets are fast enough to cause measurable deviations in the hit positions. In the simulation, this macroscopic velocity \vec{v}_{jet} is taken into account by calculating a corresponding momentum $\vec{p}_{jet} = M\vec{v}_{jet}$. Here M denotes the mass of the target ion. The jet temperature $Temp_{jet}$ is considered isotropic. The momentum distribution of the target molecules is described by a Maxwell-Boltzmann distribution which is used to assign a randomized momentum \vec{p}_{Temp} to each simulated target particle. The total momentum of the target molecule in the laboratory frame is calculated with $\vec{p}_M = \vec{p}_{jet} + \vec{p}_{Temp}$.

2. Fragmentation in rest frame of target molecule

Three different physical processes are simulated in the rest frame of the target molecules. Only one "fragment" is created in recoil ion events. Therefore only one momentum \vec{p}'_i is calculated. In two body Coulomb-explosions, two momenta are calculated, one for each fragment. The third processes are three body Coulomb-explosions resulting in three final fragments with momenta \vec{p}'_i , $i \in \{1, 2, 3\}$. Below, the calculation of the momenta \vec{p}'_i is described for each type of fragmentation.

Recoil ions If a neutral atom or molecule with ionization potential E_i is photo-ionized by a photon of energy $E_{hv} > E_i$, an electron with kinetic energy $E_e = E_{hv} - E_i$ will be freed. The photon's momentum $|\vec{p}_{hv}| = E_{hv}/c$ can be neglected, if the inelastic energy transfer is small compared to the kinetic energy of the ejected electron [UMD⁺03,

p. 1269, 1270]. In this approximation, the ion's momentum \vec{p}'_i equals $-\vec{p}_e$ with $|\vec{p}_e| = \sqrt{2m_e E_e}$.

In the simulation software, the magnitude of $|\vec{p}'_i|$ is chosen as an input parameter and a randomized angular distribution of \vec{p}'_i is simulated with a β -parameter (section 3.3 and figure 3.3).

Two body Coulomb-explosions Multiple ionization of molecules can cause a Coulomb-explosion into two or more charged fragments as described in section 4.1.3. Typical momenta, caused by the Coulomb repulsion, are in the order of 20 to 100 a. u. which is one or two orders of magnitude larger than the momenta of photo electrons. This justifies neglecting the recoil momentum in the simulation of Coulomb-explosions.

Repulsing PESs are approximated by a Coulomb potential and the exploding fragments are considered as point-like in the software. The classical equations of motion, describing the trajectories of two charged particles in the external homogeneous electric field \vec{E} of a ReMi, are given by

$$\vec{F}_1(\vec{r}_1, \vec{r}_2, t) = q_1 \left(\vec{E} + \frac{1}{4\pi\epsilon_0} \frac{q_2}{|\vec{r}_{12}(t)|^3} \vec{r}_{12}(t) \right) = m_1 \ddot{\vec{r}}_1(t) \quad (4.9)$$

$$\vec{F}_2(\vec{r}_1, \vec{r}_2, t) = q_2 \left(\vec{E} + \frac{1}{4\pi\epsilon_0} \frac{q_1}{|\vec{r}_{21}(t)|^3} \vec{r}_{21}(t) \right) = m_2 \ddot{\vec{r}}_2(t) \quad (4.10)$$

with the distance vector $\vec{r}_{12} = \vec{r}_1 - \vec{r}_2 = -\vec{r}_{21}$ and charges $q_{1,2}$ and masses $m_{1,2}$ of the fragments. At typical initial distances of a few Ångström, the Coulomb field (second term in equations 4.9 and 4.10) is many orders of magnitude larger than the electric field $|\vec{E}| = U/l$ within a ReMi with acceleration voltage U and acceleration length l . As a result the Coulomb-explosion can be treated independent of the electric field. With this simplification, in the center of mass system, both fragments are ejected back to back due to momentum conservation. The momenta \vec{p}'_1 and \vec{p}'_2 imparted on both ions with initial distance vector \vec{r}_0 are calculated by

$$\vec{p}'_1 = -\vec{p}'_2 = \sqrt{\frac{q_1 q_2}{\frac{|\vec{r}_0|}{2} \left(\frac{1}{m_1} + \frac{1}{m_2} \right)}} \frac{\vec{r}_0}{|\vec{r}_0|}. \quad (4.11)$$

Molecular bond lengths have never exact values due to their description by quantum mechanical wave functions. In the simulation, this is taken into account by using a Gaussian distribution to randomize $|\vec{r}_0|$. The mean value and the variance of this distribution are set by parameters, while the angular distribution of \vec{r}_0 is described by a β -parameter (compare section 3.3 and figure 3.3).

Three body Coulomb-explosions The PESs of at least triply charged molecular ions can lead to a three body Coulomb-explosion with three charged final fragments. Typical

KERs are even higher than those of two body fragmentations, therefore the recoil momentum due to the photo electron is neglected as well.

The equations of motion describing three charged fragments in an external field \vec{E} are given by:

$$\vec{F}_1(\vec{r}_1, \vec{r}_2, \vec{r}_3, t) = q_1 \left(\vec{E} + \frac{1}{4\pi\epsilon_0} \left(\frac{q_2}{|\vec{r}_{12}(t)|^3} \vec{r}_{12}(t) + \frac{q_3}{|\vec{r}_{13}(t)|^3} \vec{r}_{13}(t) \right) \right) = m_1 \ddot{\vec{r}}_1(t), \quad (4.12)$$

$$\vec{F}_2(\vec{r}_1, \vec{r}_2, \vec{r}_3, t) = q_2 \left(\vec{E} + \frac{1}{4\pi\epsilon_0} \left(\frac{q_1}{|\vec{r}_{21}(t)|^3} \vec{r}_{21}(t) + \frac{q_3}{|\vec{r}_{23}(t)|^3} \vec{r}_{23}(t) \right) \right) = m_2 \ddot{\vec{r}}_2(t), \quad (4.13)$$

$$\vec{F}_3(\vec{r}_1, \vec{r}_2, \vec{r}_3, t) = q_3 \left(\vec{E} + \frac{1}{4\pi\epsilon_0} \left(\frac{q_1}{|\vec{r}_{31}(t)|^3} \vec{r}_{31}(t) + \frac{q_2}{|\vec{r}_{32}(t)|^3} \vec{r}_{32}(t) \right) \right) = m_3 \ddot{\vec{r}}_3(t), \quad (4.14)$$

Here $\vec{r}_{ij} = \vec{r}_i - \vec{r}_j = -\vec{r}_{ji}$ with $i, j \in \{1, 2, 3\}$, $i \neq j$ are the distance vectors between pairs of the point-like fragments with charges q_i and masses m_i . This system of coupled second order differential equations describes a classical three body problem which can not be solved analytically. For numerical integration, these nine second order differential equations are rewritten into eighteen first order differential equations by introducing

$$\vec{v}_1(t) = \dot{\vec{r}}_1(t) \Rightarrow \ddot{\vec{r}}_1(t) = \dot{\vec{v}}_1(t), \quad (4.15)$$

$$\vec{v}_2(t) = \dot{\vec{r}}_2(t) \Rightarrow \ddot{\vec{r}}_2(t) = \dot{\vec{v}}_2(t), \quad (4.16)$$

$$\vec{v}_3(t) = \dot{\vec{r}}_3(t) \Rightarrow \ddot{\vec{r}}_3(t) = \dot{\vec{v}}_3(t). \quad (4.17)$$

A Runge-Kutta integrator taken from the Gnu Scientific Library [GDT⁺09] is used to integrate this system of differential equations until the potential energy E_p of the system is much smaller than the sum kinetic energy $E_{\text{kin}}^{\text{sum}}$ of the three fragments. As soon as $E_p = \kappa E_{\text{kin}}^{\text{sum}}$ is fulfilled, the momentary momentum \vec{p}'_i of each particle is used to calculate the particle's ToF and hit position (compare flowchart in figure 4.9). It turned out that for a parameter $\kappa = 0.01$, the numerical error is well below the experimental resolution.

The initial distances between two pairs of particles $|\vec{r}_{12_0}|$ and $|\vec{r}_{13_0}|$, as well as the opening angle

$$\alpha = \frac{\vec{r}_{12_0} \cdot \vec{r}_{13_0}}{|\vec{r}_{12_0}| |\vec{r}_{13_0}|} \quad (4.18)$$

between those two bonds, are input parameters to define the initial molecular geometry. To take non-fixed bond lengths of real molecules into account, the initial position of each fragment can be randomized with a Gaussian distribution of a desired variance.

3. Transformation into the laboratory frame

The fragments' momenta \vec{p}'_i are calculated in the rest frame of the target molecule while the momentum \vec{p}_M is calculated in the laboratory frame. The transformation into the

laboratory frame for each fragment is given by

$$\vec{p}_i = \vec{p}'_i + \vec{p}_M \frac{m_i}{M}. \quad (4.19)$$

The second term describes the momentum transfer from the target molecule to the fragment at the moment of its creation.

4. Trajectory calculation within the fields of the ReMi

With known momenta \vec{p}_i in the laboratory frame, the time-of-flight T_i and hit position $(x, y)_i$ are computed for each fragment with

$$T_i = m_i \left(\frac{2l}{p_{z_i} + \sqrt{p_{z_i}^2 + 2m_i q_i U}} \right), \quad (4.20)$$

$$\begin{pmatrix} x \\ y \end{pmatrix}_i = \begin{pmatrix} p_x \\ p_y \end{pmatrix}_i / (m_i T_i). \quad (4.21)$$

These equations are obtained by rearranging equations 3.2 and 3.3. The acceleration length l and acceleration voltage U are input parameters chosen to describe the simulated ReMi. The charges and masses of the simulated particles are given by q_i and m_i .

4.3.2. Algorithm for simulation of delayed Coulomb-explosions

In experiments performed as a part of this thesis, metastable parent ions have been observed (compare section 5.2.5). After creation, they travel as a doubly charged ion within the ReMi until they eventually explode in a normal two body Coulomb-explosion. Such events will be called delayed Coulomb-explosions throughout this thesis. They have been included in the simulation, for a better interpretation of the corresponding observations.

The software to simulate delayed Coulomb-explosions is based in large parts on the simulation of instantaneous fragmentations described before. Additional calculations are performed to account for the trajectory of the metastable dication within the ReMi. The main steps in the simulation of delayed Coulomb-explosions are visualized in a flowchart in figure 4.10 and are briefly described below.

- Blue box: The initial momentum \vec{p}'_M of the metastable dication in the laboratory frame is calculated from the temperature and velocity of the target jet.
- Yellow boxes: A randomized decay time τ of the metastable dication is calculated from an exponential distribution with a half-life that is defined by the user. The ToF T_M of the parent ion is calculated from \vec{p}'_M with equation 4.20. If $T_M \leq \tau$,

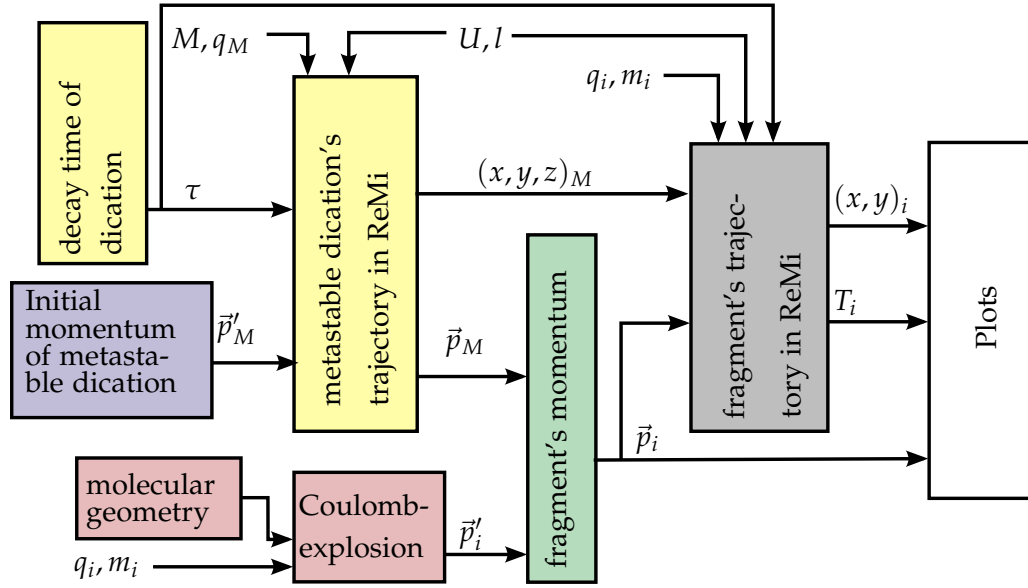


Figure 4.10.: Flowchart of delayed Coulomb-explosion simulation. First the trajectory of the metastable dication is calculated until its explosion at time τ . The fragments' trajectories are then simulated for the remaining distance to the detector.

the parent ion's ToF and hit position will be registered similar to a recoil ion described above. If $T_M > \tau$, the trajectory of the dication within the ReMi will be calculated until the moment of fragmentation at time τ . The gained momentum \vec{p}_M and its position $(x, y, z)_M$ at that time are used for further calculations below.

- Red boxes: A two body Coulomb-explosion in the rest frame of the parent ion is simulated as described before.
- Green box: As for the instantaneous fragmentation, the fragments' initial momenta \vec{p}_i in the laboratory frame are calculated from \vec{p}_M and \vec{p}'_i .
- Grey box: The dication's position $(x, y, z)_M$ at time τ and the momenta \vec{p}_i are used to calculate the remaining times-of-flight T'_i and the hit positions $(x, y)_i$ of the fragments. The used formulas deviate slightly from equations 4.20 and 4.21 to take into account the reduced spectrometer length and the reduced electric potential due to the distance that has been traveled by the metastable dication. The total time-of-flight T_i is calculated from $T_i = \tau + T'_i$.
- White box: Different types of spectra are created with the fragments' times-of-flight T_i , hit positions $(x, y)_i$ and momenta \vec{p}_i .

4.4. Simulated allene fragmentation spectra

In section 4.2.1 six predicted allene fragmentation channels were introduced. The simulation described in the previous section provides a powerful tool to visualize and familiarize oneself with those fragmentation channels and with expected ToF spectra of allene. After a brief introduction to (*double-ion*) ToF correlation spectra and (*triple-ion*) ToF correlation spectra, simulated spectra are presented.

All spectra presented in this section were simulated with an acceleration voltage $U = 400$ V, an acceleration length $l = 16.1$ cm and a target jet temperature $T = 1$ K. These values resemble the ReMi settings used for acquisition of the experimental data in chapter 5.

4.4.1. Introduction to time-of-flight correlation spectra

ToF correlation spectra are used throughout this work for identification of coincidence channels. (Double-ion) ToF correlation spectra incorporate the time-of-flight of two fragments. Three body fragmentations are best identified with triple-ion ToF correlation spectra. Both types of spectra are described below. For convenience, double-ion ToF correlation spectra will be called ToF correlation spectra in this thesis, if ambiguity with triple-ion ToF correlation spectra can be excluded.

(Double-ion) ToF correlation spectra

In a two body Coulomb-explosion, momentum conservation dictates

$$\vec{p}_1 = -\vec{p}_2 \quad (4.22)$$

for momenta \vec{p}_1 and \vec{p}_2 of the involved fragments. Plotting p_{z_1} vs. p_{z_2} will result in diagonal lines, because the fragments' momenta are correlated by equation 4.22. Horizontal or vertical lines would mean p_{z_1} is independent of p_{z_2} which violates momentum conservation. Such line will appear in experimental spectra if so called false coincidences are created. This happens for instance if more than one target molecule is ionized by a single laser pulse.

Momentum correlation spectra cannot be used for identification of coincidence channels because the (initially) unknown charges and masses of the involved particles are required to calculate p_{z_1} and p_{z_2} from the measured ToFs. Instead so called (double-ion) ToF correlation spectra, where the time-of-flight T_1 of the first fragment is plotted vs. the time-of-flight T_2 of the second fragment, are used to identify coincidence channels. In such spectra, coincidences create curved diagonal lines, because the measured ToFs depend only on the p_z momentum components (compare equation 4.20). The curvature of these lines results from the nonlinear p_z dependency in equation 4.20. The smaller ToF is typically plotted on the ToF₁-axis and the larger ToF is plotted on the ToF₂-axis in ToF correlation spectra.

Triple-ion ToF correlation spectra

The normal double-ion ToF correlation spectrum of a three body Coulomb-explosion does not feature sharp diagonal lines, because the momentum conservation of a three body fragmentation

$$\vec{p}_1 = -(\vec{p}_2 + \vec{p}_3) \quad (4.23)$$

involves three momenta. By plotting ToFs of only two fragments, the momentum imparted on the third fragment is not taken into account.

This third ion is incorporated by plotting T_1 vs. $(T_2 + T_3)$ in a triple-ion ToF correlation spectrum. This correlates the ToF of one ion, with those of the other two. In this work, the three permutations of T_i vs. $(T_j + T_k)$ ($i \neq j \neq k$, $i, j, k \in \{1, 2, 3\}$) are plotted in the same spectrum. Furthermore the smaller value of T_i and $(T_j + T_k)$ is plotted on the ToF₁-axis and the larger value defines the ToF₂ + ToF₃-value. The coincidence lines in triple-ion ToF correlation spectra can contain small sub features due to the nonlinear dependency between the ToFs and momenta.

Triple-ion ToF correlation spectra are the method of choice for identification of three body coincidences. But plotting ToFs of three body coincidences in double-ion ToF correlation spectra can unveil important information on the geometry of the parent ion, as demonstrated in section 4.4.4.

4.4.2. Simulated recoil ion spectra

Most parts of the previous sections were focused on Coulomb-explosions, but single and double ionization of allene results in slow recoil ions which will be observed in an experiment as well. These are expected to produce several sharp peaks in the ToF spectra. In figure 4.11 simulated ToFs of three different molecular recoil ions are plotted.

ToF in [ns]	Species	mass in [u]	charge in [a. u.]
7275	C_3H_4^+	40	1
7366	$(^{13}\text{C})\text{C}_3\text{H}_4^+$	41	1
5144	$\text{C}_3\text{H}_4^{2+}$	40	2

Table 4.1.: Simulated ToFs of allene fragments.

The peaks in the ToF spectrum are summarized in table 4.1. The notation $(^{13}\text{C})\text{C}_3\text{H}_4^+$ denotes that one of the carbon atoms is replaced by a ^{13}C isotope. From equation 4.20 one expects, for a negligible momentum p_{z0} , the relation

$$\frac{T_j}{T_k} = \frac{\sqrt{q_k}}{\sqrt{q_j}} \frac{\sqrt{m_j}}{\sqrt{m_k}} \quad (4.24)$$

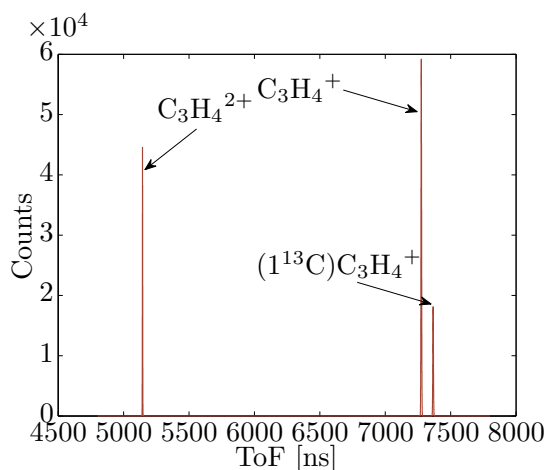


Figure 4.11.: Simulated ToF of allene molecular ions.

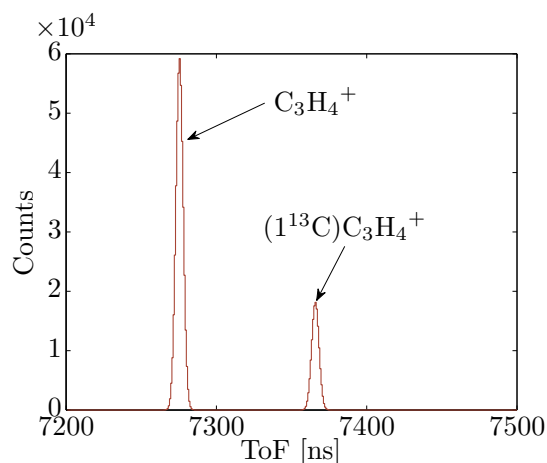


Figure 4.12.: Simulated ToF of allene isotopes.

for the ToFs $T_{j,k}$ of two ions j and k with masses $m_{j,k}$ and charges $q_{j,k}$ within the same spectrometer. As expected, the simulated ToFs are described by this relation as well.

4.4.3. Simulated two body Coulomb-explosion spectra

Simulated ToF correlation spectra of the six predicted allene fragmentation channels introduced in section 4.2.1 are presented here. The channels can be organized into two groups: the first group, in this work called C₂–C coincidences, features the final fragments $C_2H_i^+ + CH_{4-i}^+$ with $i \in \{1, 2, 3\}$. The final fragments $C_3H_i^+ + H_{4-i}^+$ with $i \in \{1, 2, 3\}$ are grouped in the C₃–H coincidences.

The two groups appear at very different positions in the ToF correlation spectrum, because of the rather small mass difference of the two fragments in the C₂–C group and the large mass differences of the C₃–H fragments. Simulated ToF correlation spectrum of both groups are discussed in the following paragraphs.

C₂–C coincidences

A ToF correlation spectrum of the C₂–C coincidences is plotted in figure 4.13. The three diagonal, slightly curved, lines of the three coincidence channels are clearly visible. All fragmentation channels are simulated with an initial internuclear distance of 5.5 a. u. This value is motivated by the bond lengths of the neutral allene ground state shown in figure 4.4. The bond lengths only affects the lengths of the lines in figure 4.13, the positions of the lines remain unchanged. The width of the lines is results from the simulated target temperature.

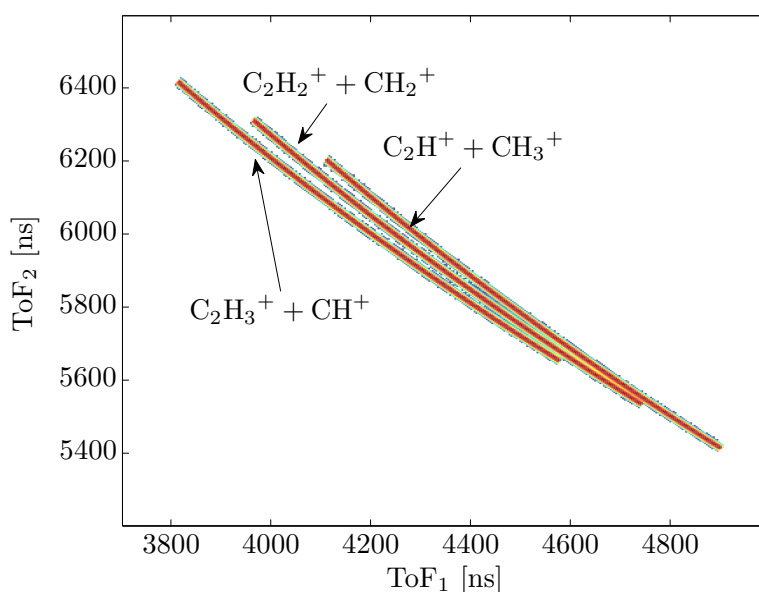


Figure 4.13.: Simulated two body Coulomb-explosions involving C_2 -C coincidences.

C_3 -H coincidences

Figure 4.14 shows a ToF correlation spectrum of the C_3 -H group. All three coincidences were simulated with the same initial internuclear distance of 6 a. u., a value which is taken from the analysis of the experimental data in section 5.2.3.

The elongated $C_3H_3^+ + H^+$ coincidence line results from simulated delayed Coulomb-explosions. The simulated half-life $T_{1/2} = 350$ ns of the metastable $C_3H_4^{2+}$ dication was chosen to resemble the length of the corresponding experimental line (plotted in figure 5.2) qualitatively.

The exact process leading to this line shape is shown in figure 4.15: the later the doubly charged, metastable parent ion explodes, the smaller is the measured time difference between the proton's time-of-flight T_1 and the time-of-flight T_2 of the $C_3H_3^+$ fragment. It is even possible, that the metastable dication does not decay at all before it hits the detector. In this case it is measured as a doubly charged allene ion.

The experimental ToF correlation spectrum in figure 5.2 shows indications of a delayed Coulomb-explosion for the $C_3H^+ + H_3^+$ as well. A very short simulated half life $T_{1/2} = 15$ ns resembles the experimental data qualitatively.

4.4.4. Simulated three body Coulomb-explosion spectra

Although three body Coulomb-explosions of triply charged allene molecular ions are not predicted by theory [MBo8], experimental evidence of triple ion coincidences exists [XOY09a]. In order to demonstrate the capabilities of the simulation, two channels

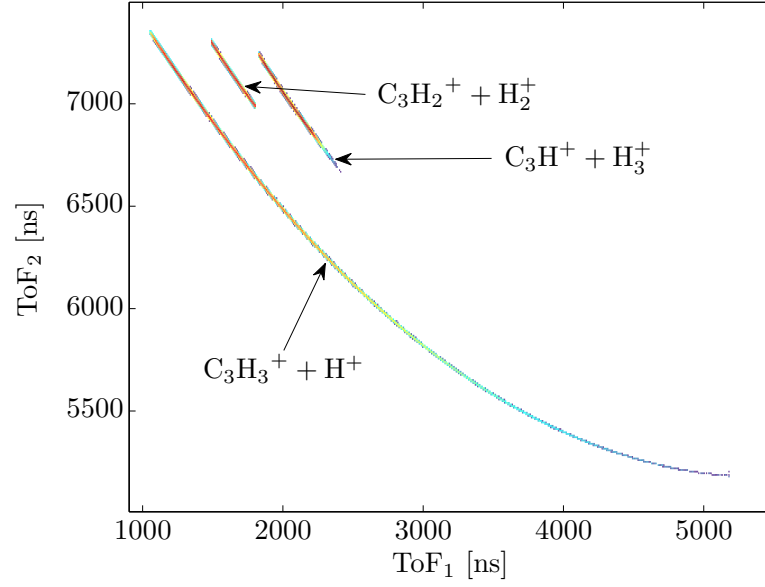


Figure 4.14.: Simulated two body Coulomb-explosions involving C_3 -H coincidences. The delayed Coulomb-explosion of the channel $C_3H_3^+ + H^+$ is simulated with a half-life of $T_{1/2} = 350$ ns. The $C_3H^+ + H_3^+$ channel is simulated with a half-life of $T_{1/2} = 15$ ns. A logarithmic color scale is used.

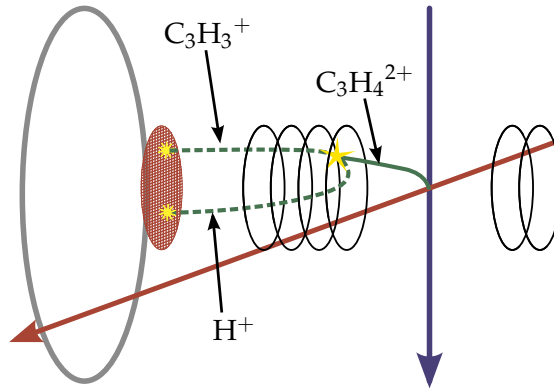


Figure 4.15.: Schematics of a delayed Coulomb-explosion within a ReMi.

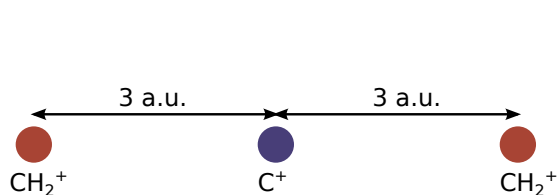


Figure 4.16.: The linear initial geometry of the first channel used in the simulation.

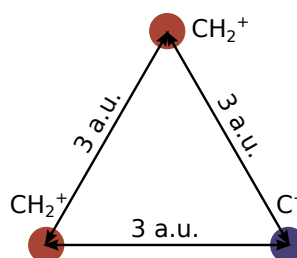
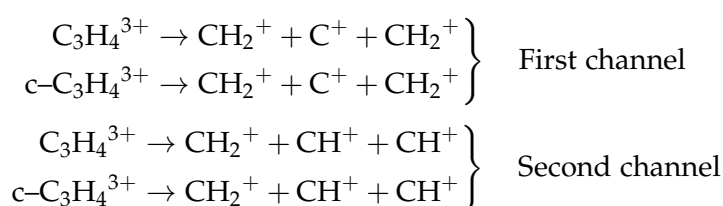


Figure 4.17.: The triangular initial geometry of the first channel used in the simulation.

with four different pathways were simulated:



The notation $\text{C}_3\text{H}_4^{3+}$ indicates a linear parent molecule. $\text{c-C}_3\text{H}_4^{3+}$ denotes a triangular initial geometry.

For each path, several million events were simulated. The molecules were randomly oriented in space with an isotropic angular distribution. The initial location of each fragment was randomized by a Gaussian distribution with a variance of 0.1 a. u. This takes varying bond lengths of real molecules into account. Double-ion ToF correlation spectra and triple-ion ToF correlation spectra of both channels are compared below.

First channel

The initial geometries of the first channel's fragmentation paths are shown in figures 4.16 and 4.17. The double-ion ToF correlation spectra (figures 4.18 and 4.19) of the two pathways show very different structures. Simulation of triangular geometries causes circular shapes to occur in the double-ion ToF correlation spectrum. Plotting of simulated events starting from of a linear geometry results in several straight lines.

The structure in figure 4.18 is explained by the symmetry of the simulated geometry. The central fragment ion gains very little momentum, because the terminal ions have equal masses and charges. As a result, the central ion has a very small spread of ToFs around 4000 ns while terminal fragments have a high ToF spread that depends on the initial orientation of the parent ion. The horizontal and vertical lines result from plotting the ToFs of the central ion vs. those of the terminal ions. The diagonal line is caused by the double-ion ToF correlation of the terminal ions, which are strongly correlated because the central ions carries very little momentum and momentum conservation is approximated by a two body momentum conservation.

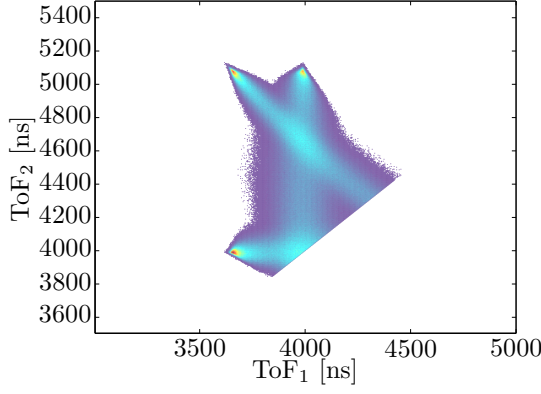


Figure 4.18.: Double-ion ToF correlation spectrum of the linear geometry (first channel).

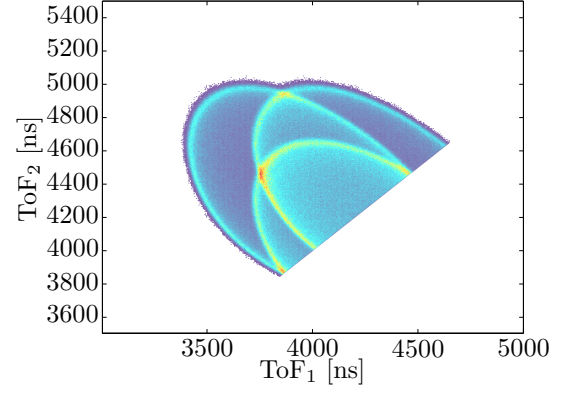


Figure 4.19.: Double-ion ToF correlation spectrum of the triangular geometry (first channel).

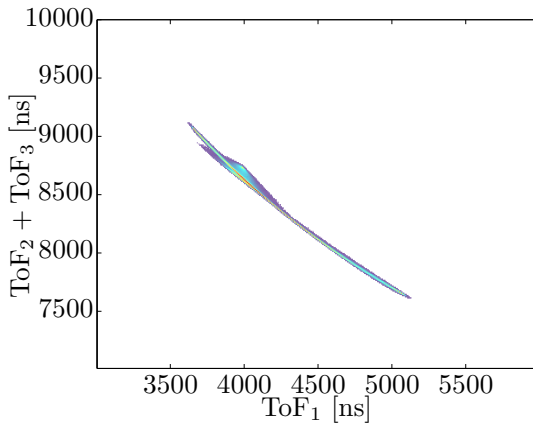


Figure 4.20.: Triple-ion ToF correlation spectrum of the linear geometry (first channel).

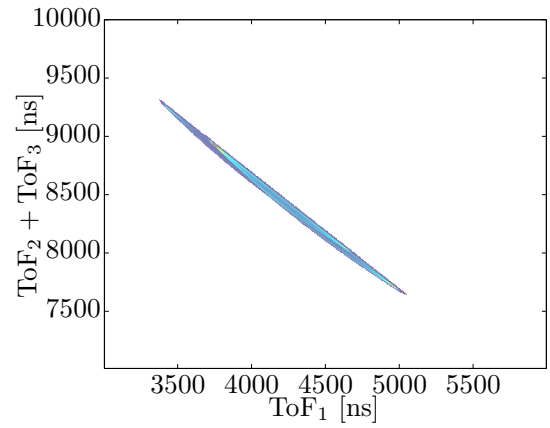


Figure 4.21.: Triple-ion ToF correlation spectrum of the triangular geometry (first channel).

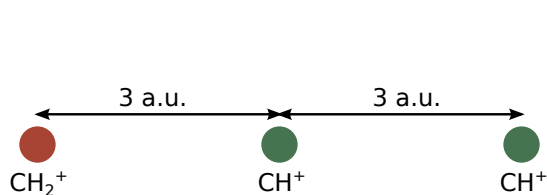


Figure 4.22.: The linear initial geometry of the second channel used in the simulation.

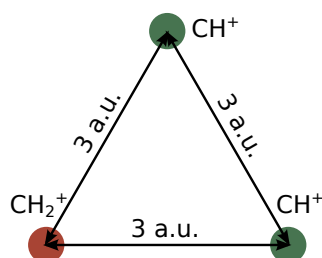


Figure 4.23.: The triangular initial geometry of the second channel used in the simulation.

The circles in the double-ion ToF correlation spectrum of the triangular molecule are difficult to explain in detail but the absence of straight lines can be understood. Due to the triangular symmetry, each of the fragments gains approximately the same kinetic energy which means that all momenta in the three body momentum conservation (equation 4.23) must be taken into account equally. Therefore the plotting of the ToF correlation between two fragments does not result in straight lines.

As expected from momentum conservation (compare equation 4.23), the triple-ion ToF correlation spectra (figures 4.20 and 4.21) feature a sharp diagonal line for both pathways. The substructures result from the nonlinear relation between ToF and p_z in equation 4.20.

Second channel

The two initial geometries of the second channel are shown in figures 4.22 and 4.23. The general features of their double-ion ToF correlation spectra (plotted in figures 4.24 and 4.25) can be explained by the same arguments as for the first channel. The more symmetric structure in figure 4.24 compared to figure 4.18 results from the smaller mass differences of the involved particles. For equal masses of all fragments, the three lines in the double-ion ToF correlation spectrum would intersect at the same point.

The triple-ion ToF correlation spectra of the linear and triangular geometry (figures 4.20 and 4.21) show again sharp diagonal lines. Similar to the pathways of the first channel, deviations in the substructure can be found.

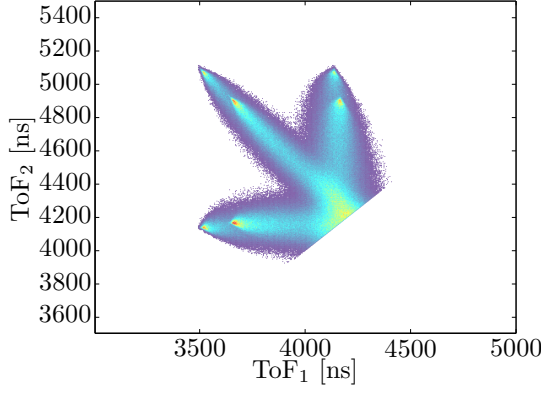


Figure 4.24.: Double-ion ToF correlation spectrum of the linear geometry (second channel).

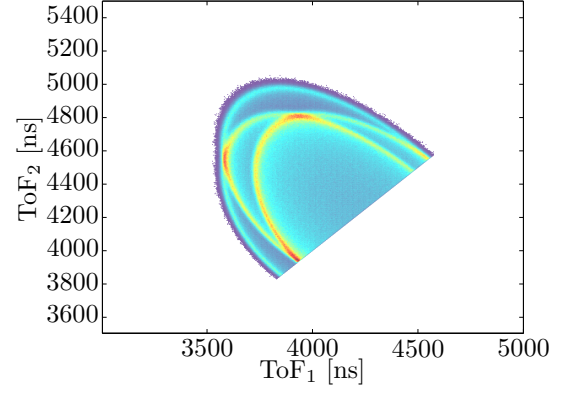


Figure 4.25.: Double-ion ToF correlation spectrum of the triangular geometry (second channel).

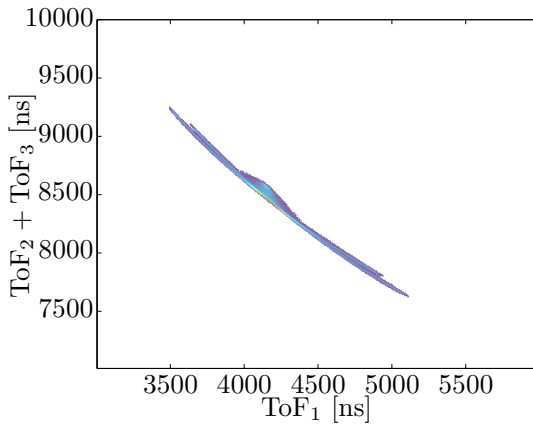


Figure 4.26.: Triple-ion ToF correlation spectrum of the linear geometry (second channel).

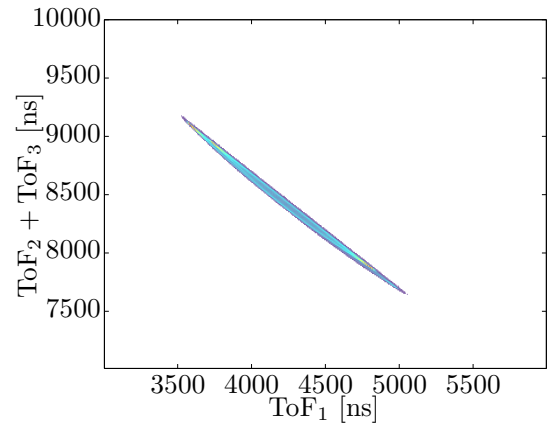


Figure 4.27.: Triple-ion ToF correlation spectrum of the triangular geometry (second channel).

5. Laser induced Coulomb-explosion of allene - Experimental results

Contents

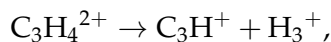
5.1. Previous experiments on allene molecules	49
5.2. Conducted IR single pulse experiments	50
5.3. Conducted XUV single pulse experiment	78
5.4. Conducted XUV-IR Pump-probe experiment	79

This chapter begins with a short introduction to comparable experiments performed by other groups (section 5.1). Afterwards three types of measurements conducted within the framework of this thesis are discussed. All experiments have been performed with pulses created by the lasersystem described in section 2.2. Charged products of fragmentation processes have been detected with a ReMi. Data obtained from a single pulse experiment with IR pulses at different pulse intensities and pulse lengths is analyzed in section 5.2. Results gathered by XUV induced allene fragmentations are presented in section 5.3. Finally outcomes of an XUV-IR pump-probe measurement are interpreted in section 5.4.

5.1. Previous experiments on allene molecules

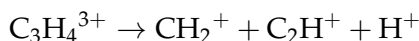
In 1995, C. CORNAGGIA [Cor95] performed Coulomb-explosion imaging experiments with highly intense, 130 fs Ti:sapphire laser pulses that ionized the allene molecules to extremely high charge states. The ionization process was described as follows: at the beginning of the laser pulse, stable $C_3H_4^+$ and $C_3H_3^+$ cations were produced. After several tenths of femtoseconds, at peak intensity, the molecular ions were further ionized to highly charged states. These exploded preferably into doubly and triply charged carbon fragments in a triple-ion Coulomb-explosion. ToF correlation spectra of those fragments indicated a linear carbon chain at the moment of fragmentation. It was concluded that $C_3H_4^+$ and $C_3H_3^+$ molecular ions feature a linear geometry similar to neutral allene molecules. These observations are in contradiction to more recent theoretical studies which predict isomerization in singly [MBo8] and doubly charged [MBo8,PTS10] allene molecular ions.

Experiments performed with 40 fs laser pulses in 2008 [XOY09b] revealed several double-ion coincidence channels. Some of those, e.g.

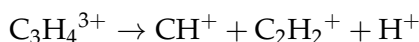


cannot start from the neutral allene geometry (shown in figure 4.4) because they require a hydrogen atom to migrate along the carbon chain. In the same experiment an anisotropic angular distribution of C₂–C explosions was found. It was concluded that C₂–C explosions occur shortly after ionization which is most probable for molecules aligned parallel to the laser polarization. The explosions of C₃–H channels, however, featured a more isotropic angular distribution. These fragmentations result from a metastable dication with a half-life of a few pico-seconds. Within this time the metastable dication can rotate freely. This results in an isotropic angular distribution.

Triple-ion fragmentations induced by intense 40 fs laser pulses were observed in 2009 [XOY09a]. The coincidence channels



and



feature relative angular distributions which indicate a proton migration along the entire carbon chain.

In order to verify these previous experimental results single pulse experiments have been conducted as a part of this thesis. Additionally a pump–probe measurement with allene target molecules has been performed for the first time to further improve our understanding of allene isomerization.

5.2. Conducted IR single pulse experiments

In a first measurement IR laser pulses of three different pulse intensities and two different pulse lengths were used to create singly and doubly charged allene ions by multi-photon ionization. Charged fragments of dissociations and Coulomb-explosions as well as stable allene cations and dications were detected with the MCP detectors of the ReMi.

A ToF spectrum and a ToF correlation spectrum acquired at medium pulse intensities are presented in the next two sections. These spectra are used to identify particle species and coincidence channels. KER spectra of Coulomb-explosion channels are given in section 5.2.3 and channel branching ratios for different pulse parameters are shown in section 5.2.4. Results in both sections are used to obtain information about the PESs of allene dications. Furthermore the data gathered in our experiments is compared with theoretical predictions and results from earlier experiments. Finally, in section 5.2.5, a Coulomb-explosion channel resulting from a metastable doubly charged allene molecular ion is discussed and the half-life of this ion is estimated.

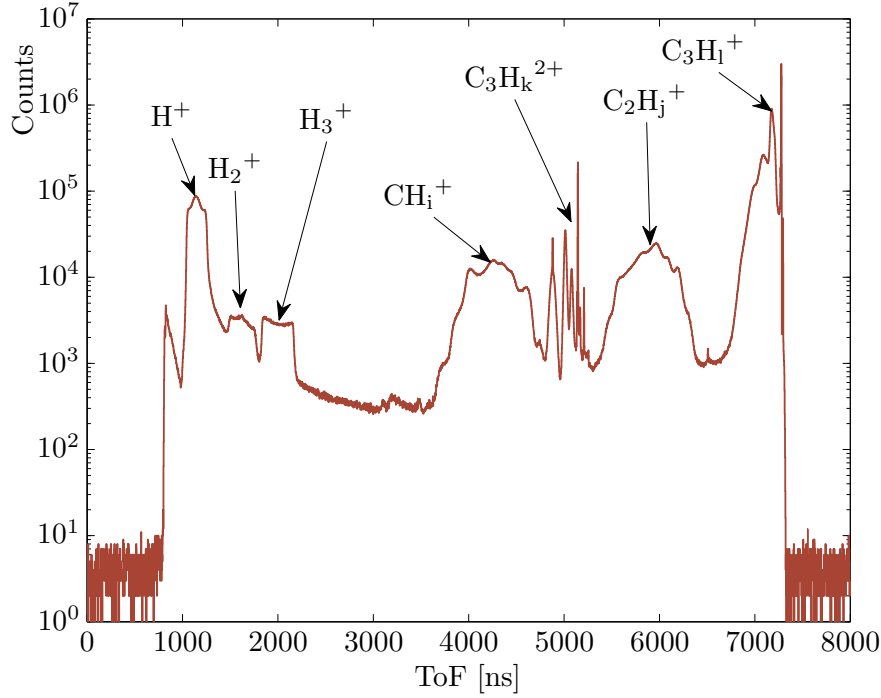


Figure 5.1.: Measured ToF spectrum of allene fragmentations induced by IR pulses of medium intensity. Identified allene fragments are labeled ($i, j \in \{1, 2, 3\}$; $k \in \{2, 3, 4\}$ and $l \in \{1, 2, 3, 4\}$). A logarithmic scale on the y -axis is used.

5.2.1. Time-of-flight spectrum and identification of fragments

A measured ToF spectrum of allene is shown in figure 5.1. This spectrum is used to identify created allene fragments.

The sharp cutoffs at 800 ns and 7300 ns result from the time to digital converter (TDC) window that only accepts ions within this time interval. The relation 4.24 and equation 4.20 (assumed that spectrometer parameters are known) allow an identification of the peaks in this spectrum. A simulation of a ToF spectrum with expected fragments can further help to identify peaks in the experimental spectrum. The ToF spectrum in figure 5.1 can be separated into five part. Peaks within each part are identified below.

ToFs between 6500 ns and 7300 ns The sharp peak at 7282 ns is identified as the $C_3H_4^+$ allene cation peak. The peaks and the shoulder at slightly smaller ToFs (7190 ns, 7100 ns and 7000 ns) result from singly charged allene with loss of one, two or three hydrogen atoms. The creation of one or multiple neutral hydrogen atoms with a non-zero momentum explains why these peaks are relatively broad compared to that of $C_3H_4^+$.

ToFs between 5500 ns and 6500 ns The broad structure between 5400 ns and 6350 ns is created by $C_2H_j^+$, $j \in \{1, 2, 3\}$ molecular ions. The broad ToF distribution is a sign for high KERs created by Coulomb-explosions.

ToFs between 4800 ns and 5500 ns The sharp peaks between 5000 ns and 5150 ns are identified as doubly charged allene fragments $C_3H_4^{2+}$, $C_3H_3^{2+}$ and $C_3H_2^{2+}$. The small peak at 5208 ns corresponds to $(^{13}C)C_3H_4^{2+}$. The peak at 4878 ns is created by the H_2O^+ from the residual gases within the ReMi. These molecules are hot compared to the jet temperature which results in a relatively broad peak.

ToFs between 3500 ns and 4800 ns The broad structure between 3600 ns and 4700 ns results from CH_i^+ , $i \in \{1, 2, 3\}$ molecular ions with different numbers of hydrogen atoms. Again the broad ToF distribution indicates fragments with high momenta resulting from Coulomb-explosions.

ToFs between 800 ns and 3500 ns H^+ , H_2^+ and H_3^+ create structures at ToFs between 1000 ns and 2500 ns. Their widths indicate high kinetic energies obtained in Coulomb-explosions.

5.2.2. Time-of-flight correlation spectra and identification of coincidences

While ToF spectra are useful for identification of created ion species, coincidence channels are identified best with the ToF correlation spectra in figure 5.2 and figure 5.4. These spectra will be analyzed in several steps that are listed below and explained in detail afterwards.

1. The origin of **horizontal and vertical lines** in figure 5.2 are explained by **false coincidences**.
2. **C_3 -H coincidences** shown in figure 5.2 are identified.
3. The elongated $C_3H_3^+ + H^+$ and $C_3H^+ + H_3^+$ coincidence lines are identified as **delayed Coulomb-explosions**.
4. **C_2 -C coincidences** shown in figure 5.4 are identified.
5. The identified coincidence channels are discussed and compared with predictions from theory and with results from experiments performed by other groups. It is discussed why Coulomb-explosions from triply charged parent molecules were not observed in our experiments.

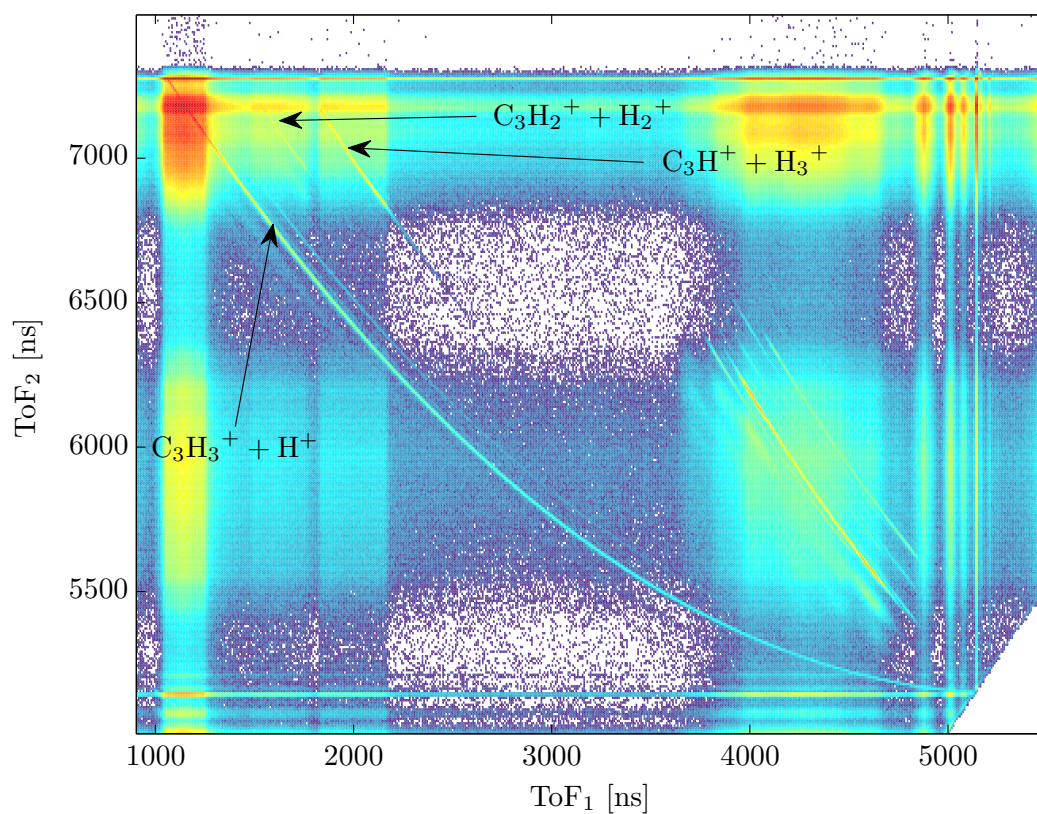


Figure 5.2.: Measured ToF correlation spectrum of allene. Identified diagonal lines created by C_3 -H double-ion coincidences are labeled. Horizontal and vertical lines are created by false coincidences. A logarithmic color scale is used.

1. Horizontal and vertical lines – false coincidences

In contrast to the simulated ToF correlation spectra (figure 4.14), the experimental spectrum in figure 5.2 shows horizontal and vertical lines. These result from the plotting of false coincidences whenever two uncorrelated ions are created by a single laser pulse. For instance the broad vertical line at a $\text{ToF}_1 = 1150 \text{ ns}$ is created by plotting protons ToFs in (false) coincidence with ToFs of heavy ions that are created by ionization of a *different* target molecule. In other words, horizontal or vertical lines indicate that the measured ToF of one ion is independent of the second ion's ToF. If these ions had been created in the same (two body) Coulomb-explosion, momentum conservation would have been violated (compare section 4.4.1).

2. C₃-H coincidences

Diagonal lines in figure 5.2 are only created by plotting real coincidences. These lines can be assigned to fragmentation channels by comparing their values of ToF_1 and ToF_2 with the identified peaks in figure 5.1. The assignment of lines is further simplified by comparing the measured ToF correlation spectrum with the simulated one in figure 4.14.

The coincidence lines beginning at small ToF_1 and large ToF_2 are assigned to C₃-H coincidences (labeled in figure 5.1). The coincidence lines in the bottom right corner of figure 5.1 are created by C₂-C coincidences and will be discussed later.

Several lines parallel to the $\text{C}_3\text{H}_3^+ + \text{H}^+$ coincidence are found. The right shifted line results from a $(^{13}\text{C})\text{C}_3\text{H}_3^+ + \text{H}^+$ coincidence with a ^{13}C isotope in the allene fragment. The broad line shifted to the left results from $\text{C}_3\text{H}_2^+ + \text{H}^+ + \text{H}$ coincidences. The momentum imparted on the undetected neutral H atom broadens this line. Even further left is a faint line produced by coincidences with loss of two neutral hydrogen atoms.

Two coincidence lines are assigned to the $\text{C}_3\text{H}_2^+ + \text{H}_2^+$ and the $\text{C}_3\text{H}^+ + \text{H}_3^+$ fragmentation channels. The coincidence line of the latter is more prominent. This is interesting because the creation of a H_3^+ ion requires a proton migration while the production of H_2^+ ions is more intuitive from the geometry of neutral allene (shown in figure 4.4).

3. Delayed Coulomb-explosions

The extremely elongated $\text{C}_3\text{H}_3^+ + \text{H}^+$ coincidence line could be explained by two different processes: either the fragments have extremely high energies or the doubly charged parent ion is metastable and travels towards the detector until it eventually explodes.

Simulated coincidences of both processes are plotted in figure 5.3. Their curvature and their probability distribution are compared with the measured line in figure 5.2.

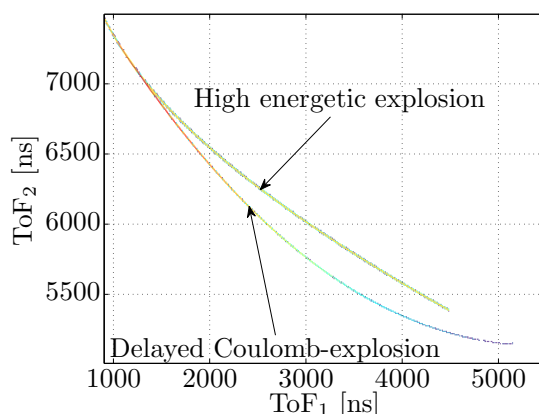


Figure 5.3.: Simulation of two types of Coulomb-explosion. Highly energetic Coulomb-explosions with an initial internuclear distance of only 0.02 a. u. and delayed Coulomb-explosions with an initial distance of 7 a. u. and 350 ns half-life of the metastable parent ion.

It is concluded from the line shape that the $\text{C}_3\text{H}_3^+ + \text{H}^+$ coincidences result, at least partly, from metastable dications.

The elongated $\text{C}_3\text{H}^+ + \text{H}_3^+$ coincidence line in figure 5.2 might indicate another delayed Coulomb-explosion with a short half-life. A simulation of this coincidence with 15 ns half-life is plotted in figure 4.14.

4. C_2 –C coincidences

The diagonal lines in the bottom right corner of figure 5.2 are created by plotting C_2 –C coincidences. This region is magnified in figure 5.4. The prominent red line is assigned to the $\text{C}_2\text{H}_2^+ + \text{CH}_2^+$ coincidence, while the orange line shifted to the left results from the $\text{C}_2\text{H}_3^+ + \text{CH}^+$ channel. The probability for a fragmentation into $\text{C}_2\text{H}^+ + \text{CH}_3^+$ is very small and the corresponding coincidence line is very faint. Lines of Coulomb-explosions with ^{13}C carbon isotopes are found in figure 5.4 as well as broad lines assigned to fragmentations with loss of one or two neutral hydrogen atoms. Impurities of the target gas, namely C_3H_6 molecules, create further coincidence lines.

5. Discussion

Summarizing, all double-ion coincidence channels that have been measured in previous experiments [XOY09b] and that are predicted by theory [MB08, PTS10], have been identified in the ToF correlation spectra. With identified masses and charges the momenta of all fragments can be calculated from the measured ToF and detector hit position with equations 3.2 and 3.3. For all two body Coulomb-explosions the sum momentum of the fragments vanishes due to momentum conservation. A momentum

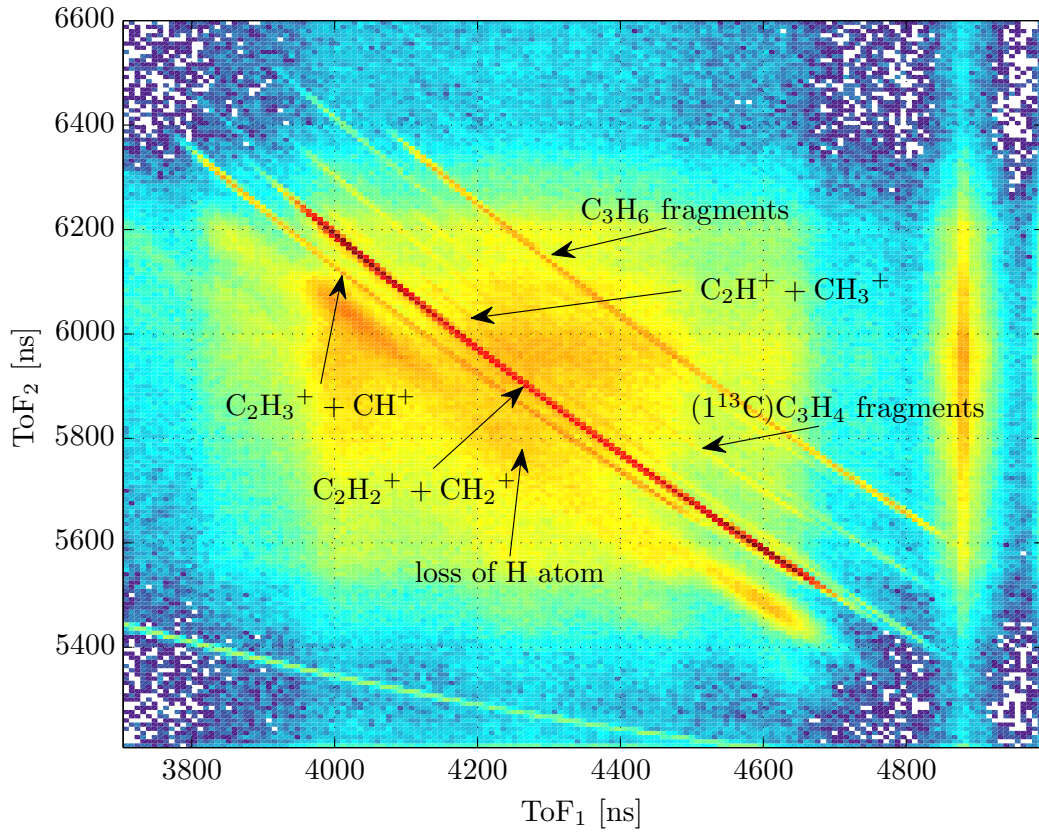
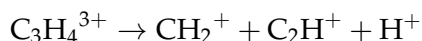


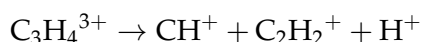
Figure 5.4.: Measured ToF correlation spectrum of allene with focus on C_2 -C coincidences. A logarithmic color scale is used.

sum condition will be used in the following sections to separate correlated events from uncorrelated detector hits. This will allow further quantitative analysis, for example on the kinetic energy release and the branching ratios of the identified coincidence channels.

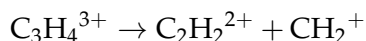
Despite intensive search no evidence of triple-ion coincidences has been found, neither in the double-ion ToF correlation spectra nor in the triple-ion ToF correlation spectra created with data from our experiments. The triple-ion Coulomb-explosions



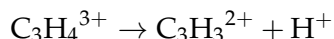
and



have been observed in previous experiments [XOY09a]. Searching for this specific ion combination with momentum sum conditions did not unveil such events either. In our analysis, a few candidates for these triple-ion coincidences fulfill the momentum sum conditions but they feature very low KERs. It is therefore concluded that they are most certainly created by false coincidences. The same applies to the double-ion Coulomb-explosions containing doubly charged fragments



and



predicted by theory [MBo8].

The absence of coincidences starting from triply charged parent ions is explained partly by a low detection acceptance for processes with large initial potential energies. At the used acceleration voltage of 400 V singly charged fragments with kinetic energies up to 6.25 eV are detected over the full solid angle. The mean KER of $\text{C}_3\text{H}_3^+ + \text{H}^+$ coincidences is measured as 4.6 eV (compare the calculated KER of $\text{C}_3\text{H}_3^+ + \text{H}^+$ coincidences in table 5.1). In coincidences that include the heavy allene fragments the proton's kinetic energy is approximately equal to the KER. If protons were created from triply charged parent ions, their kinetic energy would be roughly twice as high and therefore above the detector acceptance.

Nevertheless, in the cases where the proton travels towards the ion detector, coincidences from triply-charged parent molecules could have been measured. In this case, the electric field is high enough to prevent the low energetic heavy fragments from escaping. The only possible explanation for their absence is a very low probability to produce $\text{C}_3\text{H}_4^{3+}$ ions which have a vertical ionization potential of 53.05 eV [MBo8].

5.2.3. Kinetic energy releases measured with IR pulses

Measured KER spectra of the previously identified Coulomb-explosion channels of allene are plotted in figure 5.7. To reduce background of non-correlated events, a narrow

condition on the sum momentum of the fragments has been set for each channel. Still two uncorrelated ions can by chance fulfill this condition, especially if both have very low momenta. This for instance causes counts at low KERs of the $\text{C}_3\text{H}_3^+ + \text{H}^+$ channel in figure 5.7(a).

The interpretation of the obtained KER spectra is done in several steps that are listed below.

1. It is discussed **which information can be extracted from the measured KER spectra**. In section 4.1.3, it was explained that several conditions are required to calculate bond lengths from measured KER spectra. Most importantly the repulsive PES must be approximated by a Coulomb potential or it must be known. Furthermore all binding electrons must be removed within a timescale that is short compared to the vibrational and rotational times of the molecule. It will be shown that these requirements are not met in our experiment. Instead, the measured KERs will be used to test the energy difference E_{theo} between the transition states and final states calculated by [MBo8]. The relation between the KER and this energy difference E_{theo} is visualized in figure 5.5.
2. Mechanisms that might cause a **difference between measured KERs and E_{theo}** are explained.
3. **Measured KER spectra are presented**.
4. **Measured KERs are compared with predictions from theory**. It is shown that the KER_{min} values, where the KER distributions in figure 5.7 start to rise, are consistent with predictions from theory. The reasons for this are discussed.
5. It is shown that **laser pulse intensity and pulse length have no influence** on the measured KERs. KERs resulting from fragmentations induced by low intensity XUV pulses are consistent with those obtained from intense IR pulses. It is discussed that the intense laser field has no measurable influence on the PESs of allene dications.
6. The results obtained from the KER measurements are **summarized**. Furthermore the measured values are compared with KERs measured by other groups.

1. Information extracted from the KER spectra

In section 4.1.3 it was explained that the KER of a two body Coulomb-explosion contains information about the probability density of the initial molecule's vibrational wave function under certain conditions. The PES of the repulsive state must be known and all binding electrons must be removed within a time scale that is short compared to time scales of nuclear rearrangement.

The channels $\text{C}_2\text{H}_3^+ + \text{CH}^+$, $\text{C}_2\text{H}^+ + \text{CH}_3^+$ and $\text{C}_3\text{H}^+ + \text{H}_3^+$ show a distribution of hydrogen atoms that can only be explained by a migration of a proton. This is evident from the geometry of the neutral allene in figure 4.4. Therefore the anti-bonding PES causes a motion of neutral hydrogen atoms besides the repulsion of the charged fragments. This leads to the conclusion that the PES is not approximated by a Coulomb potential. The PES's exact shape has not been calculated and the first condition for successful reconstruction of the bond lengths of the original molecule is not fulfilled.

Doubly charged allene ions are detected in an amount that is comparable to the count rate of the Coulomb-explosion channels (compare section 5.2.4 where branching ratios of different channels are compared). The $\text{C}_3\text{H}_3^+ + \text{H}^+$ fragmentation channel results partly from a metastable $\text{C}_3\text{H}_4^{2+}$ molecular ion with a half-life of hundreds of nanoseconds. This indicates that at least one stable or metastable PES exists. As a result the excited $\text{C}_3\text{H}_4^{2+}$ molecular ion can vibrate within the local potential minimum until it eventually tunnels through the potential barrier. If the vibrational energy is high enough to form an isomer (for example cyclopropene or propyne), fragmentation channels like $\text{C}_3\text{H}^+ + \text{H}_3^+$ become accessible (compare figure 4.5). Both mechanism violate the second condition for Coulomb-explosion imaging because in those cases the binding electrons are not removed within a very short time. As a result these fragmentation channels will contain no information about the bond lengths or vibrational wave functions of the original allene molecule.

As a consequence of these considerations even potentially direct fragmentation channels like $\text{C}_2\text{H}_2^+ + \text{CH}_2^+$ can not be used for reliable geometry reconstruction of the neutral allene molecule. Instead, the measured KERs are used to test barrier heights of the PES calculated by A. M. MEBEL AND A.D. BANDRAUK [MBo8] and BRIAN T. PSCIUK ET AL. [PTS10, Table 2]. This is visualized with a one dimensional non-monotonic potential energy curve sketched in figure 5.5. The energy difference E_{theo} between a transition state and the total energy of the final fragments in figure 4.5 corresponds to the measured KER under certain conditions. These will be explained below in detail.

2. Possible differences between measured KERs and E_{theo}

Several effects can cause a deviation between the measured KER and E_{theo} .

- The final products might be rotationally and vibrationally excited which causes a reduction of the measured KER. This mechanism is indicated by the horizontal blue line in the bottom right of figure 5.5.
- In case of a low internal excitation, the Coulomb-explosion can be preceded by a tunnel process through the potential barrier. This causes a reduced measured KER as well. This mechanism is indicated by the red arrow in figure 5.5.
- Transition states define a saddle point in a multidimensional PES (schematics

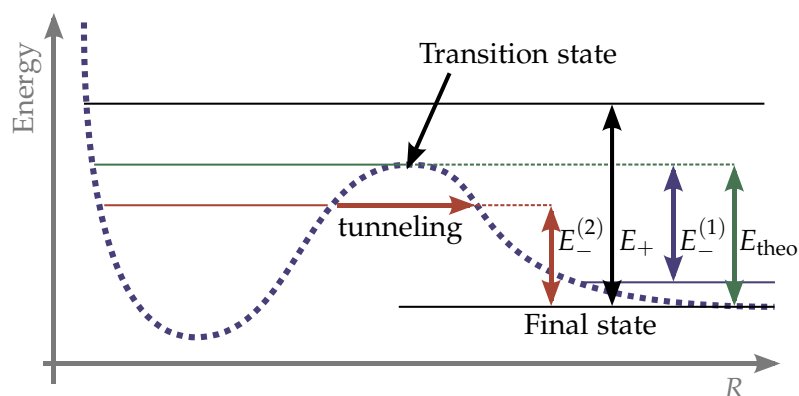


Figure 5.5.: Schematics of a non-monotonic potential energy curve. The energy difference between transition state and final state is given by E_{theo} . The measured KER corresponds to E_{theo} , if the energy level of the populated vibrational state is similar to the energy level of the transition state (green horizontal line). If the populated vibrational state is above the transition state, the measured KER corresponds to E_+ and it is higher than E_{theo} (this is indicated by the black horizontal line). If the final fragments are excited or if a metastable state decays by a tunneling process, the measured KER is similar to $E_-^{(1)}$ or $E_-^{(2)}$ respectively. In both cases it is smaller than E_{theo} (these mechanisms are indicated by the blue horizontal line and the red line and arrow).

in figure 5.6). The energetically most favorable fragmentation pathway leads through the saddle point (green curve in figure 5.6) with zero internal energy. Depending on the initial vibrational excitation, however, fragmentation processes may lead via other energetically higher paths (for example the red curve in figure 5.6). Other pathways might lead through the saddle point but with additional kinetic energy stored within the nuclear motion. Both processes will increase the measured KER if the excess energy is converted into kinetic energy of the fragments. This is indicated by the black horizontal line in figure 5.5.

3. Measured KER spectra

Table 5.1 compares measured KERs with calculated energy differences between transition states and final states. $\overline{\text{KER}}$ denotes the arithmetic mean of the experimental KER distributions¹. KER_{min} is a cutoff value at small energies where the counts in figure 5.7 reach 5% of the peak height. ΔKER is an estimation of the KER measurement

¹Only the main peaks in figure 5.7 are used to calculate $\overline{\text{KER}}$.

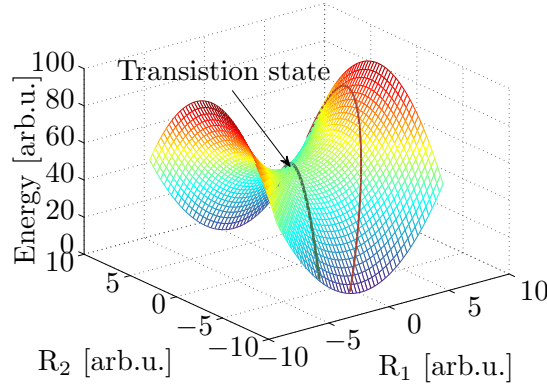


Figure 5.6.: Schematics of different pathways on a two dimensional PES. The green path leads through the transition state in the saddle point. This path will be energetically most favorable, if the saddle point is passed with zero internal energy. High internal excitation might result in a pathway that does not pass the saddle point (red curve) or passes through the transition state with additional vibrational energy stored in the nuclear motion.

Channel	$\overline{KER} \pm \Delta KER$ in [eV]	KER_{\min} in [eV]	$E_{\text{theo}}^{(1)}$ in [eV]	$E_{\text{theo}}^{(2)}$ in [eV]
$\text{C}_3\text{H}_3^+ + \text{H}^+$	4.6 ± 0.6	2.5	1.7, 2.4, 2.4 , 3.2 , 3.9	1.8, 2.5, 2.5 , 3.3 , 3.8
$\text{C}_3\text{H}_2^+ + \text{H}_2^+$	4.0 ± 0.5	2.0	–	–
$\text{C}_3\text{H}^+ + \text{H}_3^+$	3.8 ± 0.5	2.5	3.1, 3.4	–
$\text{C}_2\text{H}_2^+ + \text{CH}_2^+$	4.8 ± 0.6	3.0	3.1 , 4.2	3.3 , 4.2
$\text{C}_2\text{H}^+ + \text{CH}_3^+$	4.9 ± 0.6	3.0	1.9	2.5
$\text{C}_2\text{H}_3^+ + \text{CH}^+$	5.0 ± 0.6	3.5	4.0	4.0

Table 5.1.: Comparison of experimental KERs with theoretical predictions $E_{\text{theo}}^{(1)}$ [MBo8] and $E_{\text{theo}}^{(2)}$ [PTS10, Table 2]. \overline{KER} denotes the arithmetic mean of measured KER distribution. An estimation of the measurement uncertainty is given by ΔKER . KER_{\min} denotes a cutoff value at small energies. E_{theo} denotes the energy difference between transition state and final state (indicated in figure 5.5). Calculated KERs via direct fragmentation pathways are marked red (compare with red lines in figure 4.5).

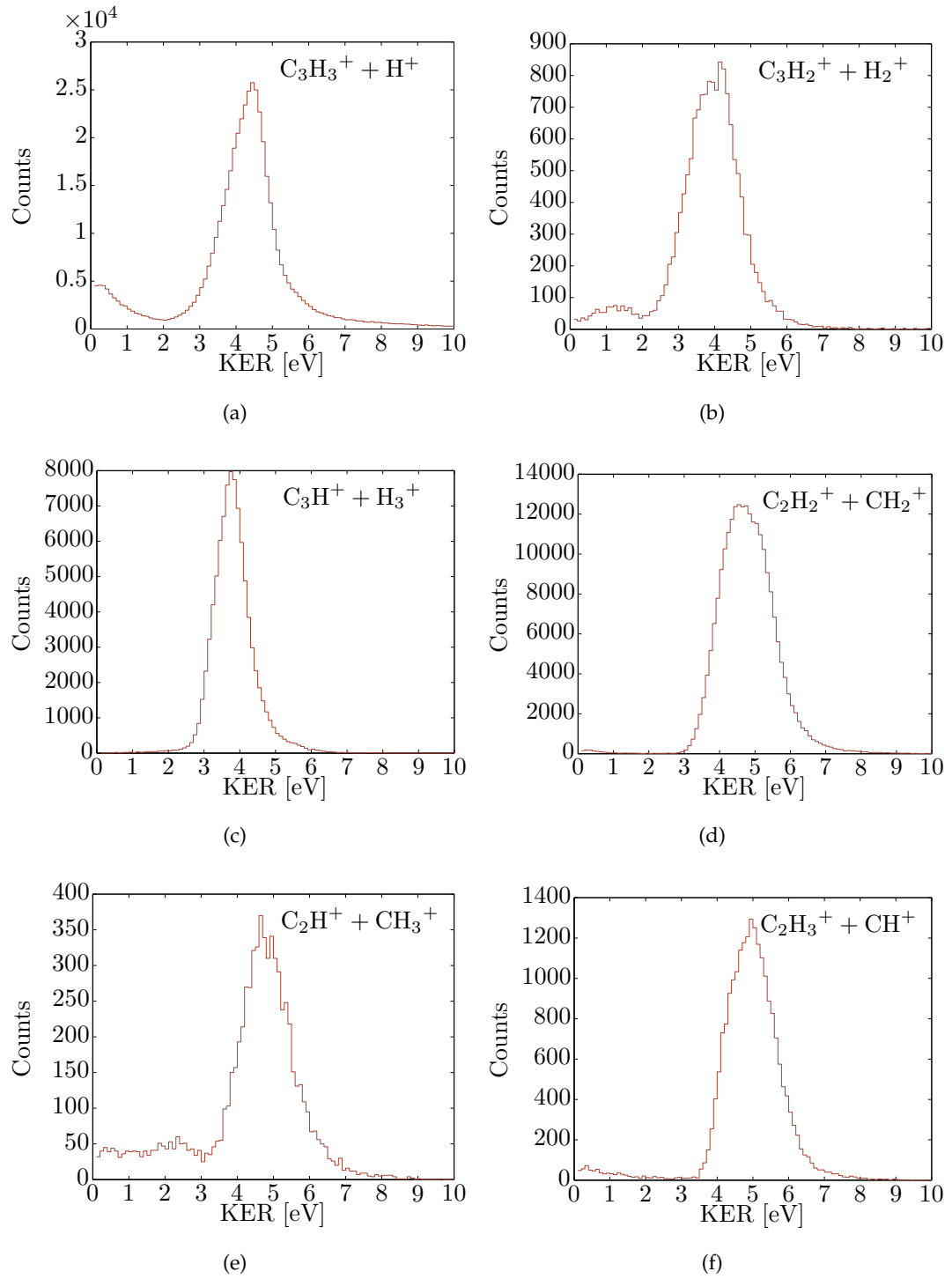


Figure 5.7.: Measured KERs of IR induced allene fragmentations at medium pulse intensity.

uncertainty calculated by

$$\Delta KER \approx \sqrt{\frac{2\bar{E}_1 (\Delta p_{sum}^y)^2}{m_1 \left(1 + \frac{m_2}{m_1}\right)} + \frac{2\bar{E}_2 (\Delta p_{sum}^y)^2}{m_2 \left(1 + \frac{m_1}{m_2}\right)}}. \quad (5.1)$$

The full-width-half-maximum (FWHM) of the sum momentum distribution in y -direction is given by Δp_{sum}^y . The masses and mean kinetic energies of the involved particles are given by $m_{1,2}$ and $\bar{E}_{1,2}$ respectively. For a derivation of equation 5.1 see appendix C. $E_{theo}^{(1,2)}$ denotes the calculated energy difference between transition state and final state of each fragmentation path (indicated in figure 5.5). The values $E_{theo}^{(1)}$ presented in table 5.1 correspond to the eleven calculated pathways in figure 4.5. The values $E_{theo}^{(2)}$ have been calculated by BRIAN T. PSCIUK ET AL. [PTS10, Table 2].

Predicted energy differences $E_{theo}^{(1,2)}$ of direct fragmentation paths are colored red (those fragmentation pathways are marked by red arcs in figure 4.5 as well) in table 5.1. Black values of $E_{theo}^{(1,2)}$ correspond to indirect pathways which feature a stable intermediate state and two barriers in the PES. It was shown in simulations that indirect pathways which involve one or more rearrangement steps are suppressed compared to direct paths [PTS10]. In this experiment the count rate of channels with direct paths is much higher than the count rate of channels that fragment only via indirect pathways (shown in section 5.2.4). The measured KER spectra of channels with both, direct and indirect pathways, is therefore assumed to be dominated by fragmentation via direct pathways.

4. Comparison of measured KERs with predictions from theory

Comparing the mean KER with the theoretical prediction shows that the measured KERs are larger than $E_{theo}^{(1,2)}$ for all channels. Furthermore the widths of the KER distributions are much broader than the energy separations of predicted pathways. This indicates that involved paths on the PES do either not lead through the transition states or lead through transition states but with a non-vanishing vibrational energy (compare figures 5.6 and 5.5). The KER_{min} , however, can be assigned to a fragmentation path through a saddle point without internal excitation. This value is consistent with the $E_{theo}^{(1,2)}$ for all channels² except $C_2H^+ + CH_3^+$ (its distribution is shown in figure 5.7(e)). For two channels, KER_{min} is slightly smaller than the smallest predicted KER. This could be explained by a non-vanishing internal excitation of the final fragments or a tunnel process through the PES barrier. Both mechanisms are visualized in figure 5.5.

The KER_{min} value of the $C_2H^+ + CH_3^+$ channel is larger than predicted by $E_{theo}^{(1)}$ and $E_{theo}^{(2)}$. Without information about the exact shape of the PES in the proximity of the transition state, there is no way to explain why this channel behaves differently from

²Only direct pathways are assumed to contribute to the measured KER spectrum of channel $C_3H_3^+ + H^+$.

the others. Future experiments which include electron detection might lead to a better understanding of this channel. The calculated values of this channel might not be too reliable either: of all fragmentation pathways the discrepancy between the calculated energies $E_{\text{theo}}^{(1)}$ and $E_{\text{theo}}^{(2)}$ is largest for the $\text{C}_2\text{H}^+ + \text{CH}_3^+$ channel. This might indicate that the calculation of this pathway causes numerical problems.

5. Influence of pulse intensity and pulse length on measured KERs

The KERs have been measured for different laser pulse intensities and different pulse lengths, but neither the mean KER nor the minimal KER value depends on these laser parameters. On the one hand this is surprising, because some channels feature several fragmentation pathways with different barrier heights. Higher laser intensities should address higher vibrational states of the $\text{C}_3\text{H}_4^{2+}$ molecular ion and fragmentation paths over higher barriers should become more pronounced. On the other hand both indirect fragmentation pathways of channel $\text{C}_3\text{H}^+ + \text{H}_3^+$ have nearly equal barrier heights of 3.49 eV and 3.20 eV. The direct pathways of $\text{C}_3\text{H}_3^+ + \text{H}^+$ feature transition states at 4.59 eV and 3.57 eV that are separated by 1.02 eV. The corresponding KERs, however, are only separated by 0.6 eV. This is about two times smaller than the FWHM of the $\text{C}_3\text{H}_3^+ + \text{H}^+$ KER distribution which might conceal small shifts of the KER. The $\text{C}_2\text{H}_2^+ + \text{CH}_2^+$ channel is assumed to be dominated by the single direct fragmentation path. For all other channels only one pathway is predicted. Therefore no shift in the KER is expected for those channels.

An increased laser intensity should populate higher vibrational energy levels which in turn result in an increased KER upon Coulomb-explosion (compare figure 5.5). The high energetic tails of the KER distributions, however, are independent of the laser intensity. This might indicate that the excitation to high vibrational energies is suppressed due to the Franck-Condon-principle.

The discussed KERs result from multi-photon double ionization by intense laser pulses with electric field strengths that are comparable to the Coulomb fields within the allene molecules. The laser field could therefore have a significant influence on the involved PESs and the measured KERs. To rule out such effects, the experiment has been repeated with XUV pulses. In this measurement, single-photon double ionization is the dominating process for $\text{C}_3\text{H}_4^{2+}$ production and field strengths are extremely small. The measured KERs of the XUV experiment are consistent with those created from IR pulses. Details concerning the measurement with XUV pulses are given in section 5.3 and measured KER spectra are shown in appendix D.

6. Summary In an earlier experiment by another group, the KERs of the $\text{C}_2\text{--C}$ channels were measured as 6.2 eV and the KERs of the $\text{C}_3\text{--H}$ channels were measured as 4.6 eV [XOYogb]. The latter is consistent with the $\overline{\text{KER}}$ values of the $\text{C}_3\text{--H}$ channels in table 5.1. The $\overline{\text{KER}}$ values of the $\text{C}_2\text{--C}$ channels in table 5.1 differ significantly from

the previously measured ones. A reason for this deviation has not yet been found.

Summarizing, the KERs measured in our experiment were used to test the predicted energy differences between transition states and final states E_{theo} . It was found that the KER_{min} values are consistent with $E_{\text{theo}}^{(1,2)}$ for all fragmentation channels except the $\text{C}_2\text{H}^+ + \text{CH}_3^+$ channel. In addition the measured KER distributions are independent of the laser intensity. A hypothesis for this observation was proposed. KER distributions measured from fragmentations induced by XUV pulses indicate that the PESs of doubly charged allene are not distorted significantly by the intense IR pulse. This finding is important if results from IR measurements are used to draw conclusions about the undisturbed allene PESs.

5.2.4. IR pulse parameter variation and branching ratios

While the measured KERs are independent of the laser pulse parameters, it will be shown in this section that the count rates of the coincidence channels depend on the pulse intensity and pulse length. Count rates of different channels are compared for each set of laser parameters as well. Both analyses give additional insight into the processes leading to the Coulomb-explosions. This section is divided into the following paragraphs:

1. The first paragraph explains how the **normalization of fragmentation channels** is done to obtain the branching ratios. The branching ratio of a channel is defined as the ratio of the number of fragmentations via this channel to the total number of fragmentations starting from the same parent ion.
2. Afterwards it is explained how **pulse parameters have been varied** during the conducted experiment.
3. A **qualitative analysis of the branching ratios of all coincidence channels** is performed. Branching ratios of direct and indirect fragmentation pathways are analyzed. Furthermore the branching ratio of stable and unstable $\text{C}_3\text{H}_4^{2+}$ dications at different pulse parameters is discussed.
4. A **quantitative analysis of the $\text{C}_2\text{-C}$ channels** is performed.
5. All results obtained from the pulse variation are **summarized**.

1. Normalization of fragmentation channels

The vertical ionization energy of the allene dication is 28.05 eV. With spectrally broadened IR light with a center wavelength of 745 nm 17 photons are required to deliver this energy. The average number of photons interacting with a single allene molecule increases with the laser intensity. This results in an intensity dependent production rate of allene dications to which the production of fragmentation channels must be

normalized in order to obtain the branching ratios. The branching ratio of a certain channel is given by the number of fragmentations via this channel normalized to the total number of fragmentations from the same parent ion. In our experiment, the parent ion itself can be stable and the creation of *stable* $\text{C}_3\text{H}_4^{2+}$ dications is also considered a “fragmentation” channel. The total number of created allene dications N_{dication} is calculated by

$$N_{\text{dication}} = N_{\text{C}_3\text{H}_4^{2+}} + \sum_{\text{coinc}} N_{\text{coinc}}, \quad (5.2)$$

$$N_{\text{C}_3\text{H}_4^{2+}} = \frac{N'_{\text{C}_3\text{H}_4^{2+}}}{\epsilon}, \quad (5.3)$$

$$N_{\text{coinc}} = \frac{N'_{\text{coinc}}}{\epsilon^2} \gamma_{\text{coinc}}. \quad (5.4)$$

$\epsilon = 0.5$ denotes the estimated detection efficiency of the MCP detectors. It is independent of ion species or their momentum distribution. The number of *created* stable $\text{C}_3\text{H}_4^{2+}$ dications is given by $N_{\text{C}_3\text{H}_4^{2+}}$. It is calculated from the *detected* $\text{C}_3\text{H}_4^{2+}$ dications given by $N'_{\text{C}_3\text{H}_4^{2+}}$ with equation 5.3. N_{coinc} denotes the total number of fragmentations per channel. It can be calculated from the *detected* coincidences N'_{coinc} of each fragmentation channel with equation 5.4. To measure a two body event, both fragments must be detected and ϵ is squared to take this into account. γ_{coinc} compensates for a detection efficiency that is dependent on the ion species. Its origin is briefly explained below. A detailed analysis of the problem is done in appendix E.

$\gamma_{\text{C}_3\text{-H}}$ compensates for a detection efficiency of $\text{C}_3\text{-H}$ coincidences that is dependent on the initial momentum of the C_3H_i^+ , $i \in \{1, 2, 3\}$ fragments and the total count rate and thereby on the laser intensity. The effect is shown in the spectrum in figure E.1 in appendix E. It originates from the high number of created ions per laser pulse (up to eight ions are detected per pulse at high IR intensity). Most of them are singly charged recoil ions. They all hit the detector within a few hundred nanoseconds and many of them are not detected due to detector dead times. If the ToFs of coincident C_3H_i^+ fragments are similar or larger than those of the recoil ions, their detection is less probable. The fraction of lost coincidences increases with the pulse intensity, because the total count rate increases as well.

A method was developed to estimate the number of lost events due to these effects. It is described in appendix E. $\gamma_{\text{C}_3\text{-H}} > 1$ compensates for the $\text{C}_3\text{-H}$ coincidences that were not measured due to detector dead times. Values for $\gamma_{\text{C}_3\text{-H}}$ are given in appendix E. The fragments of $\text{C}_2\text{-C}$ coincidences are not affected by this intensity dependent detector efficiency, because they have much smaller ToFs than the recoil ions. Therefore $\gamma_{\text{C}_2\text{-C}}$ equals unity. It is important to emphasize that the number of created $\text{C}_3\text{-H}$ coincidences is an estimation and should only be used for qualitative analysis. The number of $\text{C}_2\text{-C}$ coincidences is considered more reliable and will be used for quantitative analysis as well.

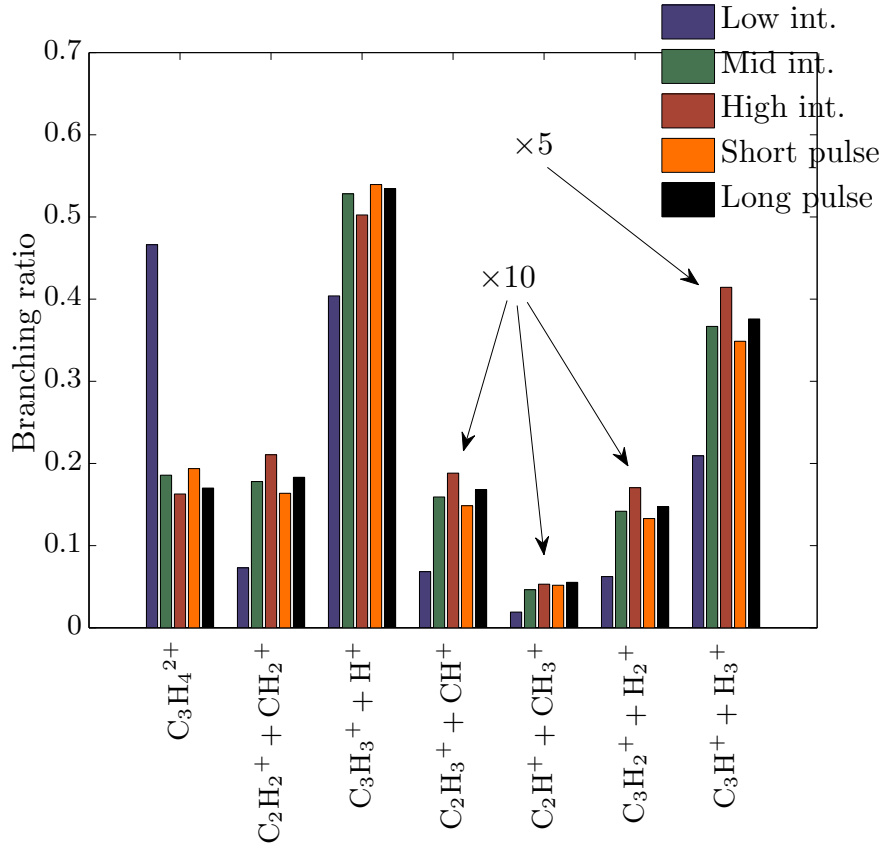


Figure 5.8.: Branching ratios of all channels. The absolute number of events per channel is reconstructed with equations 5.3 and 5.4. The branching ratios of channels $C_2H_3^+ + CH^+$, $C_2H^+ + CH_3^+$ and $C_3H_2^+ + H_2^+$ are multiplied by a factor of 10 and the branching ratio of channel $C_3H^+ + H_3^+$ is multiplied by a factor of 5.

2. Varied pulse parameters

Figure 5.8 shows the branching ratios of the fragmentation channels and the $C_3H_4^{2+}$ channel. The colors represent different laser parameters. The intensity variation has been performed with a motorized aperture in the IR path of the HHG chamber without changing any other laser parameters.

For the pulse length variation, long pulses were produced with a 2 mm thick glass window which has been placed behind the chirped mirror compressor in order to increase the pulse length from about 10 fs to more than 25 fs. The short pulse measurement was done without the window. The opening of the aperture was slightly larger in the long pulse measurement to compensate for the reflections on the glass. The average power behind the aperture was the same for both pulse lengths.

The pulse length variation was conducted a few days after the intensity variation and

the laser system had to be realigned in between³. The pulses are therefore not directly comparable to the intensity variation. The intensity of the pulse length variation should correspond approximately to the medium intensity of the intensity variation. The pulse lengths of the intensity variation should correspond approximately to the short pulses of the length variation.

3. Qualitative analysis of all coincidence channels

On a qualitative level, two important features of figure 5.8 can be analyzed. First, the branching ratio of coincidences with direct pathways ($C_2H_2^+ + CH_2^+$ and $C_3H_3^+ + H^+$) is one order of magnitude larger than that of channels with only indirect pathways ($C_2H_3^+ + CH^+$, $C_2H^+ + CH_3^+$ and $C_3H^+ + H_3^+$). This is true for all laser parameters and it is predicted by theory [PTS10] and has been measured in earlier experiments [XOY09b] as well. If two channels with direct pathways ($C_2H_2^+ + CH_2^+$ and $C_3H_3^+ + H^+$) are compared with each other, the channel with the lower barrier in the PES has the larger branching ratio. The same is true if the indirect channels $C_2H_3^+ + CH^+$, $C_2H^+ + CH_3^+$ and $C_3H^+ + H_3^+$ are compared with each other.

The second feature of the bar chart 5.8 is the decrease of the branching ratio of stable $C_3H_4^{2+}$ molecular ions for increasing laser intensity. The pulse length does not have a large effect on the branching ratios but the production of stable $C_3H_4^{2+}$ is slightly increased for short pulses. This is consistent with the picture that the field of a long pulse perturbs the PES for a longer time and might trigger a Coulomb-explosion.

4. Quantitative analysis of C_2 -C channels

Figure 5.9 shows the production of C_2 -C coincidences and stable $C_3H_4^{2+}$ molecular ions normalized to the total production of these channels. This means branching ratios are calculated only from the count rates of these four channels. The detection efficiency for these channels is does not suffer from a count rate dependence like the C_3 -H coincidences. The bar chart in figure 5.9 can therefore be used for a quantitative analysis.

At increasing pulse intensity, the branching ratio of stable $C_3H_4^{2+}$ decreases by nearly a factor of two. This indicates that one or more stable and one or more dissociating states of the allene dication exist. The probability to excite the allene dication to an anti-bonding PES increases with increasing laser intensity. It is concluded that – in the Franck-Condon region – the repulsing PESs are energetically higher than the binding PESs.

Additional information about the PES of the anti-bonding state can be extracted from figure 5.10 which compares branching ratios of the C_2 -C coincidence channels. The branching ratio of these channels is almost independent of the laser parameters.

³This has to be done regularly due to temperature or humidity drifts in the oscillator and amplifier.

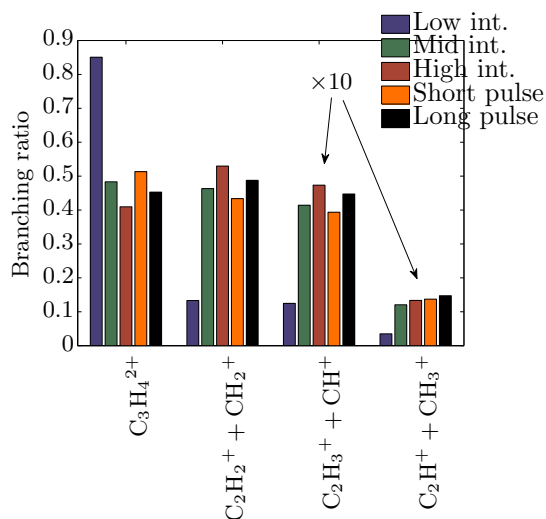


Figure 5.9.: Branching ratios of C_2 -C coincidences and stable $C_3H_4^{2+}$ for different laser parameters. The branching ratios of channels $C_2H_3^+ + CH^+$ and $C_2H^+ + CH_3^+$ are multiplied by a factor of 10.

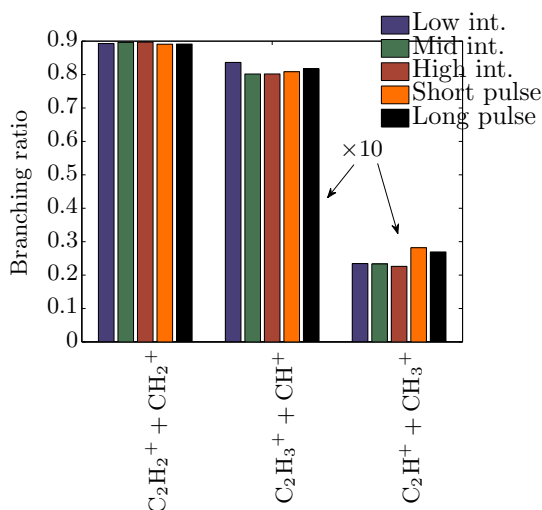


Figure 5.10.: Branching ratios of C_2 -C coincidences for different laser parameters. The branching ratios of channels $C_2H_3^+ + CH^+$ and $C_2H^+ + CH_3^+$ are multiplied by a factor of 10.

The transition states of these pathways, however, are separated by approximately 0.9 eV [MBo8] (compare figure 4.5) or 0.7 eV [PTS10, Table 2], depending on the applied computational method. With this knowledge it can be concluded that all populated dissociating molecular states are energetically above the highest transition state and all populated dissociating states feature similar branching ratios. Otherwise an intensity dependent branching ratio would have been measured because the population of energetically separated dissociating states depends on the laser pulse intensity.

Assuming all populated dissociating states are energetically above the barriers, the measured KER should only depend on the energy difference between the dissociating states and the final fragments of the C_2 -C coincidences. This is visualized by the black horizontal line in figure 5.5. As discussed above, the dissociating states are similar for all C_2 -C fragmentation channels. Therefore the energy difference of the final fragments should be equal to the energy difference of the measured KERs. The energies of the final fragments are separated by 3.1 eV [MBo8] (compare figure 4.5) or 1.7 eV [PTS10, Table 2], depending on the computational method. This is in contradiction to the measured KERs for the three C_2 -C fragmentation channels which are nearly equal.

5. Summary

It was shown in this section that the branching ratios between stable and unstable allene dications is dependent on the pulse intensity. Production of stable $C_3H_4^{2+}$ is favored

at low intensities. The pulse length does not effect branching ratios significantly. The branching ratio of fragmentation channels with a direct pathway is more than one order of magnitude larger than that of channels with only indirect pathways. If a channel with direct fragmentation pathways is compared to another, the channel with the lower barrier in the PES has a higher branching ratio. The same is true if a channel with only indirect fragmentation pathways is compared to another.

The calculated barrier heights of the C₂-C channels are separated by at least 0.7 eV [PTS10, Table 2] and the measured branching ratios are independent of the laser parameters. This is only possible if all populated dissociating states are energetically above the highest barrier. Furthermore all populated dissociating states must have the same branching ratio. If all C₂-C fragmentations started from the same dissociating state, the measured KERs would differ by at least 1.7 eV according to calculated energies of final fragments [PTS10, Table 2]. This is not the case. The only explanation for this discrepancy are systematic errors in the experiment, a wrong interpretation of the data or errors in the calculated PES. The KERs measured by H. XU ET AL [XOY09b] are equal for all C₂-C channels. This is an indication that no systematic errors were made in our experiment.

In earlier experiments the production ratio of the channels C₂H₂⁺ + CH₂⁺, C₂H₃⁺ + CH⁺ and C₂H⁺ + CH₃⁺ was measured as 1 : 0.08 : 0.03 [XOY09b] (the count rates were normalized to the number of coincident C₂H₂⁺ + CH₂⁺ fragments). This ratio is consistent with 1 : 0.091 : 0.028 measured in this work⁴ which is a further indication that the branching ratio of these channels does not depend much on the pulse parameters.

5.2.5. Half-life of metastable allene dications

The elongated coincidence line in the allene ToF correlation spectrum (figure 5.2) indicates a C₃H₃⁺ + H⁺ Coulomb-explosion starting from a metastable parent ion. In this section the half-life of this dication is calculated from measured ToF spectra. A quantitative analysis of the half-life is done in the following steps:

1. A so called polygon condition can be used to select a certain area of a spectrum for further processing. Here a polygon condition is used to **isolate C₃H₃⁺ + H⁺ coincidences** that cause the correlation line of the ToF correlation spectrum. The ToFs of the selected fragments are further processed in step 3.
2. With an event mixing technique a **background spectrum** of false coincidences is created.
3. In ToF spectra or ToF correlation spectra, ion counts are plotted as a function of the time-of-flight. To calculate the half-life from the ion distribution, **the measured ToFs must be mapped to decay times τ** . This is achieved by an algorithm based on the simulation of delayed Coulomb-explosions.

⁴This ratio is the average value of the branching ratios for different laser parameters.

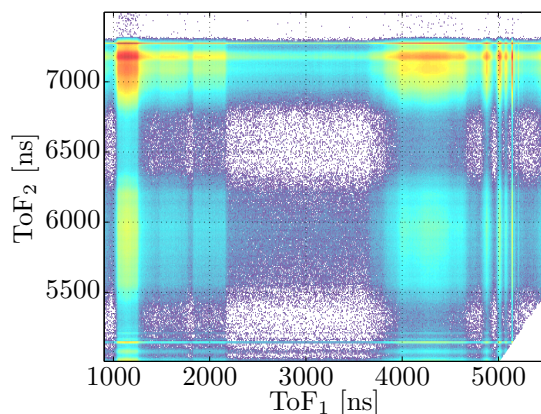


Figure 5.11.: ToF correlation spectrum created with the event mixing technique. Only non-correlated events appear in this spectrum. Therefore it can be used for background subtraction.

4. The **developed ToF to τ mapping** is tested in a simulation.
5. The **half-life of metastable allene dications** is calculated from measured ToF spectra of the protons with the ToF to τ mapping.
6. The experimental results are analyzed in a **conclusion**.

1. Isolation of $\text{C}_3\text{H}_3^+ + \text{H}^+$ coincidences

The polygon conditions of the Go4 data analysis framework allow to select the events on the $\text{C}_3\text{H}_3^+ + \text{H}^+$ coincidence line of the ToF correlation spectrum (shown in figure 5.2) for further processing. The ToFs of the selected coincident protons are then projected onto the ToF_1 -axis. The resulting spectrum is shown in figure 5.12. The projection onto the ToF_2 -axis creates a ToF spectrum of coincident C_3H_4^+ molecular ions (not plotted). The polygon condition removes most protons from false coincidences and most protons from other coincidence channels. This is evident when the figures 5.12 and 5.1 are compared. The former was created with the polygon condition, the latter incorporates all detected ions. A few false coincidences, however, remain in the first figure as well, especially for ToFs, where the coincidence line crosses horizontal or vertical lines in the ToF correlation spectrum (compare figure 5.2).

2. Creation of background spectra

To take remaining false coincidences into account, a background spectrum was created with an event mixing technique: ToFs from two different laser shots were randomly chosen and plotted into the same ToF correlation spectrum. The result is a spectrum that contains only false coincidences which is plotted in figure 5.11. By applying the

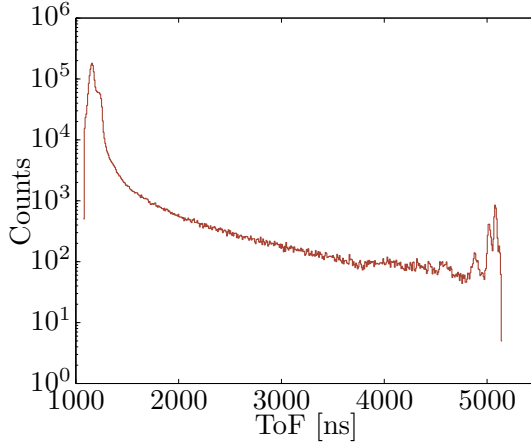


Figure 5.12.: ToF spectrum of protons from the coincidence line of the ToF correlation spectrum. A logarithmic scale on the y -axis is used.

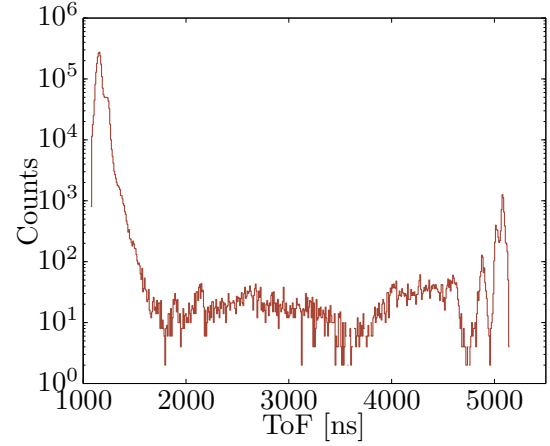


Figure 5.13.: Background ToF spectrum of protons created with the event mixing technique. A logarithmic scale on the y -axis is used.

same polygon condition to this spectrum and projecting the false coincidences onto the ToF_1 - and ToF_2 -axis, ToF spectra of false coincidences are created. The background spectrum for ToFs of protons is shown in figure 5.13. If it is subtracted from the ToF spectrum of the real coincidences, a ToF spectrum with a reduced number of false coincidences is obtained. The result is plotted in figure 5.16 where the measured ToFs of protons are already converted to a decay time τ with a method described in the next paragraph.

3. Mapping of ToFs to decay times τ

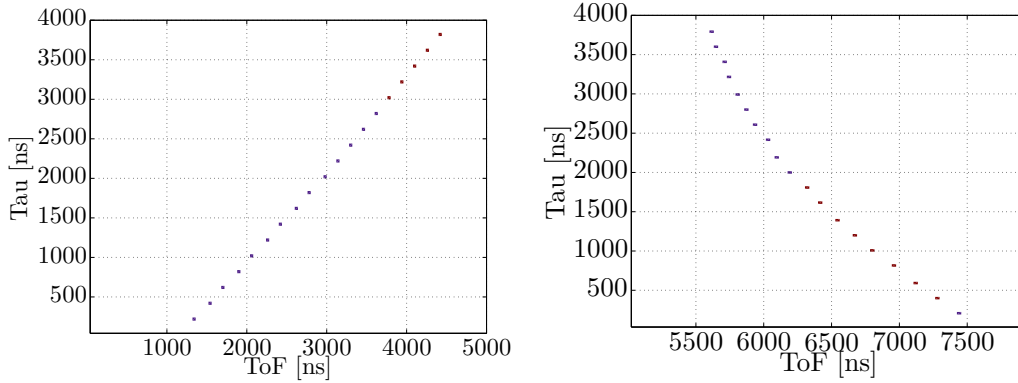
The linear decrease of the counts in the interval between 1500 ns and 4000 ns in the ToF spectrum of protons in figure 5.12 indicates an exponential decay. For a quantitative analysis, however, measured times-of-flight T_i must be mapped to decay times τ of the parent ion. If the decay time τ of an event is known, the expected ToF can be calculated by the equations

$$T_i = \tau + T_{\text{fragment}}, \quad (5.5)$$

$$T_{\text{fragment}} = \frac{m_i(2l - 2z_M)}{\frac{m_i}{M}p_M^z + \sqrt{\left(\frac{m_i}{M}p_M^z\right)^2 + 2m_iq_iU\frac{(l-z_M)}{l}}}, \quad (5.6)$$

$$z_M = \frac{1}{2} \frac{U}{l} \frac{q_M}{M} \tau^2, \quad (5.7)$$

$$p_M^z = \frac{U}{l} \frac{q_M}{M} \tau. \quad (5.8)$$



(a) Spectrum of decay times τ over simulated ToFs of protons.

(b) Spectrum of decay times τ over simulated ToFs of C_3H_3^+ fragments.

Figure 5.14.: Both figures have been created from simulated delayed Coulomb-explosions with fixed decay times in intervals of $\Delta\tau = 200\text{ ns}$ and with zero KER.

Here q_M and M denote the charge and mass of the parent ion. The mass and charge of the fragment are given by m_i and q_i . The acceleration voltage and spectrometer length are given by U and l . These equations assume a vanishing KER⁵.

In the experiment T_i is measured and τ is unknown, but solving above equations for τ analytically is difficult. Instead they are solved numerically by simulating delayed Coulomb-explosions with fixed decay times τ of the metastable parent ion. These fragmentation processes are simulated with zero KER and τ is varied in small steps. For each value of τ the ToFs of the two simulated fragments are calculated with equation 5.5. Plotting τ over the simulated ToF of the proton and the C_3H_3^+ fragment results in the spectra shown in figures 5.14(a) and 5.14(b).

The data points in figure 5.14(a) are not exactly placed in a straight line and linear interpolation on the set of data points is used to assign a decay time τ to each ToF of a proton⁶. This linear interpolation is used below to map the experimental ToF histogram of protons (figure 5.12) to the τ histogram shown in figure 5.16. A similar linear interpolation is performed on figure 5.14(b) to map ToFs of C_3H_3^+ fragments to decay times τ .

4. Test of the developed ToF to τ mapping

To test the ToF to τ mapping algorithm described above and to measure the influence of a non-vanishing KER, a delayed Coulomb-explosion into $\text{C}_3\text{H}_3^+ + \text{H}^+$ fragments

⁵The corresponding equations that incorporate the KER are used to create simulated ToF spectra of delayed Coulomb-explosions (compare section 4.3.2).

⁶Figures 5.14(a) and 5.14(b) are plotted with a coarse binning and a large step size of τ for increased visibility. For the linear interpolation a fine binning of 5 ns per bin and $\Delta\tau = 50\text{ ns}$ has been used.

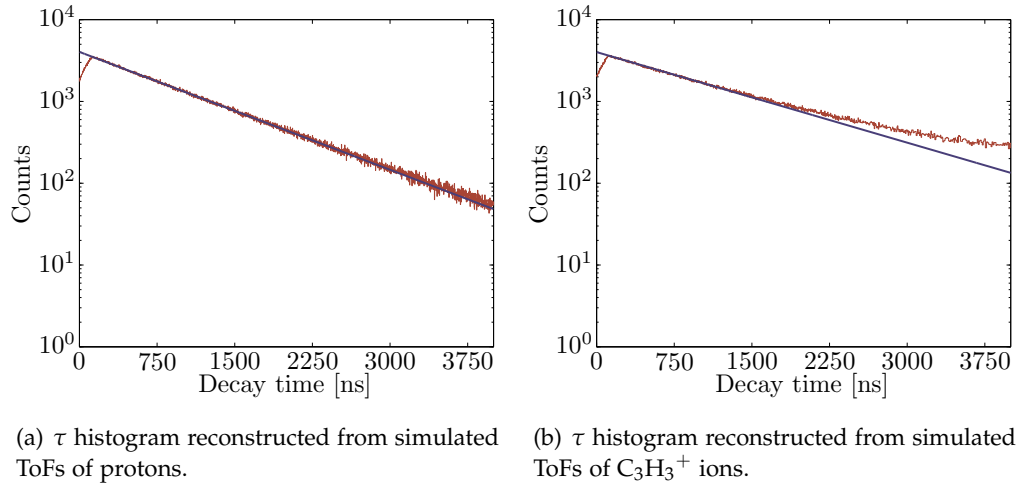


Figure 5.15.: A simulated delayed Coulomb-explosion with 600 ns half-life and initial distance of 6 a. u. has been used to create these spectra. A logarithmic scale on the y -axis is used.

has been simulated with an exponential distribution of decay times τ . The initial distance of 6 a. u. has been chosen to correspond to the measured KER of 4.6 eV of this coincidence. The metastable parent ions have been simulated with a half-life of 600 ns. The ToF spectra of the simulated fragments are mapped to τ spectra with the linear interpolation described above. The τ histogram extracted from the simulated ToFs of protons is plotted in figure 5.15(a) with an exponential function fitted to the data points. The half-life of this function is 626 ns which is slightly higher than the half-life of 600 ns used to simulate the delayed Coulomb-explosions. This difference can be explained by two effects.

First, the simulated ToFs do not only depend on the times of decay, but also on the direction of the initial momenta of the simulated particles. These momenta, however, are not taken into account by equation 5.5 and therefore the reconstructed decay times τ are distorted by the initial momenta. This explains the increasing number of counts for decay times between 0 and 150 ns in figure 5.15(a). For $\tau > 150$ ns the slope of the distribution is not altered significantly by the non-zero KER. If the exponential function is only fitted to data points with $\tau > 150$ ns, the KER has no large influence on the reconstructed half-life.

The second effect is connected to the non-linearity of equations 5.5 to 5.8 and the binning of the spectra. The reconstruction of the decay time τ is done in two steps. First, a ToF spectrum of the fragments of the delayed Coulomb-explosions is created. Afterwards the decay time is reconstructed from the ToF spectrum. The binning in the first step causes an inexactness, as the following examples demonstrate:

1. An ideal algorithm without the intermediate step of plotting the ToF spectrum

would not cause the binning effect, because it would use the *exact* ToF to reconstruct τ . In this case a (simulated) uniform τ distribution would be reconstructed as uniform distribution. Mathematically this is possible because equation 5.5 is bijective in the relevant τ and ToF range.

2. An algorithm using an intermediate step of creating a ToF spectrum will give a different result: in figures 5.14(a) and 5.14(b) fixed decay times at regular intervals of 200 ns are plotted over the simulated ToFs. While the intervals between the decay times are equal, the intervals of the simulated ToFs are not equal. As a result a *uniform* distribution of (simulated) decay times τ will cause a *nonuniform* ToF distribution if the bin size of the ToF-axis is constant. If such a ToF spectrum is used to reconstruct the original decay time τ , the reconstructed τ distribution is not uniform either. Mathematically this happens because the binning of the ToFs is a non-reversible operation.

Due to these binning effects, the half-life of the metastable allene state reconstructed from the ToF spectrum is larger than originally simulated. If the ToFs of protons are used for reconstruction of τ , the binning effect will be small, because the interpolation on the data points in figure 5.14(a) is close to a straight line. For the heavy C_3H_3^+ fragments, however, the binning effect will be significant due to the curvature in figure 5.14(b).

Figure 5.15(b) shows the decay time histogram reconstructed from the simulated C_3H_3^+ ToFs. The exponential function only describes the data for small times of decay $\tau \lesssim 1500$ ns. Furthermore, the fitted half-life of 815 ns is much larger than the value of 600 ns that was originally used to simulate the delayed Coulomb-explosions. This significant difference is caused by the binning effect discussed above. Due to this, the experimental ToFs of C_3H_4^+ fragments are not used to calculate the half-life of the metastable allene dications.

5. Calculated half-life of metastable allene dications

The $\text{C}_3\text{H}_3^+ + \text{H}^+$ coincidence line of the measured ToF correlation spectra is used for a half-life calculation of the metastable allene dications. Only the spectra acquired at low and medium IR pulse intensities are used for the half-life calculation. At high IR intensities the number of false coincidences is too high for effective background subtraction due to lost events at the high count rates (compare appendix E). For the data taken at medium pulse intensities the background subtraction described in step 2 (page 71) is used to remove false coincidences. At low pulse intensity a background subtraction is not necessary due to a small number of false coincidences. τ histograms for both laser intensities are plotted in figures 5.16 and 5.17⁷.

⁷The bin size in figure 5.17 is larger than that in 5.16. This has only a very small effect on the fitted half-life but reduces the statistical fluctuation at low laser intensity which makes the trend of the distribution visible with the naked eye.

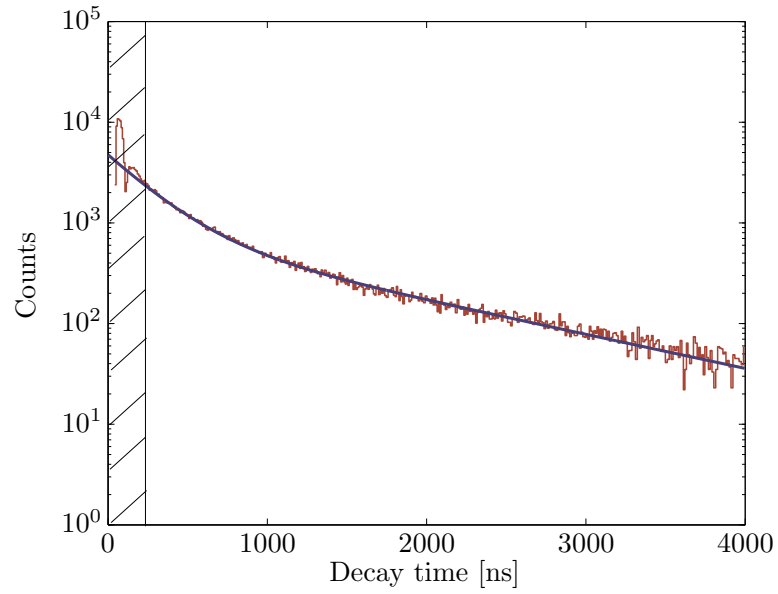


Figure 5.16.: Histogram of decay time τ at medium pulse intensity, background corrected. A logarithmic scale on the y -axis is used.

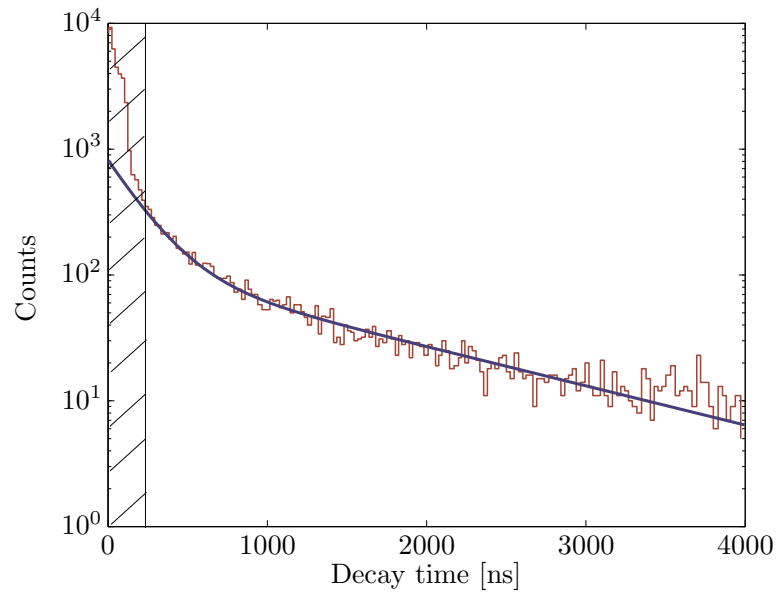


Figure 5.17.: Histogram of decay time τ at low pulse intensity. A logarithmic scale on the y -axis is used.

A sum of two exponential functions

$$f(\tau) = ae^{-b\tau} + ce^{-d\tau} \quad (5.9)$$

is used to fit both spectra. The data within the shaded area ($\tau < 248$ ns) is excluded from the fitting algorithm because its structure mainly results from immediate fragmentation and background effects. The obtained fitting parameters are given in table 5.2. At both intensities, an exponential function with a short half-life $T_{1/2}^b$ describes the steep increase of counts towards low τ . The long tail in the spectra is described by the long half-life $T_{1/2}^d$ of the second exponential function. The fitted half-lives at both intensities are consistent with each other.

Parameter	medium intensity	low intensity
a	3946	707
b	$0.0036 \text{ }^1/\text{ns}$	$0.0048 \text{ }^1/\text{ns}$
$T_{1/2}^b = \ln 2/b$	193 ns	144 ns
c	807	113
d	$0.00078 \text{ }^1/\text{ns}$	$0.00072 \text{ }^1/\text{ns}$
$T_{1/2}^d = \ln 2/d$	889 ns	963 ns

Table 5.2.: Fitting parameters for measured τ histograms.

6. Conclusion

The appearance of two different half-lives indicates at least two types of metastable states. The appearance of several half-lives has been observed for other dication species before [FE93]. The calculated half-life of the fast decay is consistent with the value of 190 ns estimated from the angular distribution of the $\text{C}_3\text{H}_3^+ + \text{H}^+$ explosions by H. XU ET AL [XOY09b]. The slow decay, however, has not been measured in previous experiments.

A simulated ToF correlation spectrum of the $\text{C}_3\text{H}^+ + \text{H}_3^+$ channel is plotted in figure 4.14. The exponential decay of the metastable dication was simulated with a half-life of 15 ns. A comparison with the measured ToF correlation spectrum in figure 5.2 reveals that the half-life in the experiment is slightly larger than 15 ns. It was tried to perform a quantitative analysis of the $\text{C}_3\text{H}^+ + \text{H}_3^+$ channel with an algorithm similar to the one described above. However, this was not successful since it was impossible to distinguish the KER effects from the delay effects in the corresponding τ spectrum due to the short half-life. A mechanism, which explains a delayed $\text{C}_3\text{H}^+ + \text{H}_3^+$ coincidence is described by theory [MBo8]. But for the $\text{C}_3\text{H}_3^+ + \text{H}^+$ coincidence such a mechanism is not reported.

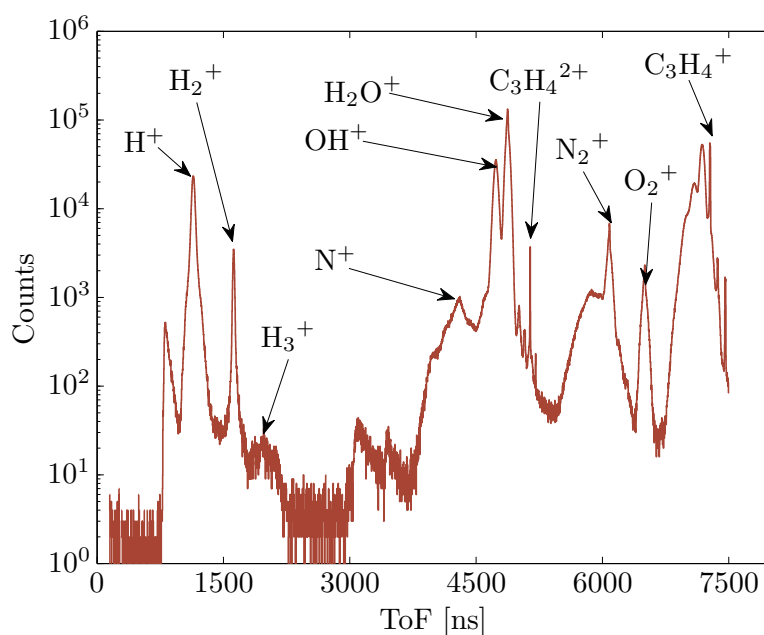


Figure 5.18.: Allene ToF spectrum with XUV pulses. A logarithmic scale on the y -axis is used.

5.3. Conducted XUV single pulse experiment

Ionization of allene molecules with intense IR laser pulses allows to create a large number of doubly charged allene dications in a short measurement time by multi-photon ionization. This comes at the disadvantage of numerous events per laser pulse – most of them singly charged allene – which increases the probability to detect false coincidences in the C_3 -H channels.

Measurements with XUV pulses can create cleaner spectra because ionization is done by single, highly energetic photons. An allene ToF spectrum created with XUV pulses is plotted in figure 5.18. This spectrum is largely dominated by fragments from the residual gases H_2O , N_2 and O_2 . About one third of the counts is caused single ionized molecules.

The total cross section for single-photon double ionization is smaller than the total cross section for single ionization with a single photon. This explains the small number of $C_3H_4^{2+}$ counts in figure 5.18 despite the vertical ionization potential of 28.05 eV [MBo8] which is in the energy range of the XUV photons. Due to the low production rate of $C_3H_4^{2+}$ ions, only a small number of Coulomb-explosion events has been detected in the XUV measurement. Measured KERs of Coulomb-explosions induced by XUV photons (shown in appendix D) are consistent with the IR measurement.

Summarizing, allene fragmentation in weak electric fields of XUV pulses does not reveal new information on the PESs. This indicates that the allene PESs are not

altered considerably by the intense laser fields of IR pulses. Only with this knowledge spectra from multi-photon ionization can be used to obtain information about the PESs of undisturbed allene dications. The low cross section for double ionization with XUV photons should be considered when interpreting the results of the pump-probe measurement presented in the next section.

5.4. Conducted XUV-IR Pump-probe experiment

The idea of pump-probe Coulomb-explosion imaging experiments has been described in section 4.1.4: double ionization by the XUV pulse starts an isomerization process of a stable allene dication state. After a variable time delay, the molecular ion is excited to an anti-bonding PES by the IR laser pulse. The measured momenta and KERs of the resulting fragments contain information about the molecular geometry at the time of excitation by the second pulse.

To gain information about bond angles, triple-ion Coulomb-explosions are required and the doubly charged molecular ion must be further ionized by the IR pulse in the probe step. The vertical ionization potential of $\text{C}_3\text{H}_4^{3+}$ is 53.05 eV [MBo8] which is 25 eV above the vertical ionization potential of the allene dication. IR intensities comparable to those in the single pulse experiments were used in the pump-probe experiment to overcome this energy difference.

Unfortunately no triple-ion coincidences have been detected with certainty during this experiment due to two reasons. First, the probability for a single-photon double ionization of a molecule by the XUV pulse and a sequential multi-photon ionization of the same molecule by the IR pulse is too small to produce triply charged allene in a significant amount. Furthermore, the used acceleration voltage of 400 V was too low to guarantee a detection of highly energetic triple-ion coincidences over the full solid angle. As a result only a low number of candidates for triple-ion coincidences have been observed and it is impossible to distinguish them from false coincidences that fulfill the momentum sum conditions. This has been discussed in detail in section 5.2.1 for the measurement with single IR pulses.

Only double-ion coincidence channels have been identified unambiguously in this pump-probe experiment. For each channel, the number of coincidences is plotted as a function of delay time in figure 5.19. Delay dependent numbers of coincidence in figure 5.19 indicate a nuclear rearrangement or isomerization process that is interrupted by the probe pulse.

The channels $\text{C}_3\text{H}_3^+ + \text{H}^+$ (shown in figure 5.19(a)), $\text{C}_3\text{H}^+ + \text{H}_3^+$ (shown in figure 5.19(c)) and $\text{C}_2\text{H}_2^+ + \text{CH}_2^+$ (shown in figure 5.19(d)) feature such a delay dependence. For these channels the number of counts for delays between -50 fs and 0 fs is slightly increased. This can be explained by two mechanisms:

- The allene molecule is excited by the XUV pump pulse to a short-lived metastable or transient doubly charged state which decays within approximately 50 fs to a

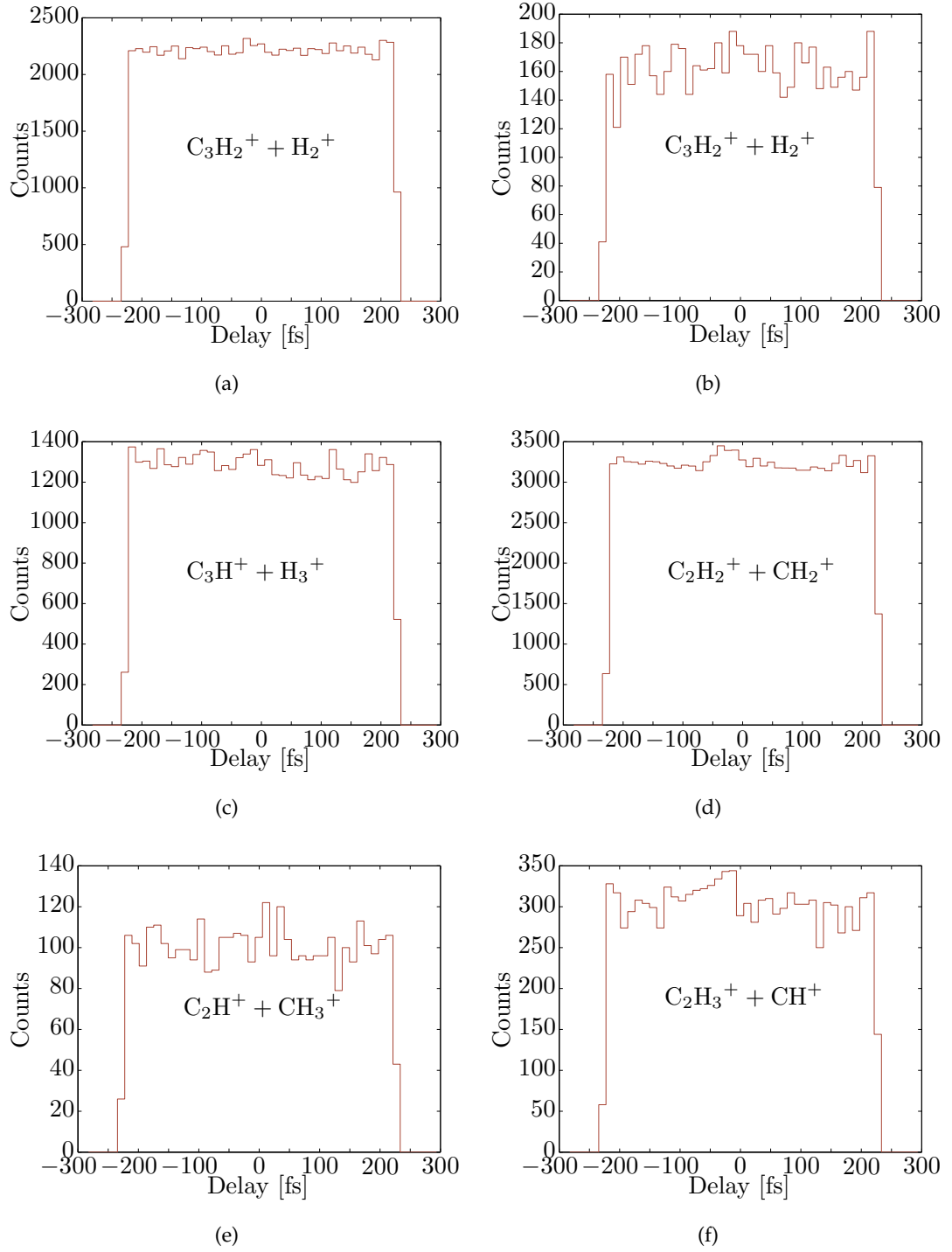


Figure 5.19.: Measured counts of the Coulomb-Explosion channels over the delay between laser pulses. Negative delay means XUV pulse comes first.

stable state. This will lead to an increased number of detected coincidences for delays between -50 fs and 0 fs, if the IR probe pulse is able to excite the short-lived state to a repulsing state which fragments in a Coulomb-explosion. Only if such a repulsing state is less probable to be reached from the stable state, the lower detection rate for delay times between -200 fs and -50 fs can be explained.

- The allene molecule is excited by the XUV pump pulse to a doubly charged dissociating state, that decays within approximately 50 fs into one doubly charged and one neutral fragment. The neutral fragment cannot be detected with the ReMi. Therefore such a dissociation will not be detected as a coincidence. If the IR pulse excites this dissociating state to a state which explodes into two singly charged particles, an increased number of coincidences will be detected for delays between -50 fs and 0 fs.

The $\text{C}_3\text{H}^+ + \text{H}_3^+$ spectrum in figure 5.19(c) shows a second increase in counts at around -100 fs. This could indicate an oscillation between different $\text{C}_3\text{H}_4^{2+}$ geometries of which some will fragment via this channel if probed by the IR pulse while others will not. An oscillation between the cyclopropene ($\text{c-C}_3\text{H}_4^{2+}$) and the 5^{++} geometry in figure 4.5 is predicted by A. M. MEDEL AND A.D. BANDRAUK [MB08]. The cyclopropene geometry features a fragmentation pathway to $\text{C}_3\text{H}^+ + \text{H}_3^+$, while the 5^{++} does not. This could explain the observed oscillation of the count rate. A Fourier transform of the measured spectrum, however, does not indicate an oscillation at a distinct frequency.

The photon flux in the XUV pulse is much lower than the photon flux in the intense IR pulse and on average less than one allene molecule is doubly ionized per the IR pulse. Therefore the probability to probe a doubly charged allene ion with the XUV pulse very small. This leads to the conclusion that any delay dependence for positive time delays is attributed to statistical fluctuations.

Summarizing, there are hints for a delay dependence of the count rate albeit the statistical significance is limited. It is definitely worth to repeat the pump-probe measurement with an extremely low IR intensity. While this will reduce the overall count rate, effects caused by the XUV pulses will get more pronounced and the number of false coincidences is reduced to a minimum. This will further increase the visibility of delay dependent effects.

6. Summary and outlook

Coulomb-explosions of allene (C_3H_4) dications induced by ultrashort laser pulses have been investigated within the framework of this thesis. All experiments performed in this work have been conducted with a laser system and a ReMi which had previously only been used with atomic or diatomic targets. The primary motivation for this project was gathering experience with the acquisition and evaluation of data obtained from fragmentations of larger molecules. The comparison of our results with those from previous Coulomb-explosion imaging experiments with single IR pulses provides a benchmark for the performance of our experimental setup. Also a pump-probe experiment was carried out to directly measure isomerization times of doubly charged allene for the first time reported.

A Monte-Carlo simulation of molecular fragmentations in ReMis has been developed and its applicability for data evaluation has been demonstrated. Especially the possibility to simulate fragmentations from metastable dications improved our understanding of ion trajectories from delayed Coulomb-explosions.

Proton ToF spectra were used to analyze metastable allene dications and it was found that the decay is best described by two exponential functions, one with a short half-life and another with a long half-life. The short half-life, measured as $T_{1/2} = 193\text{ ns}$ at medium laser intensity and $T_{1/2} = 144\text{ ns}$ at low laser intensity, is in good agreement with $T_{1/2} = 190\text{ ns}$ obtained from indirect measurements in previous experiments [XOY09b]. The half-life of the long-lived state was measured as $T_{1/2} = 889\text{ ns}$ at medium laser intensity and $T_{1/2} = 963\text{ ns}$ at low laser intensity. A comparable measurement on allene has not been reported before.

Single pulse experiments have been conducted with IR pulses of three different intensities and two different pulse lengths. The observed Coulomb-explosion channels are predicted by theory and have been reported by previous experiments [XOY09b]. The branching ratio of the stable allene dication does strongly depend on the laser intensity while pulse length dependencies were less pronounced. At low laser intensities production of stable doubly charged molecular ions is enhanced whereas at mid and high laser intensities fragmentation channels dominate. Direct Coulomb-explosion pathways are found to be favorable compared to indirect pathways which fragment via one or more transition state. If the branching ratios of fragmentation paths of the same type (indirect or direct) are compared, paths with lower barriers in the PES are favored. The branching ratios of the $\text{C}_2\text{-C}$ coincidences were found to be independent of the pulse parameters.

Measured KERs from IR experiments are independent of pulse parameters as well. They are in good agreement with those of Coulomb-explosions induced by single-photon double ionization with XUV laser pulses. It is concluded that the molecular PESs are not altered significantly by the field strengths of the IR pulses. The minimal measured KERs of the Coulomb-explosion channels are in good agreement with predictions from theory [MBo8,PTS10] for all but one fragmentation channel. The mean KERs of C_3 -H coincidences are consistent with results from previous experiments [XOY09b] but the KERs of C_2 -C coincidences differ significantly.

Triple-ion coincidences were not observed in a significant amount. Most of the events which pass the sum momentum conditions of expected triple-ion channels are most likely created by false coincidences. This is partly explained by the low acceleration voltage of 400 eV which is sufficient for detection of singly charged ions with kinetic energies up to 6.25 eV over the full solid angle. A detection of highly energetic protons created from a fragmentation of triply charged allene is still guaranteed for certain angular distributions. The absence of triple-ion coincidences is therefore only explained by a very small probability to create triply charged allene. Why triple-ion coincidences have been observed in previous experiments [XOY09a] at IR pulse intensities that were comparable to ours is not yet fully understood.

The total count rate of single-photon double-ionization by XUV pulses is small compared to the count rate for multi-photon double ionization by IR pulses (at pulse intensities used in this experiment). As a result, an XUV-IR pump-probe measurement on allene did not show unambiguous signs of molecular dynamics. In the overlap region of the pulses, the production of certain fragmentation channels seems slightly enhanced. Furthermore there are hints suggesting that the branching ratio of the $C_3H^+ + H_3^+$ channel oscillates with the delay time. Both effects, however, might result from statistical fluctuations as well.

Further investigation into allene Coulomb-explosion imaging experiments is definitely worth considering. A few lessons should be drawn from the experiments conducted in this work. First of all, the count rate needs to be reduced in all measurements. High count rates cause the detection efficiency of heavy $C_3H_i^+$, $i \in 1, 2, 3, 4$ fragments to depend on their initial momentum. Also, high count rates reduce the overall detection efficiency of these fragments. As a result, neither branching ratios nor angular distributions of Coulomb-explosions can be used for quantitative analysis, if these fragments are involved. In addition, a smaller count rate will reduce the number of false coincidences. Furthermore the TDC window should be opened for longer ToFs, otherwise heavy molecular ions with initial momentum away from the ion detector are not detected.

If the search for triple-ion coincidences at high IR intensities is to be continued, methods to reduce the count rate will be necessary as well. This can be realized by misaligning the target jet in such a way that a larger part of the jet is cut out by the skimmer of the ReMi's jet stage. Slightly misaligning the laser beam with respect to

the target jet will have the same effect: a reduction of the target density in the beam waist, which will result in a lower overall count rate. At the same time a very high laser intensity can be chosen to create triply charged allene ions. Protons created from triply charged parent ions are expected to gain approximately twice the kinetic energy of those measured in this experiment. To guarantee acceptance over the full solid angle, an acceleration voltage of 800 V will be required.

Future pump–probe experiments should focus on the detection of double-ion coincidences. This will allow to operate the IR pulses at extremely low intensities. To set the IR intensity XUV pulses should be blocked and the motorized aperture should be closed until the IR alone does not create singly charged allene anymore. The center of the delay range should be shifted towards negative values. This way the XUV pump pulses would mostly arrive before the IR probe pulses. The faint oscillation of the $\text{C}_3\text{H}^+ + \text{H}_3^+$ branching ratio (assuming it is not an artifact) seems to happen on time scales of approximately 70 fs. Increasing the delay range to 700 fs would ensure the detection of enough oscillations for an effective Fourier transform.

To our knowledge, electrons and ions created in allene fragmentations have never been detected in coincidence. The ReMi’s capability of electron detection has not been used in the present experiments either, because matching electrons to corresponding ions is virtually impossible, if more than one target molecule is ionized per laser pulse. In future low rate measurements, electron detection might provide additional interesting information. Kinematically complete studies of all charged fragments will bring out additional valuable information on the PES. For instance correlations between the Coulomb-explosion channels and the energy levels of the removed electrons could be measured.

Experience gathered in this work is going to be beneficial in further pump–probe Coulomb-explosion imaging experiments and results presented in this thesis may trigger further investigation into isomerization dynamics of medium sized molecules which are still not thoroughly understood by theory.

A. Atomic unit system and other non-SI units

Typical scales of most quantities like lengths, masses, energy etc. in atomic and molecular physics are extremely small while other for example velocities are typically large. For convenience the so called atomic unit system is frequently used. In this system, electron mass m_e , elementary charge e , the classical Bohr radius a_0 , the Planck's constant \hbar and $1/(4\pi\epsilon_0)$ with the electric constant ϵ_0 are set to unity. "a. u." is the symbol used for any quantity given in atomic units. Table A.1 gives a selection of atomic units and their conversion factor to SI units. In the work only molecular bond lengths, measured ion momenta and charges are given in a. u..

Quantity	Expression	Value in SI units
mass	m_e	$9.109 \times 10^{-31} \text{ kg}$
charge	e	$1.602 \times 10^{-19} \text{ C}$
length	a_0	$5.292 \times 10^{-11} \text{ m}$
angular momentum	$\hbar = h/(2\pi)$	$1.055 \times 10^{-34} \text{ kg m}^2/\text{s}$
energy	$\hbar^2/(m_e a_0^2)$	$4.360 \times 10^{-18} \text{ J}$
time	$m_e a_0^2/\hbar$	$2.419 \times 10^{-17} \text{ s}$
velocity	$\hbar/(m_e a_0) = c\alpha$	$2.188 \times 10^6 \text{ m/s}$
momentum	\hbar/a_0	$1.993 \times 10^{-24} \text{ kg m/s}$

Table A.1.: Atomic units. Table copied from [Sen09].

For magnetic fields of reaction microscopes, the unit gauss with the abbreviation G is used. The conversion to the SI unit tesla is given by:

$$1 \text{ G} = 1 \times 10^{-4} \text{ T}.$$

B. Estimation influences of the earth's magnetic field on electron trajectories

One could argue that the washed out bands in section 3.4 do not result from a tilted field but from another, hidden effect. To support the theory of the earth's influence, an estimation of the effective magnetic field is done:

The earth's magnetic field in central Europe $|\vec{B}_{\text{earth}}| = 0.48$ G, with $B_{\text{earth}}^{\parallel} = 0.20$ G parallel to the earth's surface and $B_{\text{earth}}^{\perp} = 0.44$ G perpendicular to the ground [MMM⁺10]. The spectrometer axis and the electric field of the ReMi are oriented towards 146° (south-east), therefore the magnetic field must be aligned towards 326° (north-west).

The earth's magnetic field component perpendicular to the electric field is given by

$$B_{\text{earth}}^{B\perp E} = \sqrt{(B_{\text{earth}}^{\perp})^2 + (B_{\text{earth}}^{\parallel} \cdot \sin(326^{\circ}))^2} = 0.45\text{G}, \quad (\text{B.1})$$

while the component parallel to the spectrometer can be described with

$$B_{\text{earth}}^{B\parallel E} = B_{\text{earth}}^{\parallel} \cdot \cos(326^{\circ}) = 0.17\text{G}. \quad (\text{B.2})$$

At 40A current, the magnetic field is assumed to be homogeneous and the coils' magnetic field perpendicular to the electric field $B_{\text{coil}}^{B\perp E}$ fulfills $B_{\text{coil}}^{B\perp E} = -B_{\text{earth}}^{B\perp E}$. From the nodes of the electron trajectories, the total magnetic field within the ReMi is measured as $B_{\text{ReMi}}^{B\parallel E} = B_{\text{coil}}^{B\parallel E} + B_{\text{earth}}^{B\parallel E} = 7.90\text{G}$ which leads to a coils' field $B_{\text{coil}}^{B\parallel E} = 7.73\text{G}$ parallel to the electric field. The angle between the inverse electric field $-\vec{E}$ and the magnetic field \vec{B}_{coil} is calculated to:

$$\alpha_{\text{coil}}^{EB} = \arctan\left(\frac{B_{\text{coil}}^{B\perp E}}{B_{\text{coil}}^{B\parallel E}}\right) = 3.33^{\circ}. \quad (\text{B.3})$$

At a current of 45A, $B_{\text{ReMi}}^{B\parallel E} = 8.73\text{G}$, determined from the measured electron trajectories again, and $\vec{B}_{\text{coil}}^{B\parallel E} = 8.56\text{G}$. Assuming the angle of the magnetic field created by the coils does not depend on the current,

$$\vec{B}_{\text{coil}}^{B\perp E} = \tan(3.33^{\circ}) \cdot \vec{B}_{\text{coil}}^{B\parallel E} = 0.50\text{G} \quad (\text{B.4})$$

and $\vec{B}_{\text{coil}}^{B\perp E} \neq -\vec{B}_{\text{earth}}^{B\perp E}$! The relative angle between the total magnetic field \vec{B}_{ReMi} and the spectrometer axis is calculated to

$$\alpha_{\text{ReMi}}^{EB} = \arctan\left(\frac{B_{\text{ReMi}}^{B\perp E}}{B_{\text{ReMi}}^{B\parallel E}}\right) = 0.32^{\circ}, \quad (\text{B.5})$$

where $B_{\text{ReMi}}^{B\perp E} = B_{\text{coil}}^{B\perp E} - B_{\text{earth}}^{B\perp E}$. Although the angle differs from the simulated $\alpha_{\text{sim}}^{EB} = 0.5^\circ$, this deviation is not surprising. When simulating the electron spectra, there is definitely a freedom of a tenth of a degree within which it is hard to say how the experimental spectra are resembled best.

C. Estimation of experimental KER uncertainty

The KER of a double ion coincidence with kinetic energies E_i of the involved particles is given by

$$KER = \sum_{i=1,2} E_i \quad (C.1)$$

and the error is calculated by error propagation

$$\Delta KER = \sqrt{\sum_{i=1,2} (\Delta E_i)^2} \quad (C.2)$$

from the uncertainty of the single particle's kinetic energy ΔE_i .

E_i can be expressed as

$$E_i = \frac{(p_i^x)^2 + (p_i^y)^2 + (p_i^z)^2}{2m_i} \quad (C.3)$$

and its error is given by

$$\Delta E_i = \sqrt{\left(\frac{p_i^x}{m_i} \Delta p_i^x\right)^2 + \left(\frac{p_i^y}{m_i} \Delta p_i^y\right)^2 + \left(\frac{p_i^z}{m_i} \Delta p_i^z\right)^2}. \quad (C.4)$$

The momentum uncertainty in z-direction (ToF-direction) is smaller than in x, y directions ($\Delta p_i^z < \Delta p_i^x \approx \Delta p_i^y$) resulting in:

$$\Delta E_i < \sqrt{((p_i^x)^2 + (p_i^y)^2 + (p_i^z)^2) \left(\frac{\Delta p_i^y}{m_i}\right)^2} = \sqrt{\frac{2E_i}{m_i} (\Delta p_i^y)^2} \quad (C.5)$$

with equation C.3 applied. The sum momentum of both particles in y -direction is given by

$$p_{\text{sum}}^y = p_1^y + p_2^y \Rightarrow \Delta p_{\text{sum}}^y = \sqrt{(\Delta p_1^y)^2 + (\Delta p_2^y)^2}. \quad (C.6)$$

The ratio between the particles' momentum uncertainty is

$$\frac{\Delta p_1^y}{\Delta p_2^y} \approx \frac{\sqrt{m_1}}{\sqrt{m_2}} \quad (C.7)$$

if the jet temperature is neglected [Gop10, p. 69]. Applied to equation C.6, one obtains

$$\Delta p_{\text{sum}}^y = \sqrt{\left(1 + \frac{m_2}{m_1}\right) (\Delta p_1^y)^2} = \sqrt{\left(1 + \frac{m_1}{m_2}\right) (\Delta p_2^y)^2}. \quad (\text{C.8})$$

By rearranging, the momentum uncertainty for each particle can be obtained:

$$\Delta p_1^y = \frac{\Delta p_{\text{sum}}^y}{\sqrt{1 + \frac{m_2}{m_1}}}; \quad \Delta p_2^y = \frac{\Delta p_{\text{sum}}^y}{\sqrt{1 + \frac{m_1}{m_2}}} \quad (\text{C.9})$$

For the FWHM of the p_{sum}^y distribution of the $\text{C}_3\text{H}_2^+ + \text{H}_2^+$ coincidence measured in this experiment as $\Delta p_{\text{sum}}^y = 10$ a. u., $\Delta p_{\text{H}_2^+}^y = 2.2$ a. u.¹.

Combining equations C.9 and C.5 results in

$$\Delta E_1 \approx \sqrt{\frac{2E_1}{m_1} \frac{(\Delta p_{\text{sum}}^y)^2}{1 + \frac{m_2}{m_1}}}; \quad \Delta E_2 \approx \sqrt{\frac{2E_2}{m_2} \frac{(\Delta p_{\text{sum}}^y)^2}{1 + \frac{m_1}{m_2}}} \quad (\text{C.10})$$

This means the error of the kinetic energy ΔE_i is dependent on the magnitude of the kinetic energy E_i . For all coincidences, the width of the E_i distribution is small compared to its mean \bar{E}_i . With these considerations, the estimation

$$\Delta E_1 \approx \sqrt{\frac{2\bar{E}_1}{m_1} \frac{(\Delta p_{\text{sum}}^y)^2}{1 + \frac{m_2}{m_1}}}; \quad \Delta E_2 \approx \sqrt{\frac{2\bar{E}_2}{m_2} \frac{(\Delta p_{\text{sum}}^y)^2}{1 + \frac{m_1}{m_2}}} \quad (\text{C.11})$$

can be made. Applying this to equation C.2 results in

$$\Delta \text{KER} \approx \sqrt{\frac{2\bar{E}_1}{m_1} \frac{(\Delta p_{\text{sum}}^y)^2}{1 + \frac{m_2}{m_1}} + \frac{2\bar{E}_2}{m_2} \frac{(\Delta p_{\text{sum}}^y)^2}{1 + \frac{m_1}{m_2}}} \quad (\text{C.12})$$

which is an estimation for the uncertainty of the measured KER used in chapter 5.2.3.

¹This is not too far of the estimated momentum uncertainty of $\Delta p_{\text{D}^+}^y = 1.2$ a. u. of deuterons from a D_2 target jet. The momentum spread due to the jet temperature scales with the square root of the target molecules' mass and which partly explains the higher momentum spread in this experiment.

D. KERs measured with XUV pulses

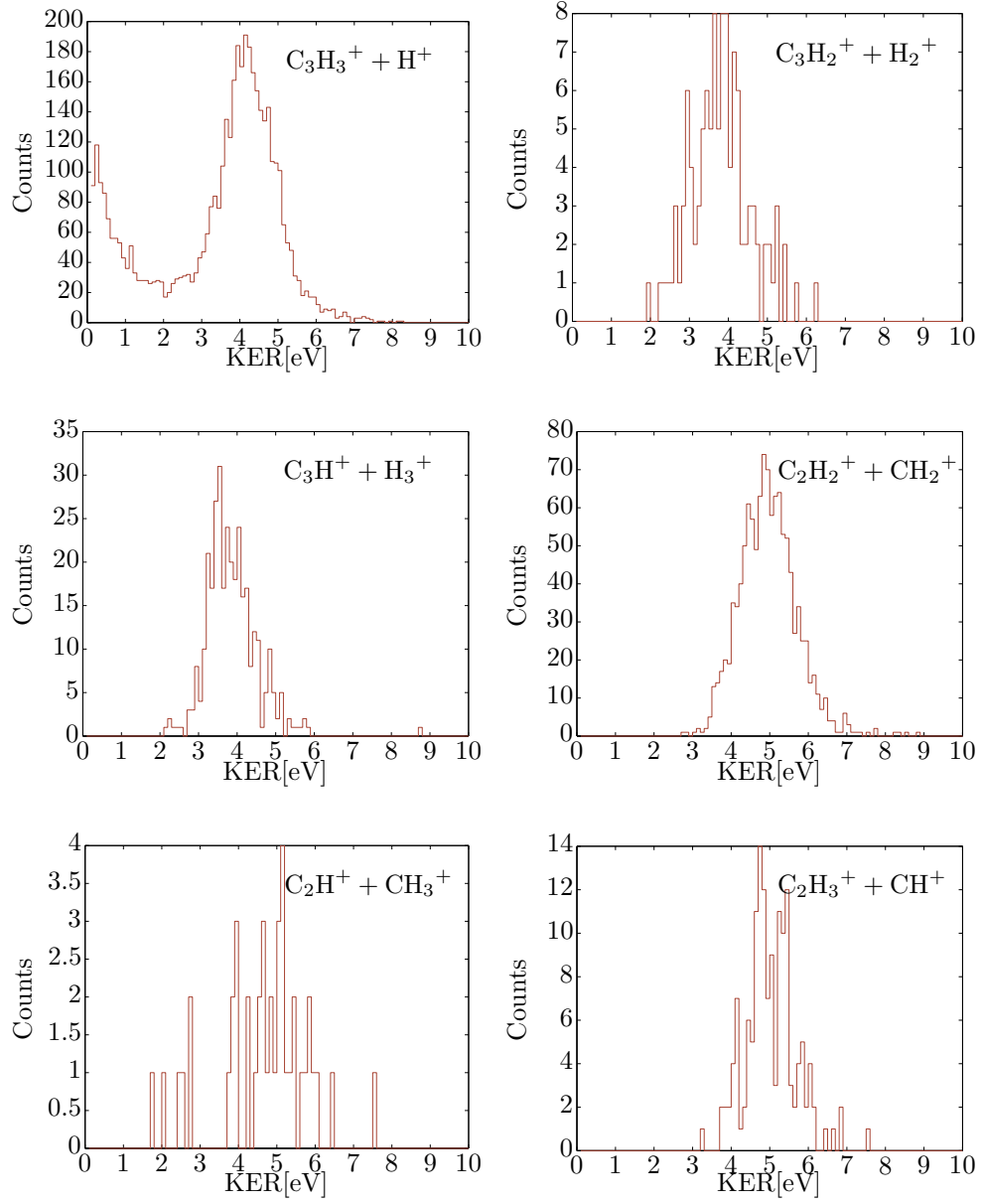


Figure D.1.: Measured KERs of XUV induced allene fragmentations.

E. Detection efficiency and drawbacks of high count rates

As mentioned at several parts of this work, the high count rates of up to 8 ions per laser pulse at medium and high IR intensities cause detection problems of heavy molecular ions. In this chapter, these problems are analyzed for C_3H_3^+ molecular ions, the following arguments apply to C_3H_2^+ and C_3H^+ as well.

A p_z momentum spectrum of C_3H_3^+ cations from the $\text{C}_3\text{H}_3^+ + \text{H}^+$ coincidence measured with different laser intensities is plotted in figure E.1. The counts of the p_z distributions at low and high pulse intensities have been multiplied by a factor of 20 and 1.35 respectively to obtain equal peak heights at -12 a. u. for better comparison.

In this plot, C_3H_3^+ ions with $p_z < 0$ explode towards the detector, while those with $p_z > 0$ have longer ToFs. The cutoff at $p_z = 20$ a. u. is created by the TDC window which does not accept ions with ToFs larger than 7300 ns (compare ToF spectrum 5.1 in chapter 5.2.1). From symmetry arguments, one would expect the p_z distribution to be symmetric around $p_z = 0$ because the laser polarization is parallel to the z -axis and the measurement was not performed with a stabilized carrier-envelope-phase. This is the case because the count rate drops fast at $p_z = -10$ a. u. and starts to rise just before the cutoff momentum. The spectrum can only be explained by a detection efficiency that is dependent on the ToF and on the count rate which is largest at high intensities where the effect is most prominent.

The majority of the C_3H_3^+ ions is not plotted in figure E.1 because it is created in non-coincident events (from single ionization with loss of a neutral hydrogen atom) with momenta mostly between -8 a. u. $< p_z < 8$ a. u.. The spectrum of these non-coincident ions features a similar asymmetry as the coincident ones. More than 40% of all detected ions are within the non-coincident C_3H_3^+ peak at low intensities, where the asymmetry is smallest. This means at high intensities, when up to eight ions are detected per laser short, multiple ions hit the MCP and delay line anodes within approximately 100 ns. Due to a finite dead time of readout of the delay line anode which is typically in the order of $t_e > 10$ ns [JMUP⁺02], a large fraction of the coincident C_3H_3^+ counts will be lost if they arrive at ToFs similar or slightly larger to those of non-coincident C_3H_3^+ molecular ions.

Missing $\text{C}_3\text{H}_3^+ + \text{H}^+$ coincidences can be reconstructed by the following method. At low pulse intensities, the counts with $p_z < 0$ are assumed to be not influenced by the dead time of the electronics (which is probably not completely true as seen in figure

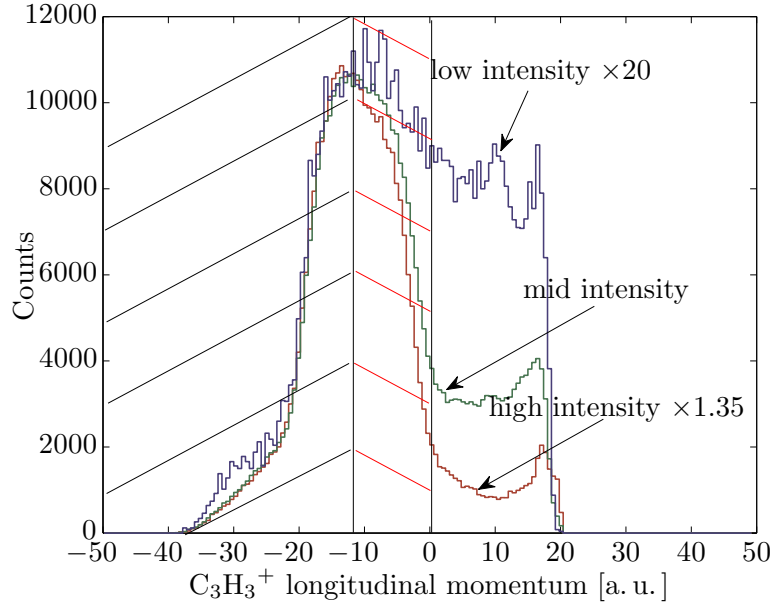


Figure E.1: Measured longitudinal momentum spectrum of coincident C_3H_3^+ at different laser intensities. The reconstruction of lost $\text{C}_3\text{H}_3^+ + \text{H}^+$ coincidences is done with this spectrum. Explanation see text.

E.1). For this intensity, the ratio

$$\frac{\gamma_{\text{C}_3\text{H}_3^+ + \text{H}^+}}{2} = \frac{N'_2}{N'_{\text{coinc}}} = 2.21 \quad (\text{E.1})$$

is calculated. Here, N'_{coinc} is the number of counts with $p_z < -12$ a. u. (area shaded black in figure E.1) and N'_2 is the number of counts with $p_z < 0$ a. u. (area shaded black and area shaded red in figure E.1) at low pulse intensity.

For $p_z < -12$, the detection efficiency seems to behave normal for medium and high pulse intensities as well and with the assumption that the angular distribution and magnitude of p_z does not depend on the laser parameters,

$$N'_2 = N'_{\text{coinc}} \frac{\gamma_{\text{C}_3\text{H}_3^+ + \text{H}^+}}{2} \quad (\text{E.2})$$

gives an estimation of the number of counts with $p_z < 0$ for all laser intensities and

$$N'_{\text{tot}} = N'_{\text{coinc}} \gamma_{\text{C}_3\text{H}_3^+ + \text{H}^+} \quad (\text{E.3})$$

gives the number of reconstructed counts for all p_z . The ratio $N'_{\text{tot}}/\epsilon^2$ with the estimated “normal” detection efficiency $\epsilon = 0.5$ of the MCP and delay line anode gives the number of originally produced $\text{C}_3\text{H}_3^+ + \text{H}^+$ coincidence (compare equation 5.4).

Table E.1 summarized γ_{coinc} values for all double ion coincidences. For $\text{C}_3\text{-H}$ coincidences, those values are obtained with the corresponding p_z spectra in a similar

way to that described above. The count rates at ToFs typical for CH_i^+ and C_2H_i^+ are very low, therefore a reconstruction is not required for C₂-C coincidences. In those cases $N'_{\text{C}_2\text{-C}}$ is simply the *total number* of detected coincident ions and $\gamma_{\text{C}_2\text{-C}}$ equals unity.

Coincidence	γ_{coinc}
$\text{C}_3\text{H}_3^+ + \text{H}^+$	2.21
$\text{C}_3\text{H}_2^+ + \text{H}_2^+$	1.77
$\text{C}_3\text{H}^+ + \text{H}_3^+$	1.49
$\text{C}_2\text{H}_3^+ + \text{CH}^+$	1.00
$\text{C}_2\text{H}_2^+ + \text{CH}_2^+$	1.00
$\text{C}_2\text{H}^+ + \text{CH}_3^+$	1.00

Table E.1.: γ_{coinc} -factors for coincidence reconstruction.

F. Bibliography

- [Air] Air Liquide. Safety data sheet, Propadiene. <http://encyclopedia.airliquide.com/encyclopedia.asp?CountryID=19&GasID=52&LanguageID=11>. Online; accessed 08.21.2012.
- [ALO⁺06] A. S. Alnaser, I. Litvinyuk, T. Osipov, B. Ulrich, A. Landers, E. Wells, C. M. Maharjan, P. Ranitovic, I. Bochareva, D. Ray, and C. L. Cocke. Momentum-imaging investigations of the dissociation of D_2^+ and the isomerization of acetylene to vinylidene by intense short laser pulses. *Journal of Physics B: Atomic, Molecular and Optical Physics*, 39(13):S485–, 2006.
- [AMATB⁺11] J. Adamczewski-Musch, M. Al-Turany, D. Bertini, H.G. Essel, and S. Linev. The Go4 analysis framework reference manual v4.5. Technical report, GSI Helmholtzzentrum für Schwerionenforschung, 2011.
- [Bal85] J. J. Balmer. Notiz über die Spectrallinien des Wasserstoffs. *Ann. Phys.*, 261(5):80–87, 1885.
- [Cor93] P. B. Corkum. Plasma perspective on strong field multiphoton ionization. *Phys. Rev. Lett.*, 71(13):1994–1997, September 1993.
- [Cor95] C. Cornaggia. Carbon geometry of $C_3H_3^+$ and $C_3H_4^+$ molecular ions probed by laser-induced coulomb explosion. *Phys. Rev. A*, 52(6):R4328–R4331, December 1995.
- [Demo8] Wolfgang Demtröder. *Molecular Physics: Theoretical Principles and Experimental Methods*. WILEY-VCH, 2008.
- [Dem10] Wolfgang Demtröder. *Experimentalphysik 3, Atome, Moleküle und Festkörper*. Springer Berlin Heidelberg, 2010.
- [DR06] Jean-Claude Diels and Wolfgang Rudolph. *Ultrashort Laser Pulse Phenomena: Fundamentals, Techniques, and Applications on a Femtosecond Time Scale*. Academic Press, 2006.
- [ERF⁺05] Th. Ergler, A. Rudenko, B. Feuerstein, K. Zrost, C. D. Schröter, R. Moshhammer, and J. Ullrich. Time-resolved imaging and manipulation of H_2 fragmentation in intense laser fields. *Phys. Rev. Lett.*, 95(9):093001–, August 2005.

- [FE93] Thomas A. Field and John H.D. Eland. Lifetimes of metastable molecular doubly charged ions. *Chemical Physics Letters*, 211(4–5):436–442, August 1993.
- [FHPW61] P. A. Franken, A. E. Hill, C. W. Peters, and G. Weinreich. Generation of optical harmonics. *Phys. Rev. Lett.*, 7(4):118–119, August 1961.
- [Fiso3] Daniel Fischer. *Mehr-Teilchen-Dynamik in der Einfach- und Doppelionisation von Helium durch geladene Projektile*. PhD thesis, Ruprecht-Karls-Universität, Heidelberg, 2003.
- [Fis10] Bettina Fischer. *Time resolved studies of H_2 dissociation with phase-stabilized laser pulses*. PhD thesis, Ruperto-Carola University of Heidelberg, Germany, 2010.
- [FKZ⁺04] M. Fischer, N. Kolachevsky, M. Zimmermann, R. Holzwarth, Th. Udem, T. W. Hänsch, M. Abgrall, J. Grünert, I. Maksimovic, S. Bize, H. Marion, F. Pereira Dos Santos, P. Lemonde, G. Santarelli, P. Laurent, A. Clairon, C. Salomon, M. Haas, U. D. Jentschura, and C. H. Keitel. New limits on the drift of fundamental constants from laboratory measurements. *Phys. Rev. Lett.*, 92(23):230802–, June 2004.
- [fXRO] Center for X-Ray Optics. Filter Transmission. http://henke.lbl.gov/optical_constants/filter2.html. Online; accessed 08.09.2012.
- [GDT⁺09] Mark Galassi, Jim Davies, James Theiler, Brian Gough, Reid Priedhorsky, Gerard Jungman, and Michael Booth. *GNU Scientific Library Reference Manual - Third Edition*. Network Theory Ltd., 2009.
- [Gop10] Ram Gopal. *Electron Wave Packet Interferences in Ionization with Few-Cycle Laser Pulses and the Dissociative Photoionization of D_2 with Ultrashort Extreme Ultraviolet Pulses*. PhD thesis, Ruperto-Carola University of Heidelberg, Germany, 2010.
- [Her87] H. Hertz. Ueber einen Einfluss des ultravioletten Lichtes auf die elektrische Entladung. *Ann. Phys.*, 267(8):983–1000, 1887.
- [HR23] H. Hartridge and F. J. W. Roughton. A method of measuring the velocity of very rapid chemical reactions. *Royal Society of London Proceedings Series A*, 104:376–394, October 1923.
- [JMUP⁺02] O. Jagutzki, V. Mergel, K. Ullmann-Pfleger, L. Spielberger, U. Spillmann, R. Dörner, and H. Schmidt-Böcking. A broad-application microchannel-plate detector system for advanced particle or photon detection tasks:

- large area imaging, precise multi-hit timing information and high detection rate. *Nuclear Instruments and Methods in Physics Research Section A: Accelerators, Spectrometers, Detectors and Associated Equipment*, 477(1–3):244–249, January 2002.
- [JRH⁺10] Y. H. Jiang, A. Rudenko, O. Herrwerth, L. Foucar, M. Kurka, K. U. Kühnel, M. Lezius, M. F. Kling, J. van Tilborg, A. Belkacem, K. Ueda, S. Düsterer, R. Treusch, C. D. Schröter, R. Moshhammer, and J. Ullrich. Ultrafast extreme ultraviolet induced isomerization of acetylene cations. *Phys. Rev. Lett.*, 105(26):263002–, December 2010.
- [Kir60] G. Kirchhoff. Ueber das Verhältniss zwischen dem Emissionsvermögen und dem Absorptionsvermögen der Körper für Wärme und Licht. *Ann. Phys.*, 185(2):275–301, 1860.
- [Kre09] Manuel Kremer. *Einfluß der Träger-Einhüllenden-Phase auf die Wechselwirkung ultrakurzer Laserpulse mit Molekülen*. PhD thesis, Ruprecht-Karls-Universität Heidelberg, 2009.
- [LBI⁺94] M. Lewenstein, Ph. Balcou, M. Yu. Ivanov, Anne L’Huillier, and P. B. Corkum. Theory of high-harmonic generation by low-frequency laser fields. *Phys. Rev. A*, 49(3):2117–2132, March 1994.
- [Lev08] Ira N. Levine. *Quantum Chemistry*. Prentice Hall, 2008.
- [LLF⁺89] X. F. Li, A. L’Huillier, M. Ferray, L. A. Lompré, and G. Mainfray. Multiple-harmonic generation in rare gases at high laser intensity. *Phys. Rev. A*, 39(11):5751–5761, June 1989.
- [LR47] Jr. Lamb, Willis E. and Robert C. Retherford. Fine structure of the hydrogen atom by a microwave method. *Phys. Rev.*, 72(3):241–243, August 1947.
- [MBo8] A. M. Mebel and A. D. Bandrauk. Theoretical study of unimolecular decomposition of allene cations. *J. Chem. Phys.*, 129(22):224311–12, December 2008.
- [MMM⁺10] S. Maus, S. Macmillan, S. McLean, B. Hamilton, A. Thomson, M. Nair, and C. Rollins. The us/uk world magnetic model for 2010-2015. Technical report, NOAA Technical Report NESDIS/NGDC, 2010.
- [MST95] G. P. Moss, P. A. S. Smith, and D. Tavernier. Glossary of class names of organic compounds and reactivity intermediates based on structure. *Pure Appl. Chem.*, 67(8-9):1307–1375, 1995.

- [MUS⁺96] R. Moshhammer, M. Unverzagt, W. Schmitt, J. Ullrich, and H. Schmidt-Böcking. A 4π recoil-ion electron momentum analyzer: a high-resolution “microscope” for the investigation of the dynamics of atomic, molecular and nuclear reactions. *Nuclear Instruments and Methods in Physics Research Section B: Beam Interactions with Materials and Atoms*, 108(4):425–445, March 1996.
- [MUU⁺94] R. Moshhammer, J. Ullrich, M. Unverzagt, W. Schmidt, P. Jardin, R. E. Olson, R. Mann, R. Dörner, V. Mergel, U. Buck, and H. Schmidt-Böcking. Low-energy electrons and their dynamical correlation with recoil ions for single ionization of helium by fast, heavy-ion impact. *Phys. Rev. Lett.*, 73(25):3371–3374, December 1994.
- [NHR⁺00] M. Niering, R. Holzwarth, J. Reichert, P. Pokasov, Th. Udem, M. Weitz, T. W. Hänsch, P. Lemonde, G. Santarelli, M. Abgrall, P. Laurent, C. Salomon, and A. Clairon. Measurement of the hydrogen 1s- 2s transition frequency by phase coherent comparison with a microwave cesium fountain clock. *Phys. Rev. Lett.*, 84(24):5496–5499, June 2000.
- [Nob] Nobelprize.org. “The Nobel Prize in Chemistry 1967”. <http://www.nobelprize.org/nobelprizes/chemistry/laureates/1967/index.html>. Online; accessed 08.07.2012.
- [PTS10] Brian T. Psciuk, Peng Tao, and H. Bernhard Schlegel. Ab initio classical trajectory study of the fragmentation of C_3H_4 dications on the singlet and triplet surfaces. *J. Phys. Chem. A*, 114(29):7653–7660, June 2010.
- [Rie07] Helga Rietz. Aufbau und Inbetriebnahme einer Apparatur zur Erzeugung hoher harmonischer Strahlung und deren Charakterisierung. Diploma thesis, Ruprecht-Karls-Universität Heidelberg, 2007.
- [SCC95] H. Stapelfeldt, E. Constant, and P. B. Corkum. Wave packet structure and dynamics measured by coulomb explosion. *Phys. Rev. Lett.*, 74(19):3780–3783, May 1995.
- [Scho7] Franz Schwabl. *Quantum Mechanics*. Springer Berlin / Heidelberg, 2007.
- [Sen09] Arne Senftleben. *Kinematically complete study on electron impact ionisation of aligned hydrogen molecules*. PhD thesis, Ruperto-Carola University of Heidelberg, Germany, 2009.
- [SLL⁺99] G. Santarelli, Ph. Laurent, P. Lemonde, A. Clairon, A. G. Mann, S. Chang, A. N. Luiten, and C. Salomon. Quantum projection noise in an atomic fountain: A high stability cesium frequency standard. *Phys. Rev. Lett.*, 82(23):4619–4622, June 1999.

- [Spe09] Alexander Sperl. Erzeugung und Charakterisierung ultrakurzer Lichtimpulse für die Generation Hoher Harmonischer Strahlung. Diploma thesis, Ruprecht-Karls-Universität, Heidelberg, 2009.
- [SSW⁺05] S. W. J. Scully, V. Senthil, J. A. Wyer, M. B. Shah, E. C. Montenegro, M. Kimura, and H. Tawara. Direct evidence of a strong isomer effect in electron-impact double ionization of C₃H₄. *Phys. Rev. A*, 72(3):030701–, September 2005.
- [UMD⁺03] J. Ullrich, R. Moshhammer, A. Dorn, R. Dörner, L. Ph. H. Schmidt, and H. Schmidt-Böcking. Recoil-ion and electron momentum spectroscopy: reaction-microscopes. *Reports on Progress in Physics*, 66(9):1463–, 2003.
- [WSWZ03] R. Wester, D. Schwalm, A. Wolf, and D. Zajfman. Coulomb-explosion imaging studies of molecular relaxation and rearrangement. In J. Ullrich and V.P. Shevelko, editors, *Many-particle quantum dynamics in atomic and molecular fragmentation*, pages 411–445. Springer-Verlag Berlin Heidelberg, 2003.
- [XOY09a] Huailiang Xu, Tomoya Okino, and Kaoru Yamanouchi. Tracing ultrafast hydrogen migration in allene in intense laser fields by triple-ion coincidence momentum imaging. *J. Chem. Phys.*, 131(15):151102–4, October 2009.
- [XOY09b] Huailiang Xu, Tomoya Okino, and Kaoru Yamanouchi. Ultrafast hydrogen migration in allene in intense laser fields: Evidence of two-body coulomb explosion. *Chemical Physics Letters*, 469(4–6):255–260, February 2009.
- [Zew88] Ahmed H. Zewail. Laser femtochemistry. *Science*, 242(4886):1645–1653, December 1988.
- [ZRX⁺12] Li Zhang, Stefan Roither, Xinhua Xie, Daniil Kartashov, Markus Schöffler, Huailiang Xu, Atsushi Iwasaki, Stefanie Gräfe, Tomoya Okino, Kaoru Yamanouchi, Andrius Baltuska, and Markus Kitzler. Path-selective investigation of intense laser-pulse-induced fragmentation dynamics in triply charged 1,3-butadiene. *Journal of Physics B: Atomic, Molecular and Optical Physics*, 45(8):085603–, 2012.

Danksagung

Für ihren Beitrag zum Gelingen dieser Arbeit möchte ich all denjenigen herzlich danken, die mich in den letzten Monaten unterstützt haben.

Dieser Dank gilt in erster Linie Priv.-Doz. Dr. Robert Moshhammer, der mich während des letzten Jahres betreut und meine Begeisterung für die Quantendynamik geweckt hat. Für die Zweitkorrektur dieser Arbeit danke ich Prof. Dr. Andreas Wolf.

Für das geduldige Beantworten von Fragen und die vielen hilfreichen Ratschläge und Anregung bei der Auswertung der Daten möchte ich Arne Senftleben danken. Seine Anregungen beim Programmieren und seine Erklärungen zu Konzepten der Molekülphysik waren unverzichtbar für meine Arbeit. Meinen Freunden und Laborkollegen Alexander Sperl, Andreas Fischer, Michael Schönwald und Helga Rietz danke ich für die Hilfsbereitschaft und die Unterstützung im Labor. Andreas Fischer, Alexander Sperl und Markus Berberich haben für das Korrektur lesen dieser Arbeit viele freie Tage geopfert und mir damit geholfen viele kleine und auch größere Fehler auszumerzen.

Besonders möchte ich meiner Familie für das Ermöglichen dieses Studiums und die Unterstützung in allen Lebenslagen danken.

UND VERENA IST DIE BESTE!

Erklärung:

Ich versichere, dass ich diese Arbeit selbstständig verfasst habe und keine anderen als die angegebenen Quellen und Hilfsmittel benutzt habe.

Heidelberg, den 05.09.2012

.....